UNIVERSITY OF CALIFORNIA

Santa Barbara

Bulk Group-III Nitride Crystal Growth in Supercritical Ammonia-Sodium Solutions

A dissertation submitted in partial satisfaction of the

requirements for the degree of

Doctor of Philosophy

in

Materials

by

Steven Herbert Griffiths

Committee in charge:

Professor Shuji Nakamura, Chair
Professor James S. Speck
Professor Steven P. DenBaars
Professor Michael F. Doherty

June 2017

The dissertation of Steven Herbert Griffiths is approved.

_____

Michael F. Doherty

_____

Steven P. DenBaars

_____

James S. Speck

_____

Shuji Nakamura, Chair

May 2017

Bulk Group-III Nitride Crystal Growth in Supercritical Ammonia-Sodium Solutions

By

Steven Herbert Griffiths

To

Sarah

Amor Vitae Meae

On the whole, it seems not improbable that the form of very minute crystals in equilibrium with solvents is principally determined … by the condition that $\sum(\sigma s)$ *shall be a minimum for the volume of the crystal except so far as the case is modified by gravity or the contact of other bodies, but as they grow larger (in a solvent no more supersaturated than is necessary to make them grow at all), the deposition of new matter on the different surfaces will be determined more by the nature (orientation) of the surfaces and less by their size and relations to the surrounding surfaces. As a final result, a large crystal, thus formed, will generally be bounded by those surfaces alone on which the deposit of new matter takes place least readily, with small, perhaps insensible truncations. If one kind of surfaces satisfying this condition cannot form a closed figure, the crystal will be bounded by two or three kinds of surfaces determined by the same condition. The kinds of surface thus determined will probably generally be those for which* σ *has the least values. But the relative development of the different kinds of sides, even if unmodified by gravity or the contact of other bodies, will not be such as to make* $\sum(\sigma s)$ *a minimum. The growth of the crystal will finally be confined to sides of a single kind.*

-J. Willard Gibbs, On the Equilibrium of Heterogeneous Substances (Concluded)
Transactions of the Connecticut Academy of Arts and Sciences, Vol. III (1878)

Acknowledgements

If one would have told me in high school, or early in the course of my undergraduate education, “Steven, you will go on to defend your Ph.D. at one of the best materials science programs in the world, with the most decorated scientists in the compound semiconductor community,” I would have replied, “get lost.” I cannot wrap my head around how fortunate I have been to undertake this research. There are many people to acknowledge, but the list must start with my esteemed faculty committee. Steve DenBaars and Mike Doherty have provided immense support and guidance on matters of device/autoclave design and the fundamentals of solution crystal growth, respectively. Jim Speck has devoted much of his time to my cause, with his notable expertise and advice on bulk crystal growth technology, and discussions of materials science fundamentals that went well beyond the quarter I spent as a teaching assistant for his MATRL 101 class. Of course my advisor, Shuji Nakamura, deserves a tremendous amount of credit for the work that I’ve been able to do at UCSB. His leadership, advice, and trust to let me pursue my own “crazy” projects have been invaluable to me as a developing scientist.

Working on bulk GaN at UCSB not only means working with the best faculty members and facilities, it also means having the best colleagues and peers. I owe an unrepayable debt to the other members of the bulk GaN team that I’ve shared time/office spaces with, including: Ben Bryant, Justin Palmer, Jared Kearns, Dano Pagenkopf, Mo Abo Alreesh, Andrew Espenlaub, Thomas Malkowski, Paul Von Dollen, and of course our fearless leader, Siddha Pimputkar. In particular, Andrew, Thomas, and Paul have contributed countless hours of discussion (both frivolous and fruitful) without which I would not have had the “aha” moments which make this dissertation worth reading. I don’t know where to begin describing Siddha’s

impact on myself and this work, but I suppose a fitting place is with the "best facilities" referenced in the first sentence of this paragraph. Siddha literally built the lab I used to conduct all of my experiments in. He directly oversaw my training, critically-engaged me on my scientific observations and analyses, and ensured (to the best of his ability) that my work lived up to the standards that should exist for our department and research group. I consider myself incredibly fortunate to grow into the role of materials scientist under his tutelage.

A huge reason that the bulk GaN group has enjoyed sustained research success and longevity is the adept support of the machinists who fix what we destroy. Although they sometimes rolled their eyes when they saw me coming into the shop with an autoclave with a sheared-off Inconel 718 7/16" bolt, they always agreed to help with it. The individuals who wear this "badge of patience" are Andy Weinberg, Andy Segale, Mark Sheckherd, Jeff Dutter, Doug Rehn, and Guy Patterson. Special thanks go out to Doug and Guy, who in addition to fixing my messes, worked with me to design new autoclave components and "custom tools."

The SSLEEC and Materials department staff (past and present) also deserve my humblest gratitude. In the lab, Brian Carralejo, Mike Iza, David Whitlach, Stacia Keller, Tal Margalith, and Erin Young provided immense support both of a technical nature, and in helping me find tools/equipment that were inevitably missing from where I last saw them. Furthermore, Deryck Stave was crucial in helping me develop alloying recipes in the Materials Processing Lab. The CNSI and MRL facilities and staff were a huge reason why I chose to come to UCSB in the first place, and the following people were pivotal to my research: Amanda Strom (for ICP-AES), Mark Cornish (for SEM and CL), Tom Mates (for SIMS), and Youli Li and Miguel Zepeda (for XRD). In the SLEEC office, Sheryl Condino-Montoya, Aldir Lopez, Fukiko Miyazaki, Michiko Sato, Tara Owens, and Yukina Warner were crucial in

helping me locate professors, file the right paperwork, obtain the proper equipment, and overall to devote my time to research rather than handling bureaucratic requirements. I frequently visited the Materials office with strange questions and requests, thus the department staff require a huge thanks as well, especially Oura Neak, Heather Gardner, Tawny Hernandez, Stefani Juarez, Budd Jamieson, and Jocelyn Guzman.

I've also had the pleasure to collaborate with many visiting researchers and international Universities. I would like to thank Hamad Albraithen and Mahdi Alqahtani from KACST in Saudi Arabia, Nurul Fatihah from USM in Malaysia, Srinivas Gandrothula and Naoya Goto from Sanoh in Japan, Sami Suihkonen and Pyry Kivisaari from Aalto University in Finland, and Sooyoung Moon from Seoul Semiconductor in South Korea. It was truly a pleasure to work alongside all of these researchers in the lab, and to share in fruitful discussions about research in different cultures. Furthermore, the BaCaTec program introduced me to many world-class German graduate students and researchers who were instrumental in providing feedback on my work, in addition to sharing their own. I would like to thank Thomas Steigerwald, Jan Hertrampf, Saskia Schimmel, and Anna Kimmel (who I worked with at UCSB during her Fulbright scholarship) in particular for their insight.

All of the aforementioned individuals were acknowledged for their contributions to my work, but an equal thanks is indebted to them for their kindness and friendship to me and my family. In addition to those previously mentioned, spouses and significant-others have made my life in Santa Barbara a joy. In particular, I would like to thank Hend Abo Alreesh, Miki Sankary, and Lauren Von Dollen. The Von Dollen clan, which includes Paul's better half (Lauren), Paul's parents (Steve and Karen), Paul and Lauren's children (Charlie and Will), Paul's siblings (Steve, Andrew, Mark, Susan, Margaret, and Karen Anna), and additional

extended family (aunts, uncles, cousins, goats, etc.), have been remarkably welcoming and open to sharing their home with us. Speaking of home, I had the honor of sharing a rental house with an amazing neighbor for four years. Gail Cooley deserves my humblest gratitude for her company, patience, support, and sharing of food and family, including her amazing children, James and Katherine. Also, our dear friends Chris and Allie Joyce have helped to make Santa Barbara home over the past four years. There are too many fellow graduate students (past and present) to thank for the parties, football games, dinners, picnics, Golf Classics, and other events that we have attended, but in the spirit of humiliating myself through omission, special thanks are owed to: Dan Becerra, Chris Pynn, Humberto Foronda, John Leonard, Burhan Saifaddin, Leah Kuritzky, Ben Yonkee, Stacy Kowsz, David Hwang, Asad Mughal, Sang Ho Oh, Doug Fabini, Tiberiu Stan, Tobias Brown-Heft, Brian Evanko, Brent Goodlet, Josh and Mandi Buffon, Rahul Sangodkar, Matt Idso, John Kaminsky, Stefan Heinze, Ryan Need, Megan Butala, Marissa Lafata, Philip Dodge, Chris Freeze, and Rob Rhein.

I am fortunate to have been given support from so many friends from my hometown in Ohio, and from friends in Michigan during my undergraduate years. From as early as I can remember, the Creme, Shippy, and Fechter families have been there to support me, encouraging me to pursue whatever I've found interesting. Through high school and beyond, Sean Rice, Cameron Scheetz, Marcus and Jessica Hardy, Phil Green, Morgan Gates, Rachael Hiengphothichack, Lauren Reed, Dane Cramer, Matt Dunaway, Josh and Joey Andrea, and so many others have constantly given me reassurance that I can accomplish whatever I put my mind to. While I was distilling my professional interests at Michigan, I was incredibly lucky to have the support of so many friends, including: Preston Smith, Justin Chronowski, Alex Schmidt, Carly Wheaton, Lauren Warner, Justin Baerwolf, Matt Bart, Charlie Rhodes, Ryan

Hosking, Katie Kelley, Meredith Horowski, Colleen Durnian, Erica Timinski, Anne Darrenberger, Patch Ronald, Kat Marsh, Ellen Dupler, Michelle Weaver, Kevin Wayne, and Garret Huff. I can't thank all of these people enough for sticking by me through thick and thin.

I do not think I would be where I am today without my family. I owe so much to my cousins, aunts, and uncles, who have been there with me for all of the highs and lows of my life. This list especially includes the Davis family (Aunt Gina and Uncle Keith, with Cousins Hilary and Elizabeth, and husband, Jesus), my Aunt Jackie (and fiancé, Larry) and Cousin Pete (and wife, Nina), the Jones-Raines family (Aunt Sandra and Aunt Tina, and Cousins Josh and Jake, with wives, Kristen and Taylor, respectively), the former-Griffiths' East (Aunt Donna and Uncle Barry, with Cousins Ben and Zach, and wife, Sarah), and the Esser family (late Aunt Carol and Uncle Bill, with Cousins Julie and Paul, and wife, Dania).

I am sure that I am a product of my parents and grandparents, for better or for worse (although I like to think it's for the better). My late Grandma and late Grandpa Sullivan were tough, loving people who worked at the GE Lamp Plant in Warren, OH on incandescent bulbs, so it is fitting that I continue in their lighting footsteps (albeit with different technology). My late Grandpa Griffiths inspired me with his passion for the outdoors and interest in anything scientific, and my Grandma Griffiths is a continuing example of the power of the arts and physical fitness. So much is owed to my Mom and Dad, Karen and Gordon, that I can't begin to thank them enough. When I've had questions, they've been there to answer them. When I've made mistakes, they've been there to help me learn from them. When I've felt lost, they've been there to show me the way. They gave me a brother and best friend, Neil, who even after not speaking to for long periods of time, I can pick up with as if a day hasn't gone by. I couldn't

have asked for a better nuclear family, because I know for whatever faults I possess, they will always be there for me.

Last, and certainly not least, I have to thank my loving wife, Sarah, who has made this dream of mine a reality. I met Sarah as a freshman in college, and must have impressed her with my ability to grunt yes-or-no responses to non-binary questions while eating Ramen noodles. In spite of this first impression, she saw potential in me and agreed to polish it. On the other hand, what I saw in Sarah from Day-1 was the warmest, kindest, and most honest person I had ever met. It was abundantly clear to me that in order to feel like I deserved her, that I had to become the best version of myself possible. This realization came without her, or my beloved in-laws (Dave and Nancy, and son, Tres, all of whom have been supportive beyond description), ever having to say anything. That is the level of trust and devotion that Sarah has shown me. Together we have found happiness, we have been there to support each other, and we have made a family (Lola, the dog, included) and a home in Santa Barbara during the duration of graduate school. I couldn't have done any of it without you, Sarah.

Curriculum Vitae

STEVEN HERBERT GRIFFITHS

EDUCATION

June 2017 *(expected)* — Ph.D., Materials
University of California, Santa Barbara

April 2012 — B.S.E., Materials Science and Engineering
University of Michigan

PUBLICATIONS

1. **S. Griffiths**, J. Kearns, T.F. Malkowski, S. Pimputkar, M.F. Doherty, J.S. Speck, and S. Nakamura
   Isothermal growth of bulk group-III nitride crystals from alloy sources in supercritical ammonia-sodium solutions (in preparation)

2. **S. Griffiths**, J. Kearns, T.F. Malkowski, S. Pimputkar, M.F. Doherty, J.S. Speck, and S. Nakamura
   Effect of internal fluid temperatures on gallium nitride growth in supercritical ammonia-sodium solutions (in preparation)

3. **S. Griffiths**, S. Pimputkar, J.S. Speck, and S. Nakamura
   On the solubility of gallium nitride in supercritical ammonia-sodium solutions
   Journal of Crystal Growth **456**, p. 5-14. (2016)

4. S. Pimputkar**,** T.F. Malkowski**, S. Griffiths** , J.S. Speck, and S. Nakamura
   Stability of materials in supercritical ammonia solutions
   Journal of Crystal Growth **110**, p. 193-229. (2016)

PATENTS

1. **S. Griffiths**, S. Pimputkar, P. Von Dollen, and J.S. Speck
   Group-III containing source material for bulk nitride solution growth
   UC Case No. 2017-137 (Patent Pending)

2. **S. Griffiths**, S. Pimputkar, P. Von Dollen, and J.S. Speck
   Solvothermal growth of single crystals using a single control temperature
   UC Case No. 2017-138 (Patent Pending)

INVITED PRESENTATIONS

1. Nitrides Seminar, Solid State Lighting & Energy Electronics Center
   On the solubility of gallium nitride in supercritical ammonia-sodium solutions
   Santa Barbara, CA, USA (2016)

2. 9th International Workshop on Bulk Nitride Semiconductors
   Solubility of gallium nitride in supercritical ammonia-sodium solutions
   Wonju, South Korea (2015)

TEACHING

1. Guest Lecturer, *MATRL 101- Introduction to Structure and Properties*
   Materials Dept., University of California, Santa Barbara (2016)

2. Lead Teaching Assistant, *MATRL 101- Introduction to Structure and Properties*
   Materials Dept., University of California, Santa Barbara (2015)

HONORS AND AWARDS

1. Outstanding Graduate Student Research Achievement Award
   Solid State Lighting & Energy Electronic Center,
   University of California, Santa Barbara (2016)

2. President, Alpha Sigma Mu Honors Society
   Materials Science and Engineering Dept., University of Michigan (2011)

3. Jack J. Heller Memorial Engineering Scholarship
   Materials Science and Engineering Dept., University of Michigan (2011)

Abstract

Bulk Group-III Nitride Crystal Growth in Supercritical Ammonia-Sodium Solutions

Steven Herbert Griffiths

Gallium nitride (GaN) and its alloys with indium nitride (InGaN) and aluminum nitride (AlGaN), collectively referred to as Group-III Nitride semiconductors, have enabled white solid-state lighting (SSL) sources and power electronic devices. While these technologies have already made a lasting, positive impact on society, improvements in design and efficiency are anticipated by shifting from heteroepitaxial growth on foreign substrates (such as sapphire, Si, SiC, etc.) to homoepitaxial growth on native, bulk GaN substrates.

Bulk GaN has not supplanted foreign substrate materials due to the extreme conditions required to achieve a stoichiometric GaN melt (temperatures and pressures in excess of 2200°C and 6 GPa, respectively). The only method used to produce bulk GaN on an industrial scale is hydride vapor phase epitaxy (HVPE), but the high cost of gaseous precursors and relatively poor crystal quality have limited the adoption of this technology. A solution growth technique known as the ammonothermal method has attracted interest from academia and industry alike for its ability to produce bulk GaN boules of exceedingly high crystal quality. The ammonothermal method employs supercritical ammonia (NH_3) solutions to dissolve, transport, and crystallize GaN. However, ammonothermal growth pressures are still relatively high (~200 MPa), which has thus far prevented the acquisition of fundamental crystal growth knowledge needed to *efficiently* (i.e. through data-driven approaches) advance the field. This dissertation

focused on addressing the gaps in the literature through two studies employing in situ fluid temperature analysis.

The first study focused on identifying the solubility of GaN in supercritical NH_3-Na solutions. The design and utilization of in situ and ex situ monitoring equipment enabled the first reports of the two-phase nature of supercritical NH_3-Na solutions, and of Ga-alloying of Ni-containing autoclave components. The effects of these error sources on the gravimetric determination of GaN solubility were explored in detail.

The second study was aimed at correlating autoclave dissolution and growth zone fluid temperatures with bulk GaN crystal growth kinetics, crystal quality, and impurity incorporation. The insights resulting from this analysis include the identification of the barrier between mass transport and surface integration-limited GaN growth regimes, GaN crystal shape evolution with fluid temperature, the sensitivity of (0001)-orientation crystal quality with fluid temperature, and impurity-specific incorporation activated from the dissolution and growth zones of the autoclave.

The results of the aforementioned studies motivated a paradigm-shift in ammonothermal growth. To address this need, a fundamentally different crystal growth approach involving isothermal solutions and tailor-made Group-III alloy source materials was developed/demonstrated. This growth method enabled impurity incorporation reduction compared to traditional ammonothermal GaN growth, and the realization of bulk, ternary Group-III Nitride crystals.

Contents

List of Figures

List of Tables

Chapter 1 Introduction

Single crystal semiconductor materials are to modern society what iron and steel were to the industrial revolution. They have provided a "materials vehicle" by which the electronic age was born. From computers and cell phones, to electrical grid infrastructure and transportation, it is difficult to imagine the 21st Century without the wonders of semiconductors. Although the single crystal semiconductor era began with germanium and silicon, which enabled the construction of the first transistor devices, the story told in this work starts with an even older concept: light.

1.1 Lighting: The Engine of Enlightenment for Mankind

The synonymous nature of the lightbulb with ideation goes back to Thomas Edison's prolific number of inventions (exceeding 1000 in the US alone), the most famous of which was the incandescent lightbulb in 1879. However, lighting has played an essential role in human evolution well before the time of Edison. The first control of fire dates back to the Homo erectus era (ca. 1,000,000 years ago) [1], where immense cultural innovation was realized by extending ancestral human activity into the night. Given the broad variety of light sources that have been utilized since mastering fire, a standard metric of the effectiveness of visible light production is required to compare these light sources. Luminous efficacy is a measure of how efficiently a source produces light at wavelengths that are perceptible to the human eye, which is quantified by the ratio of luminous flux to radiant flux, expressed in lm/W. For example, since the sensitivity of the human eye peaks at 555 nm light (green), light sources efficiently producing radiation in this spectral range have a higher luminous efficacy than light sources

efficiently producing radiation in the infrared region of the spectrum. The first "engineered" light source could be considered the oil lamp (ca. 15000 B.C.) which had ~0.1 lm/W luminous efficacy [2]. Kerosene lamps have not improved much beyond this, and are considerably dangerous to use from a flammability and air pollutant perspective. Fast-forward millennia later to the 19th century, and the development of the incandescent lightbulb yielded far cleaner and more efficient lighting at ~16 lm/W [2]. The fluorescent bulb yielded higher efficiency yet in the 20th century, achieving ~70 lm/W [2]. However, these technologies are still a far cry from an ideal white light source, such as black body radiation from the sun (5800 K), which when truncated to the visible spectrum produces light at ~250 lm/W. Fundamentally different technology is required to reach luminous efficacies in this range: that of solid-state lighting (SSL).

The beginning of the SSL revolution occurred in 1907, when electroluminescence was discovered by Henry Joseph Round with the passage of current through small silicon carbide (SiC) crystals [3]. Electroluminescence is the process by which photons are emitted by a material due to the recombination of electrons and holes. A light-emitting diode (LED) operates using this principle, with the color of the light emission determined by the bandgap of the semiconductor material in the device. The first visible LED (which emitted in the red region of the spectrum) was invented by Nick Holonyak Jr. in 1962 [4]. By 1972, orange, yellow and green LEDs had been demonstrated [5]. These LEDs were produced from alloys of gallium arsenide (GaAs) and gallium phosphide (GaP). However, the last primary color, blue, cannot be achieved with these materials. With the goal of combining the primary colors into a white SSL source, scientists raced to achieve blue emission using three different material systems: SiC, zinc selenide (ZnSe), and gallium nitride (GaN). Although SiC could be grown

with decent crystal quality in bulk and epitaxial form, it is an indirect bandgap semiconductor, implying radiative recombination is coupled with heat evolution, which makes it an inefficient light source [6]. ZnSe is a direct bandgap semiconductor, and could also be grown with very high crystal quality (it is lattice-matched to GaAs), but p-type doping was (and still is) very difficult to achieve, limiting the capability of scientists to create an efficient p-n diode structure [7]. Herbert Maruska was the first to demonstrate faint blue/violet emission using GaN grown on a sapphire substrate in a metal-insulator-semiconductor (MIS) LED architecture [8] , but once again, the inability to grow p-type GaN made bright blue emission impossible.

A flurry of GaN activity occurred in Japan in the late 1980's and early 1990's which made the bright blue LED possible. At Nagoya University, Isamu Akasaki and Hiroshi Amano pioneered the low temperature aluminum nitride (AlN) buffer layer on sapphire substrates in 1985 [9] and p-type activation of GaN by electron beam irradiation in 1989 [10], which enabled the first p-n homojunction GaN LED. At Nichia Corporation, Shuji Nakamura invented the two-flow metal organic chemical vapor deposition (MOCVD) reactor in 1991 [11], which enabled the growth of high quality GaN buffer and epitaxial material on sapphire substrates later that year [12]. By discovering hydrogen passivation as the cause of p-type conductivity suppression [13], Nakamura then developed p-type activation by thermal annealing in 1992 [14]. Using Zhores Alferov and Herbert Kroemer's double heterostructure (DH) concept [15], and the improved ability of the two-flow MOCVD reactor to grow high quality indium gallium nitride (InGaN) of tunable composition, Nakamura achieved the first room temperature band-to-band emission from InGaN active layers in 1992 [16], and the first candela-class InGaN/AlGaN DH LED in 1994 [17]. After a string of subsequent device demonstrations by Nakamura, including: green and yellow InGaN DH LEDs in 1995 [18], a pulsed violet InGaN

DH laser diode (LD) in 1996 [19], and then a continuous wave (CW) violet InGaN DH LD later that year [20]; Nichia released the first commercial white phosphor-converted (PC) LED utilizing a blue InGaN DH LED in 1996. The challenges and implications associated with SSL were so immense that Akasaki, Amano, and Nakamura were awarded the 2014 Nobel Prize in Physics "for the invention of efficient blue light-emitting diodes which has enabled bright and energy-saving white light sources" [2]. The era of SSL had begun thanks to the Group-III Nitride semiconductor revolution.

1.2 Bulk Group-III Nitride Semiconductors

As previously mentioned, GaN and its alloys with InN (InGaN) and AlN (AlGaN), collectively referred to as Group-III Nitride semiconductors in this work, have enabled white SSL sources. While white LED technology has made a lasting, positive impact on society, commercial LED performance is still hampered by fundamental barriers, which include efficiency droop of blue LEDs for PC-LED architectures, and inefficient green emitters (the "green gap") for color-mixed LED light sources [21]. These challenges have limited the current generation of commercial white LED packages to luminous efficacies on the order of 130 – 160 lm/W at 35 A/cm^2 [22]. One potential solution to reach commercial LED packages with 250 lm/W is to shift from heteroepitaxial growth on foreign substrates (such as sapphire, Si, SiC, etc.) to homoepitaxial growth on native, bulk GaN substrates. Nonpolar (and semipolar) substrate orientations cut from bulk GaN boules enable high quality growth of thick quantum wells. This results in devices with lower carrier density in the active region and zero (or reduced) spontaneous and piezoelectric polarization fields, and thus higher efficiency at high current density and longer wavelengths due to reduction of non-radiative Auger recombination [21][23][24][25].

Furthermore, LDs have a potential role to play in SSL because they do not suffer from current efficiency droop above threshold current, they emit collimated light (lower beam divergence over long distances), and they allow for increased light emission per wafer area than LEDs. Bulk GaN substrates are essential for LD production, as the deleterious effects of high dislocation density in heteroepitaxial films (resulting from lattice and coefficient of thermal expansion mismatch with respect to the foreign substrate) reduces laser lifetime to impractical values for commercial applications (~10^3 hours for epitaxial lateral overgrowth on sapphire substrates with 10^6-10^7 cm^{-2} dislocation density in the epitaxial layers) [26][27]. It is important to note that these are only the justifications for bulk GaN in optoelectronic applications. There are also immense performance improvements realized by transitioning from Si and SiC power electronic device layers to GaN, including increased breakdown voltage and decreased specific on-resistance. Furthermore, by utilizing a bulk GaN substrate (as opposed to a SiC substrate, for example) avalanche capability is realized, as are vertical device architectures (as opposed to lateral) [28].

The reason GaN devices are not largely-produced on GaN substrates is because it is not commercially-feasible to grow bulk GaN boules from the melt, as Si is grown by the Czochralski method, for instance. The temperature and pressure required to crystallize GaN from a stoichiometric melt (no decomposition of GaN into N_2 gas and liquid Ga) is ~2200°C and ~6 GPa, respectively [29]. Although GaN can be grown in bulk from solution (e.g. by high nitrogen pressure solution growth, HNPSG) and liquid metal fluxes (e.g. sodium flux), the only truly commercial bulk GaN growth method is from the vapor phase. This technique, known as hydride vapor phase epitaxy (HVPE, sometimes also referred to as halide vapor phase epitaxy), is analogous to MOCVD. Ammonia (NH_3) provides the N-species, and is supplied in excess

over a seed (which is typically either sapphire or GaAs) at appropriate flow rates to achieve a desirable boundary layer. The Ga-species (or other Group-III constituent) is supplied as GaCl gas, which is produced by bubbling HCl through liquid Ga. Bulk GaN boules have been produced by HVPE at growth rates exceeded 2.4 mm/day [30], up to 6" in diameter. However, HVPE suffers from some of the same ill-effects of heteroepitaxy, with typical threading dislocation density (TDD) from $10^5 - 10^7$ cm^{-2}, and high boule strain limiting the maximum achievable growth thickness before cracking to ~6 mm [27]. Furthermore, it has proven too costly to become truly cost-competitive with sapphire and Si due to the large amounts of NH_3 and HCl gas used in the process. Thus, the realization of a scalable, truly bulk GaN growth process would have a momentous impact on all GaN technologies, including LEDs and power-electronics, through defect reduction and enabling large area nonpolar and semipolar GaN substrates.

As previously mentioned, HNPSG and sodium flux have both been used to produce high quality GaN crystals. Both methods rely on the ability of liquid metal (pure Ga for HNPSG, and a Na:Ga atomic ratio of ~3:1 for sodium flux) to crack N_2 gas, thereby dissolving atomic N-species into the melt, wherein a GaN seed is placed and supersaturation is achieved (according to Sievert's Law), driving GaN growth. HNPSG requires process pressures which are only modestly lower than the equilibrium melt pressure (~1 – 2 GPa), which limits the size of the growth systems to impractical volumes [31]. Sodium flux, however, only employs ~1 – 10 MPa N_2 pressure, and has been demonstrated very recently to grow large-area GaN boules (up to ~7" diameter, in a hybrid technique with HVPE [32]) at growth rates exceeding 50 μm/hr [33]. However, no commercial products currently exist using either of these techniques.

This landscape brings us to the focus of this work. The need for bulk GaN, and generally bulk Group-III Nitride crystals, is real. The solutions put forth to grow bulk GaN are either too costly or ineffective to compete with foreign substrate materials to allow the true potential of Group-III Nitride semiconductor devices to be realized. Therefore, what follows is an introduction to the descendent of the hydrothermal growth technique, which has been used to grow oxide crystals for decades. This analogous technique for nitride crystals is known as the ammonothermal method.

1.3 The Ammonothermal Method

The ammonothermal method is a NH_3 solution growth technique which has received great interest from academia and industry alike for its ability to produce bulk GaN boules of exceedingly high quality. It is part of a family of solution growth techniques, described in general as solvothermal processes, meaning "any chemical reaction in the presence of a nonaqueous solvent or solvent in supercritical or near-supercritical conditions" [34]. Crystal growth through the solvothermal method can be further described using the transport growth model. Transport growth entails dissolution of the nutrient in a solvent (usually through the presence of mineralizer species), followed by transport of soluble intermediate species to seed crystals, and crystallization on said seed crystals through transformation of the intermediate species.

As previously indicated, the inspiration for ammonothermal growth comes from another successful solvothermal technique: hydrothermal growth. Hydrothermal growth was first demonstrated by Schafthaul in 1845 with the transformation of silicic acid into quartz crystals [35]. Further development of the technique was carried out by many scientists in France and Germany, one of them being Henri Saint-Claire Deville, who is reportedly the first

person to use a mineralizer (NaOH) to alter growth chemistry in his pursuit to transform bauxite to corundum [36]. In parallel with the development of hydrothermal growth, Weyl and Seely independently demonstrated the solubility of alkali metals in liquid NH_3 in 1864 and 1871, respectively [37]. Their studies of metal-NH_3 solutions enabled the hydrothermal-ammonothermal growth analogy. After relatively slow progress in the early 20^{th} century, hydrothermal growth of quartz exploded during World War II, with a shortage of natural quartz crystals from Brazil fueling demand for synthetic production to power the electronics industry. Captured reports heralded the growth of the first large-sized quartz monocrystal (> 1" diameter) by German scientist, Nacken, in 1946 [34], while A. Walker and E. Buehler founded the hydrothermal quartz manufacturing facility at Bell Labs in 1950 [38]. With the commercialization of oxide crystals in full-swing, R. Juza and H. Jacobs were the first to demonstrate nitride growth using the ammonothermal method by producing Be_3N_2 crystals and alkaline earth amides in 1966 [39]. Jacobs went on to work with R. Dwilinski, who demonstrated GaN synthesis by the "Ammono" method in 1995 [40].

Laudise states that transport growth can be achieved if the solubility of the desired solute approaches 3% in the hydrothermal system [41]. To understand the significance of this principle for GaN in the ammonothermal system, a comparison of the physical properties of NH_3 and water, as shown in Table 1-1, is required. Both molecules are polar, but water has a higher dielectric constant and dipole moment than NH_3, making it a better solvent for ionic species. NH_3 has a higher heat of neutralization (enthalpy required to form a neutral molecule from its conjugate acid and base), which is inversely proportional to the dissociation constant, thus it is easier for water to solvate ionic species [42]. GaN, however, has roughly 51% ionic bonding character, making it a good candidate for dissolution in a polar solvent [42]. Also, the

addition of mineralizers to the NH_3 solution enables greater solubility of GaN through the formation of soluble Ga-containing intermediate species. In addition to the mineralizer effect on solubility, achieving the supercritical state of NH_3 enhances its transport properties over that of a normal liquid (by increasing convection and diffusion to gas-like levels), and enhances the dissolution properties over that of a normal gas (by increasing the dielectric constant to values approaching that of a liquid).

Table 1-1. Physical properties of ammonia and water [43][42]**.**

Physical Properties of Ammonia and Water		
Property	Ammonia	Water
Boiling Point (°C)	-33.4	100
Freezing Point (°C)	-77.7	0
Critical Temp. (°C)	132.5	374.2
Critical Press. (bar)	113	221
Density (g/cm^3)	0.68 (-33°C)	0.96 (100°C)
Ionic Product	10^{-29}	10^{-14}
Heat of Vaporization (kJ/mol)	23.35	40.67
Heat of Fusion (kJ/mol)	5.65	8.37
Heat of Neutralization (kJ/mol)	-109.20	-56.11
Viscosity (cP)	0.135 (25°C)	0.891 (25°C)
Dielectric Constant	22 (-33°C)	80 (0°C)
Dipole Moment (D)	1.46	1.84
Polarizability (10^{24} cm^3)	2.25	1.49
Conductivity ($\Omega^{-1}cm^{-1}$)	4×10^{-10} (-15°C)	4×10^{-8}

The concepts of mineralizers, solubility, and chemical potential driving force will be discussed in depth in Chapter 2 . However, to draw distinctions between acidic and basic

ammonothermal growth, it will suffice to say that a basic mineralizer is a compound that forms amide ions (NH_2^-) in the NH_3 solution, whereas an acidic mineralizer forms ammonium ions (NH_4^+) in the NH_3 solution. The behavior of basic and acidic ammonothermal systems are very different with respect to corrosion, solubility, mass transport, and crystal growth kinetics. In general, acidic ammonothermal chemistry results in the corrosion of Ni-base superalloy autoclaves, which is the standard material used in ammonothermal growth due to its creep rupture resistance at the typical process pressures (~100 – 400 MPa) and temperatures (~400 – 700°C) of interest. This has resulted in the use of costly noble metal liner materials in acidic ammonothermal growth to prevent autoclave degradation and growth environment poisoning. To address this problem, various materials stability studies have been performed in different ammonothermal chemistries to identify universally-stable autoclave/liner materials, with some amount of success [44][45][46][47]. However, the first demonstrations of ammonothermal GaN growth were conducted using basic mineralizers to circumvent this problem, as were most of the experiments that were part of this work. As such, the history of basic ammonothermal growth is reviewed in detail in the following sections, delineated by the major institutions that performed the research.

1.3.1 The Ammono Company

The synthesis of GaN powder was first demonstrated using basic mineralizers ($LiNH_2$ and KNH_2) by R. Dwilinski et al. in 1995 at Warsaw University [40]. They determined that with ratios of $LiNH_2$:NH_3 of 1:10, at temperatures less than 550°C and pressures lower than 5 kbar, transformation of Ga to GaN went to completion and resulted in a well-shaped grain structure, as opposed to incomplete, inhomogeneous formation of GaN with a mineralizer ratio of 1:240. Also, the higher activity of KNH_2 with respect to $LiNH_2$ was realized as GaN

formation occurred faster, but resulted in less uniform, needle-like poly GaN morphology [48]. Dwilinski et al. also performed crystallization studies in which they doped the Ga nutrient with rare earth metals, such as erbium (Er), as they hypothesized that this would reduce oxygen incorporation in the GaN product through complexation of forward-solubilized Er-oxynitrides [49]. With an Er:Ga nutrient ratio of 1:10, shallow donor concentration was reduced to 5 x 10^{15} cm^{-3} in the GaN, as determined by electron spin resonance (ESR). Photoluminescence (PL) spectra also demonstrated the perceived reduction of oxygen, as yellow band emission diminished and exciton recombination increased [49]. Zajac et al. attempted to grow GaN doped with manganese (Mn) to form magnetic material suitable for spintronic applications, but they realized the formation of Mn_3N_2 precipitates throughout the GaMnN material [50].

While the work on transition metal doping of GaN through the basic ammonothermal method was being carried out at Warsaw University, Dwilinski and his team formed the Ammono Company in collaboration with Nichia Corporation. Their first patent for monocrystalline growth of GaN was published in 2003, revealing dislocation densities of 10^4 cm^{-2} for GaN films greater than 200 μm thick (for a 2 cm^2 area), with full width at half maximum (FWHM) <60 arcsec from the omega rocking curve of the 002 reflection [51]. They disclosed that metallic Ga is co-loaded with HVPE GaN feedstock so that dissolution and supersaturation of the basic ammonothermal environment occurs in two steps (although they moved away from a two-step nutrient dissolution approach later in the literature). An Ammono patent in 2004 demonstrated the use of azides as basic mineralizers [52]. By 2008, Ammono had grown a crystal of nearly perfect structural quality, with a dislocation density of ~ 10^2 cm^{-2}, and FWHM of the 002 reflection reaching 17 arcsec (which decreased to 10 arcsec when interrogated by a synchrotron microbeam, due to low beam diameter and high

monochromaticity and collimation) [53]. The low FWHM is evidence that there is no mosaicity or low angle grain boundaries present in the crystal. Arguably their most important improvement came by increasing the radius of curvature of their GaN crystal to 10^2 - 10^3 m (a normal value for HVPE GaN is closer to 2 - 12 m), which results in nearly strain-free epitaxial growth [53].

After their demonstration of a nearly-perfect crystal, Ammono published on other landmark advancements, including: demonstration of a 2" c-plane substrate in 2008 [54], m-plane substrates reaching 17 x 8 mm^2 of near perfection in 2009 [55], and the effects of Ammono substrate surface preparation on epitaxial growth in 2010 [56]. Of course their methods are proprietary, so details on the production of the substrates were not included in these publications.

1.3.2 University of California, Santa Barbara (UCSB)

The first publication for bulk GaN growth at UCSB involved parallel solubility and seeded growth studies in 2004. Hashimoto et al. used HVPE GaN platelets and a 1 molar (M) solution of $NaNH_2$ mineralizer, with the addition of 0.05 M NaI comineralizer, to confirm retrograde solubility of GaN in the basic ammonothermal regime [57]. A 3-day seeded growth employing Ga nutrient and HVPE seeds (under the conditions above) yielded growth asymmetry, with faster (0001)-orientation (Ga-face) growth than $(000\bar{1})$-orientation (N-face) growth. It was also noted that there were many pits and facets covering the Ga-face, indicative of island growth behavior [57]. In 2005, UCSB demonstrated the first seeded growth on a seed exceeding 1". The crystalline quality was not spectacular (with FWHM of the 002 reflections for the Ga-face and N-face achieving 2000 and 1700 arcsec, respectively) but dominant band edge luminescence was reported for the N-face under room temperature PL [58]. In 2006,

Hashimoto et al. performed a powder growth study to investigate the thermodynamic and kinetic stability of the metastable zinc-blende (cubic) GaN phase. According to their calculations, the difference in free energy of formation between the wurtzite phase and zinc-blende phase is 8 meV at 600 K, and its magnitude decreases with decreasing temperature [59]. This energy difference is small enough to allow for kinetic formation of zinc-blende GaN if high formation rates are realized. This was experimentally observed at 525°C with neutral and acidic mineralizers, but an order of magnitude less with basic mineralizers, reportedly due to the difference in reaction pathway in the basic ammonothermal regime.

Tremendous progress was made in GaN crystal quality in 2008 by increasing the mineralizer content and using poly GaN nutrient instead of metallic Ga. The FWHM of the 002 reflections for the Ga-face and N-face were reduced to 290 and 840 arcsec, respectively, while the TDD dropped from ~10^9 cm^{-2} to ~10^6 cm^{-2} on the Ga-face and ~10^7 cm^{-2} on the N-face [60]. It is expected that the previous use of Ga as a nutrient resulted in a premature supersaturation of the solvent, which initiated growth at the seed interface at a lower temperature, resulting in inferior crystal quality [60]. Multiple grain domains were confirmed by XRD and etching along the grain boundaries, with the higher crystalline quality of the wing region suggesting that lattice bending of the seed was to blame for the grain structure.

Significant research efforts have been made to understand the plane-dependent growth of GaN in the basic ammonothermal environment at UCSB. To this end, thickness and XRD measurements were performed on seeded GaN samples grown in different orientations under uniform ammonothermal conditions ($NaNH_2$ mineralizer, 500 - 600°C, 150 - 250 MPa) [61]. It was determined that the fastest growth rate (87 μm/day) and best quality (on-axis FWHM of 65 arcsec) was obtained for the semipolar plane, $(11\bar{2}2)$, while both c-plane polarizations

achieved high growth rates but poor quality due to their tilted columnar grain structure along the c-axis [61]. This columnar grain structure leads to pipe diffusion of impurities (e.g. Na) from the substrate to epilayers, which in turn may affect device performance [62]. $(10\bar{1}0)$ (m-plane) had the slowest growth rate (11 μm/day) [61]. In general, growth rate and crystal quality were found to increase with small off-orientation angle of the seed from the m-plane. More recently published results show different surface morphologies of nonpolar planes as a function of off-orientation angle from m-plane (to a-plane). A mound morphology is observed for m-plane, whereas for slight off-orientation angles, a slate-like morphology occurs, and for off-orientation angles from 20 - 30°, a pyramidal morphology is observed [63].

1.3.3 Air Force Research Laboratory (AFRL) and Clemson University

Ketchum and Kolis began work on the ammonothermal growth of Group-III Nitrides soon after Dwilinski et al. started their investigations. The focus in the beginning of their work was on fluoride-ammonia adduct formation with In and Al in the acidic ammonothermal regime [64]. In 2001, they attempted growth using GaN as a nutrient with KNH_2 as a mineralizer, due to its increased solubility in NH_3 as compared to $NaNH_2$ [65]. They were the first group to use a halide comineralizer in basic ammonothermal growth, adding KI to the KNH_2 charge in small quantities, which they hypothesized would attack the GaN nutrient first, forming a halide complex, which would later be displaced by amide to form Ga-amide-imides or GaN-amines as soluble intermediates [65]. In 2004, Clemson University teamed up with AFRL to begin growth experiments on both poly GaN and HVPE single crystal GaN seeds. Once again, growth asymmetry was encountered, resulting in greater Ga-face thickness than N-face. The FWHM of the omega rocking curve for the 002 reflection was 535 and 859 arcsec for the Ga-face and N-face, respectively [66]. As part of the Multidisciplinary University

Research Initiative (MURI), Kolis attempted to link structural and optical characterization techniques for the study of basic ammonothermal GaN films. He confirmed the correlation between low temperature PL peaks in the 3.30 - 3.45 eV region to the presence of basal plane stacking faults (BPSF), as identified by TEM [67]. Additionally, stacking mismatch boundaries, inversion domains, and screw dislocations were ruled out as being optically-active defects in this PL range [67].

In another collaboration between Clemson and AFRL, Wang et al. predicted the soluble intermediates in the basic ammonothermal regime. For mineralizers such as KNH_2, the tertra-amidogallates, $KGa(NH_2)_4$, are thought to form; whereas for $NaNH_2$ mineralizer, the penta-amidogallates, $Na_2Ga(NH_2)_5$, are thought to form [68]. This is expected to be the case due to the sterics of the solvated ternary amide, as the increased size of K disallows greater amide complexation, which has been experimentally verified recently by researchers from FAU for particular pressure-temperature regimes [69]. Callahan et al. (AFRL) later demonstrated very high GaN solubility in 2 - 4 M alkali amide solutions (14% at 350°C), with growth rates up to 40 μm/day [70]. He hypothesized that columnar growth on the Ga-face occurs due to a lower edge free energy, which favors kink and step face growth. Also, the presence of Ga_2O_3 at the seed interface may impede the morphological stability of the ammonothermal GaN material [70]. To reduce the issues of impurity incorporation and columnar morphology due to the presence of oxygen complexes in GaN, AFRL demonstrated growth of GaN in the presence of Er [71] under the same principals as Dwilinski et al. [49]. The Er-oxynitride was found to contain many metallic impurities, but incorporation of Er in the GaN crystal resulted in color centers [71]. AFRL also performed an in-depth morphological study of GaN growth in the presence of $NaNH_2$ and KNH_2 mineralizers (2 - 6 M) [72]. Their study yielded similar results

to Hashimoto et al. [73], with GaN displaying dominant Ga-face, N-face, m-plane, and pyramidal-plane $\{10\overline{1}1\}$ faceting, although the larger pyramidal planes were oriented towards the N-face, as opposed to the Ga-face [72].

1.4 Research Challenges Addressed in This Work

As previously indicated, bulk GaN crystals of extremely high quality have been realized by a number of researchers in the ammonothermal field. However, the relatively high system pressures have thus far prevented the acquisition of fundamental crystal growth knowledge needed to *efficiently* (i.e. through data-driven approaches) advance the state of the art. What follows in this work are two studies employing in situ fluid temperature analysis to determine the solubility of GaN in supercritical NH_3-Na solutions (in Chapter 2) and the effect of dissolution and growth zone fluid temperature on bulk GaN crystal growth (in Chapter 3). The insights resulting from these analyses led to the development/demonstration of a fundamentally-different approach to crystal growth (in Chapter 4), which not only addresses impurity incorporation reduction and poly GaN source material dependence in ammonothermal GaN growth, but also enables the growth of bulk, ternary Group-III Nitride crystals.

Chapter 2 On the Solubility of Gallium Nitride in Supercritical Ammonia-Sodium Solutions

2.1 Motivation

As stated in Chapter 1 , the ammonothermal method has received great interest from academia and industry alike for its ability to produce bulk GaN boules of exceedingly high quality. Conventional ammonothermal growth of GaN proceeds by establishing a temperature gradient between two zones ("dissolution" zone and "growth" zone) of an isobaric autoclave. The autoclave is filled with a NH_3 solution, enriched with additional chemical species called mineralizers to increase the solubility of GaN in the system, and is heated above its critical point (T > 132 °C, P > 11.3 MPa). Polycrystalline GaN source material is dissolved in the dissolution zone at a fluid temperature of T_D^{int}, and is transported to the growth zone, where the dissolved GaN crystallizes on single crystal GaN seeds at a fluid temperature of T_G^{int}. Traditionally, due to the moderately high pressure (≥ 200 MPa) and temperature (>500 °C) inherent to the technique, T_D^{int} and T_G^{int} are not typically measured or controlled directly, rather an external wall temperature gradient of the autoclave (T_G^{ext}- T_D^{ext}) is established and controlled. The ammonothermal method is pursued with either acidic or basic chemistries. In acidic ammonothermal growth, halide species (such as ammonium fluoride (NH_4F), ammonium chloride (NH_4Cl), etc.) are added as mineralizers, thereby shifting the dissociation reaction of NH_3 towards ammonium (NH_4^+); whereas, in basic ammonothermal growth, alkali or alkaline earth species (such as sodium (Na), potassium amide (KNH_2), etc.) are added as mineralizers, thereby shifting the dissociation reaction of NH_3 towards amide (NH_2^-). Both techniques have demonstrated growth of 2 inch diameter boules, with threading dislocation

density as low as $10^3 – 10^4$ cm^{-2}, but the state-of-the-art polar <0001> and nonpolar <10$\bar{1}$0> growth rates (the highest of which are near 1 mm/day) are thought to be too slow to supplant hydride vapor phase epitaxy (HVPE, with growth rates > 2.4 mm/day) as the industry-preferred growth method [74][75][76][77][78][79][80].

One potential method to increase growth rates in the ammonothermal system is to increase the chemical potential driving force for dissolved GaN to crystallize on seeds in the growth zone. The chemical potential driving force ($\Delta\mu$) is given by Equation 2-1, in which γ refers to the activity coefficient of GaN in the supercritical NH_3 solution at the specified temperatures ($\gamma_{GaN}^{NH_3(T_D^{int})}, \gamma_{GaN}^{NH_3(T_G^{int})}$), and *S* refers to the solubility of GaN in the supercritical NH_3 solution at the specified temperatures ($S_{GaN}^{NH_3(T_D^{int})}, S_{GaN}^{NH_3(T_G^{int})}$). Therefore, understanding solubility in the ammonothermal system is paramount in understanding the chemical potential driving force for bulk GaN crystal growth.

Equation 2-1

$$\Delta\mu = RT_G^{int}\ln\left(\frac{\gamma_{GaN}^{NH_3(T_D^{int})} * S_{GaN}^{NH_3(T_D^{int})}}{\gamma_{GaN}^{NH_3(T_G^{int})} * S_{GaN}^{NH_3(T_G^{int})}}\right)$$

Many research groups have studied the solubility of GaN in both the acidic ammonothermal environment (with NH_4F [81], NH_4Cl [81][82][83], NH_4Br and NH_4I [84] as mineralizers), and in the basic ammonothermal environment (with KNH_2 [53][68] and $NaNH_2$ [85] as mineralizers). For reference, all reported solubility curves measured in the basic ammonothermal environment are summarized in Figure 2-1. Most GaN solubility experiments

have consisted of gravimetric measurements, in which the mass of GaN (either polycrystalline material or HVPE single crystal seeds) added to the autoclave is measured before and after being exposed to an isothermal NH_3 solution, with the resulting mass change considered to have been dissolved in the NH_3 solution during the experiment. The temperatures recorded for these solubility measurements typically refer to the temperature of the external wall of the autoclave. More recently, Schimmel et al. performed solubility measurements using an *in situ* X-ray tomography technique with internal temperature measurement capability, which could resolve dimensional changes of an HVPE seed in real time during etch back, thereby allowing for dynamic determination of the GaN solubility [81]. In general, it has been determined that acidic chemistry exhibits forward, or normal solubility with respect to temperature (i.e., increasing solubility with increasing temperature), whereas basic chemistry exhibits retrograde solubility with respect to temperature (i.e., decreasing solubility with increasing temperature). Notable exceptions to this trend exist for NH_3-NH_4F solutions in the 550-650 °C range, and for NH_3-NH_4Cl solutions above 650 °C, both of which exhibit retrograde GaN solubility [78][86].

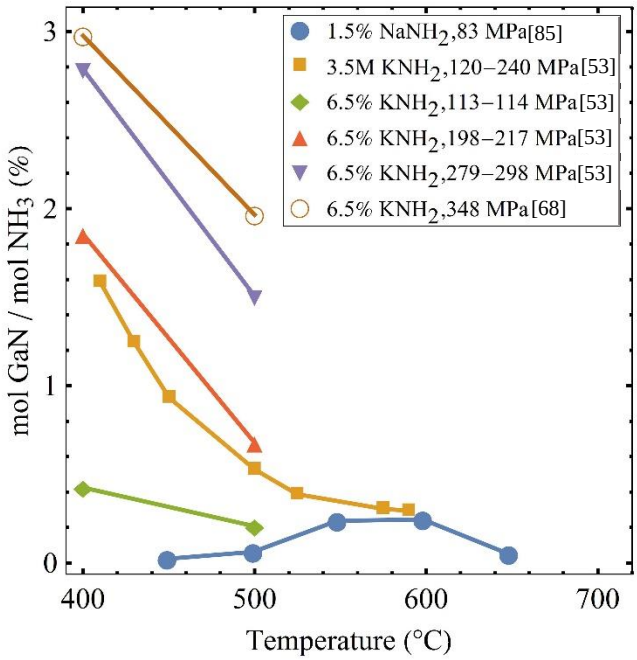

Figure 2-1. Summary of previously measured GaN solubility curves, normalized by NH_3 amount, in basic ammonothermal systems as a function of temperature and pressure. "%" mineralizer content refers to mol.% mineralizer, normalized by NH_3. Lines connecting data sets are added to guide the reader's eye, and are therefore not experimentally-determined. When appropriate, the original data submitted in the referenced work was digitized so as to ensure proper normalization by NH_3 amount.

Our research group has developed expertise with bulk GaN growth in the supercritical NH_3-Na system, including the ability to measure fluid temperatures in the dissolution (T_D^{int}) and growth zones (T_G^{int}) [79]. It was found that crystal growth readily occurs at T_D^{int}= 451 ± 8 °C and T_G^{int}= 505 ± 4 °C, which implies retrograde solubility according to Equation 2-1, but corresponds to the region of forward solubility for the reported $NaNH_2$ mineralizer solubility curve, shown in Figure 2-1 [85]. To resolve this discrepancy and better understand the fundamental driving force for GaN growth in basic ammonothermal systems, further investigations into the solubility of GaN in supercritical NH_3-Na solutions are needed, with a focus on reducing sources of error for a more accurate assessment of the GaN solubility curve under relevant growth conditions: nominally isobaric conditions (peak total system pressure

~200 MPa), with a constant molar NH_3:Na fill ratio (20:1), and a varying internal (actual) fluid temperature (415—650 °C). This paper presents the experimental determination of an improved GaN solubility curve, including corrections for two previously unreported sources of error in the gravimetric determination of GaN solubility.

2.2 Experimental Methods

The solubility of GaN in supercritical NH_3-Na solutions was determined gravimetrically for systems under the relevant ammonothermal conditions previously identified. The mass change of a polycrystalline GaN charge ($w_{GaN}^{i} - w_{GaN}^{f}$) was measured as a function of experiment soak time, autoclave free volume, and fluid temperature by performing 23 experiments under varying conditions. The apparent solubility of GaN, normalized by fill NH_3 ($S_{GaN}^{Fill\ NH_3}$), was determined in mol. % according to Equation 2-2, in which $w_{NH_3}^{fill}$ refers to the weight of fill NH_3 added to the autoclave, and MW_{NH_3} and MW_{GaN} refer to the molecular weight of NH_3 and GaN, respectively.

Equation 2-2

$$S_{GaN}^{Fill\ NH_3}(\%) = mol\ GaN/mol\ Fill\ NH_3\ (\%) = \frac{\left(w_{GaN}^{i} - w_{GaN}^{f}\right)}{w_{NH_3}^{fill}} * \frac{MW_{NH_3}}{MW_{GaN}} * 100$$

Errors in determination of the mass change of the GaN charge were reduced by evacuating the supercritical NH_3-Na solution at working pressure and temperature in less than 1 second, thereby nearly-instantaneously ending the experiment. This experimental design

prevented the possibility of both the dissolution of the GaN charge or nucleation of dissolved GaN on the charge during cooldown.

A dense, white powder was always observed at the bottom of the autoclave after completion of the experiments. The powder is known to contain Na based on its reactivity with water. Evidence will be given which suggests that this powder crystallized from a liquid phase which was present (in addition to the supercritical NH_3-Na solution) during the experiment. It is therefore assumed the Na was present in this second phase during the run as well, and therefore this phase will be referred to as the *Na-rich phase* throughout this work. Although the Na-rich phase was not analyzed in detail and is still under investigation, significant evidence has been presented in the liquid NH_3 and ammonothermal literature to suggest that it is primarily composed of $NaNH_2$ [87][88][42].

Error in the determination of the temperature dependence of GaN solubility was reduced by directly probing the fluid temperature (rather than measuring the external autoclave wall temperature). Corrections to the apparent solubility curve were made by accounting for additional Ga sinks and sources in the autoclave. This was performed by analyzing the mass and chemical composition changes of autoclave components exposed to the ammonothermal environment, in addition to analyzing the mass and chemical composition of the Na-rich phase collected upon unloading the autoclave.

The polycrystalline GaN charge was sourced from Mitsubishi Chemical Co. (MCC), and was produced through parasitic growth on the susceptor and reactor walls during production of HVPE GaN boules. The polycrystalline pieces were crushed and sieved. Special care was taken to select > 3 mm pieces for the GaN charge in each experiment to avoid losing pieces while handling the material. The GaN charge mass was measured using a high precision

balance (Mettler Toledo AB135-S/FACT, precision: ± 0.01 mg). The total mass of the GaN charge was kept above 7 g to ensure that the supercritical NH_3-Na solution was saturated in dissolved GaN, and that dissolution was not surface-limited. The GaN charge was added to a basket constructed of either nickel or nickel-chromium wire mesh (Ni-Cr, with composition 80-20 wt.%, respectively). The GaN-containing basket was placed in a Rene 41 Ni-Cr superalloy autoclave on top of an Inconel 625 standoff, which elevated the basket to ~ 2.5 cm above the bottom of the inner surface of the autoclave wall. Autoclaves of two different sizes were used for these experiments to ensure that the measured solubility did not depend on reactor dimensions (i.e. to prove that the measurements were intensive). The small autoclaves had internal free volumes of 60-70 mL, while the large autoclave had an internal free volume of ~120 mL.

After charging with the GaN-containing basket, the autoclave was placed in a nitrogen-filled glovebox (ambient containing ≤ 1 ppm O_2 and H_2O), where the Na (sourced from Alfa Aesar, 99.95% metals basis purity) was prepared, weighed, and added to the autoclave according to procedures described in Ref. [79]. A high pressure, stainless steel head assembly was attached to the autoclave, which consisted of a feed-through containing an Inconel 625 sheathed Type K thermocouple (accuracy: ± 0.4% of reading), a pressure transducer (Honeywell model with ± 3 MPa accuracy, or Omegadyne model with ± 0.3 MPa accuracy), and a high pressure needle valve. The autoclave was sealed through compression of a nickel gasket (Ni 200/201, > 99% purity).

Once loaded and sealed, the autoclave assembly was taken out of the glove box and weighed with a precision balance (Sartorius MSA14202S, precision: ± 10 mg). The free

volume of the autoclave assembly was measured to within ± 0.1 mL according to procedures described in Ref. [89]. The NH_3 fill was estimated using the NH_3 equation of state previously presented in the literature for the given free volume, target fluid temperature, and target peak total system pressure of 200 MPa [89]. After filling the autoclave assembly with NH_3 (Denko K.K., 99.99995% purity and further purified to ≤ 1 ppb H_2O, O_2, and CO_2 using a Japan Pionics purifier and a SAES MicroTorr point-of-use purifier) and allowing it to warm to room temperature, a post-fill autoclave mass was recorded (Sartorius MSA14202S, precision: ± 10 mg) permitting an additional determination of the NH_3 fill ($w_{NH_3}^{fill}$). The filled autoclave assembly was placed in a ceramic insulated, resistive heater stack and connected to exhaust via stainless steel tubing, a 0.5 μm pore size line filter, and a normally-off, remote-controlled pneumatic valve.

Each experiment was executed by heating the autoclave assembly at a rate of 2 °C/min, and isothermally holding at a target soak temperature for 45—316 hours. A schematic of the complete autoclave assembly at the soak temperature is shown in Figure 2-2, depicting the experimentally-supported, two-phase ammonothermal environment (supercritical NH_3-Na solution phase and dense, Na-rich phase) as is described in the Results and Discussion section. At the conclusion of the desired soak time, the gaseous contents of the autoclave assembly were purged to exhaust by opening the remote-controlled pneumatic valve while the system remained at the soak temperature. The pneumatic valve was closed after approximately 10 seconds to prevent contamination from exhaust. The autoclave assembly was allowed to cool to room temperature over the course of ~ 6 hours, after which it was removed from the containment vessel. In some instances the autoclave assembly was opened in a nitrogen-filled glove box, where the remaining Na-rich powder at the bottom of the autoclave was collected

for further analysis. It should be noted that GaN decomposition (whether in the supercritical NH_3-Na solution, or in the evacuated autoclave post-purge) is expected to be negligible in the temperature range explored for this study (< 650 °C) [90].

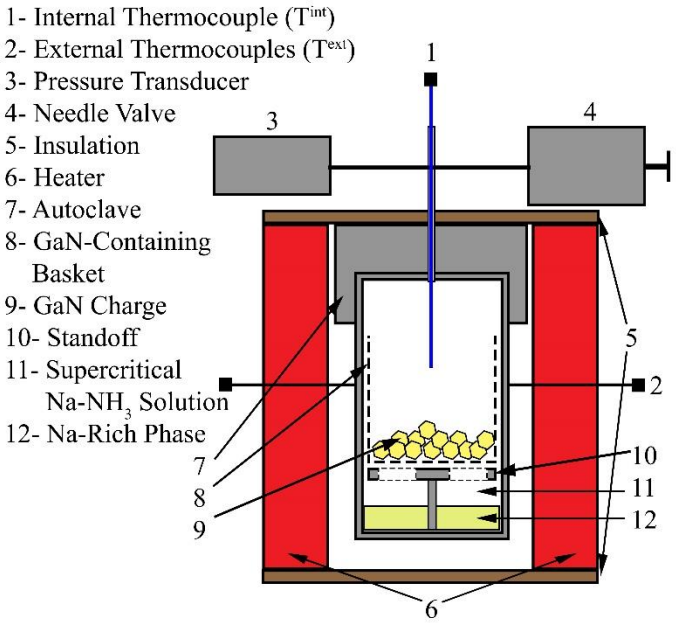

Figure 2-2. Autoclave assembly schematic for GaN solubility experiments in supercritical NH_3-Na solutions at soak temperature. The GaN charge (9) is placed in a Ni (or Ni-Cr) GaN-containing basket (8), atop an Inconel 625 standoff (10) in a Rene 41 autoclave (7). After filling with Na, a stainless steel head assembly is added to the autoclave. The head assembly includes a pressure transducer (3), needle valve (4), and Inconel 625-sheathed internal thermocouple (1). After filling with NH_3, the autoclave assembly is placed in a resistive heater stack (6), in which external thermocouples monitor the external temperature of the autoclave wall (2), and around which insulation (5) is added, so as to maintain a uniform temperature throughout the autoclave volume. The autoclave assembly is then heated to the desired soak temperature, during which evidence suggests that the ammonothermal environment forms two distinct phases: a supercritical NH_3-Na solution phase (11, in which the GaN charge is immersed) and a dense, Na-rich phase (12).

After opening the autoclave, all parts exposed to the supercritical NH_3-Na solution were neutralized in a mixture of deionized water and isopropanol followed by sonication in pure deionized water, then isopropanol. Special care was taken during cleaning to look for pieces of GaN which may have fallen out of the basket, or spontaneously nucleated during the run, though no such pieces were ever observed (including in the tubing leading to the line filter, or

in the line filter itself). After drying, the GaN charge, GaN-containing basket, and standoff were weighed (Mettler Toledo AB135-S/FACT, precision: ± 0.01 mg) to determine their mass change. Heavier parts (the autoclave, stainless steel head assembly, pressure transducer, internal thermocouple, high pressure tubing, and line filter) were weighed using a less precise balance (Sartorius MSA14202S, precision: ± 10 mg).

Cross-sectional samples of the 80-20 Ni-Cr wire mesh (composing some of the GaN-containing baskets) and the Inconel 625 standoff were prepared for chemical analysis. These samples were mounted in epoxy, polished, and then examined using a scanning electron microscope (SEM, FEI XL40 Sirion FEG Digital Scanning Microscope) with energy-dispersive X-ray spectroscopy (EDX) capability (Oxford INCA X-ray system).

The chemical composition of the Na-rich phase collected from the bottom of the autoclave post-experiment was investigated using an inductively coupled plasma (ICP) atomic emission spectrometer (Thermo Scientific, Model: iCAP 6300). The powder was removed from the autoclave in a nitrogen-filled glovebox, ground and mixed using a ceramic mortar and pestle, and weighed in the glovebox (Mettler Toldeo, Model: B303-S, Precision: ±0.5 mg). A portion of the powder was digested in a solution composed of 2 wt.% nitric acid in water. The ICP was calibrated using an acid blank (2 wt.% nitric acid in water, with no dissolved solids added) and a certified 100±1 µg/mL standard solution for elements of interest (Ga, Na, Ni, Cr, etc.) dissolved in a 2% nitric acid matrix (High Purity Standards, Product: ICP-AM-MISA6, Lot: 1511720). A 10x dilution of the certified standard was performed to more narrowly bracket the concentration of dissolved solids in the unknown samples.

2.3 Results and Discussion

Two previously-unreported errors for the gravimetric determination of the solubility of GaN in supercritical NH_3-Na solutions were identified in our study. One error is due to the propensity of Ga to alloy with Ni-containing components in the system. A second error is due to Ga dissolution in the Na-rich phase present at the bottom of the autoclave during the experiment. The presence of a Na-rich phase implies that the solubility limit of Na in supercritical NH_3 was exceeded under the experimental conditions tested. These two phenomena had the ability to act as Ga *sinks* with respect to the supercritical NH_3-Na solution, while the Ni-containing components could act as either Ga *sinks* or *sources*, depending on the experimental conditions. It is assumed these contributions operate concurrently and therefore each must be carefully considered to correct the apparent solubility values determined purely by mass change of the GaN charge.

In the following, each error contribution will be independently discussed. An apparent GaN solubility curve will be presented based on the mass change of the GaN charge. Additionally, temperature-dependent error contributions are provided in Ga solubility plots, for which positive values indicate that Ga was added to the supercritical NH_3-Na solution, and negative values indicate that Ga was removed from the supercritical NH_3-Na solution. The cumulative effect of all Ga solubility error contributions is given in a refined GaN solubility curve as a function of fluid temperature in Figure 2-13.

2.3.1 Gravimetric GaN Charge Measurements

The determination of GaN solubility as a function of temperature by exclusively monitoring mass change of the GaN charge, as is conventionally done for gravimetric

experiments, can be calculated according to Equation 2-2, which normalizes GaN solubility by the NH_3 fill. This is the proper normalization for systems in which the mineralizer has exceeded its solubility limit in supercritical NH_3, as is the case for Na in this study, in which the Na amount dissolved in supercritical NH_3 is not equivalent to the fill Na. The apparent GaN solubility, determined in this fashion, is plotted as a function of fluid temperature in Figure 2-3.

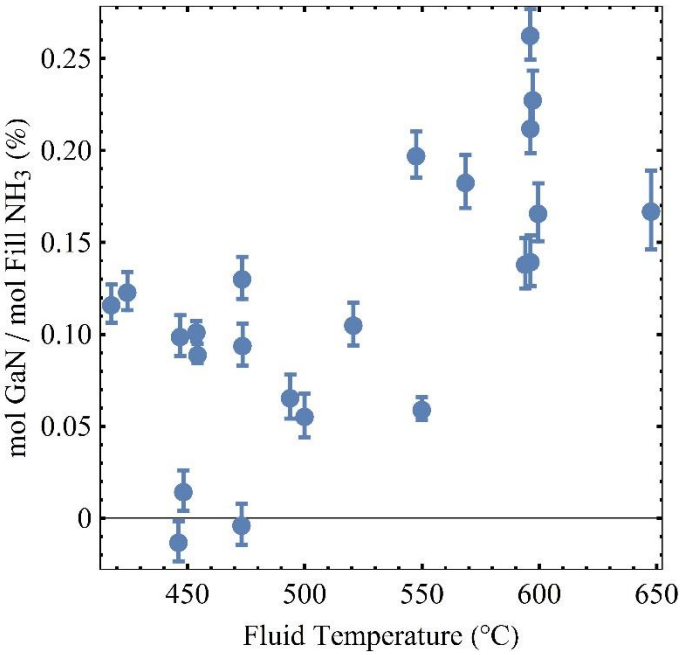

Figure 2-3. Apparent GaN solubility, normalized by fill NH_3, in supercritical NH3-Na solutions as a function of fluid temperature, as determined exclusively by the mass change of polycrystalline GaN charge.

By only considering the mass change of the GaN charge, the solubility of GaN in the supercritical NH3-Na solution would appear to be normal. There is significant scatter in the data, well in excess of the anticipated experimental error range (indicated as error bars, typically +/- 0.02%). Additionally, mass gains on the GaN charge were sometimes measured at low fluid temperatures, indicating that GaN was deposited on the charge during these experiments. There should have been no driving force for GaN deposition on the charge from

the supercritical NH_3-Na solution due to the presumed equilibrium between the charge and the solution under isothermal conditions. This implies that Ga (or GaN) had to exist at a higher activity somewhere else in the system, thereby acting as a Ga (or GaN) source which supersaturated the solution, allowing for GaN deposition on the charge. This Ga (or GaN) source behavior is examined in the following.

2.3.2 Gallium Diffusion in Nickel-Containing Components

The previous gravimetric studies of GaN solubility in the basic ammonothermal environment were performed in Ni-based autoclaves, and as such one may speculate on the possibility of Ga-Ni compound formation, given known binary Ga-Ni phase behavior at temperatures relevant to ammonothermal growth [91]. A study on the corrosion behavior of Inconel 718 autoclaves in the basic ammonothermal growth environment identified the formation of a surface nitride layer on the inner autoclave wall using EDX, but the authors did not report on the presence of Ga in the alloy [45]. Ga was however identified in all Ni-containing components in this study, and an attempt to quantify the effect of Ga-alloying in each component on the solubility of GaN in supercritical NH_3-Na solutions was conducted.

2.3.2.1 *Gallium in GaN-Containing Basket (Ni and 80-20 Ni-Cr wires)*

EDX analysis was performed on 80-20 Ni-Cr wire cross-sections, cut normal to the axial direction of the wire. The wires originated from woven mesh parts of two GaN-containing baskets which were exposed to supercritical NH_3-Na solutions at various temperatures for over 1000 hours each. A representative SEM micrograph near the surface of the Ni-Cr wire is shown in Figure 2-4a), with the chemical composition measured using EDX given as a function of depth into the wire in Figure 2-4b).

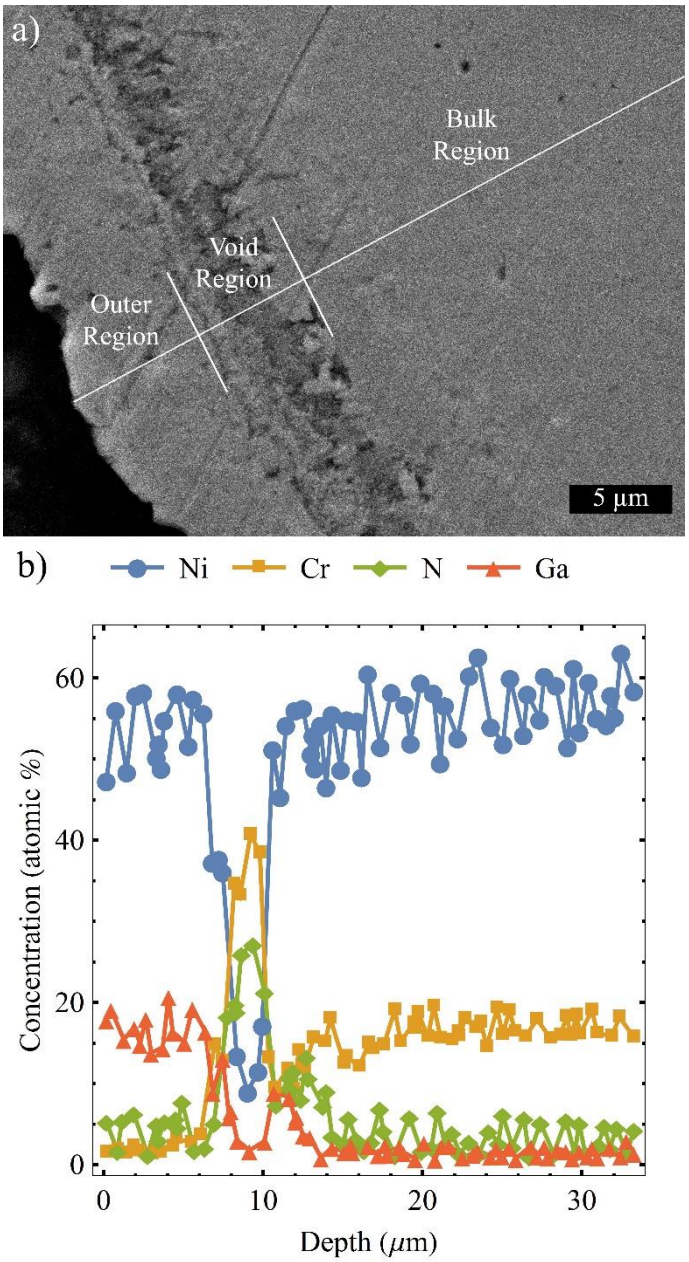

Figure 2-4. a) Representative Ni-Cr wire cross-section SEM micrograph, showing the path (in white) along which the b) corresponding chemical composition was measured using EDX. For clarity, some dilute contaminate elements are excluded from the plot.

As can be seen in Figure 2-4, there are three distinct regions of the Ni-Cr wire: an outer region near the wire surface, characterized by high relative concentrations of Ni and Ga; a region of voids roughly 5-10 µm from the wire surface, characterized by high relative

concentrations of Cr and N (and reduced Ni and Ga); and a bulk region with high, relatively uniform concentrations of Ni and Cr (and reduced Ga and N). The composition of the outer region indicates that the wire did not continuously nitride, as one would anticipate a decreasing N-concentration gradient into the wire if the process was diffusion driven. What is instead observed is a high N-concentration solely in the void region, which scales with Cr concentration, suggesting chromium nitride formation. This nitride layer may have formed upon initial exposure to a heavily-nitriding environment. Subsequent experiments may have caused Ga to deposit on the surface and to alloy with Ni which diffused from the bulk through the nitride layer (possibly forming the voids shown in Figure 2-4). While further investigations are needed to determine the underlying mechanisms of initial formation of the Ga and Ni-containing surface, its presence is unambiguous evidence that Ga and Ni alloy under ammonothermal conditions.

For this study, it is assumed that Ni is not soluble in the NH_3-Na solution, that the Ga-Ni alloy presents a considerable diffusion barrier for inward N diffusion (to form additional chromium nitride), and that the Ga-Ni alloy was already present for the first solubility experiments, as the baskets were exposed to supercritical NH_3-Na solutions containing Ga-species prior to this study for at least 450 hours. With these assumptions, the mass change of the GaN-containing basket can be completely associated with Ga uptake or loss to/from the Ga-Ni alloy.

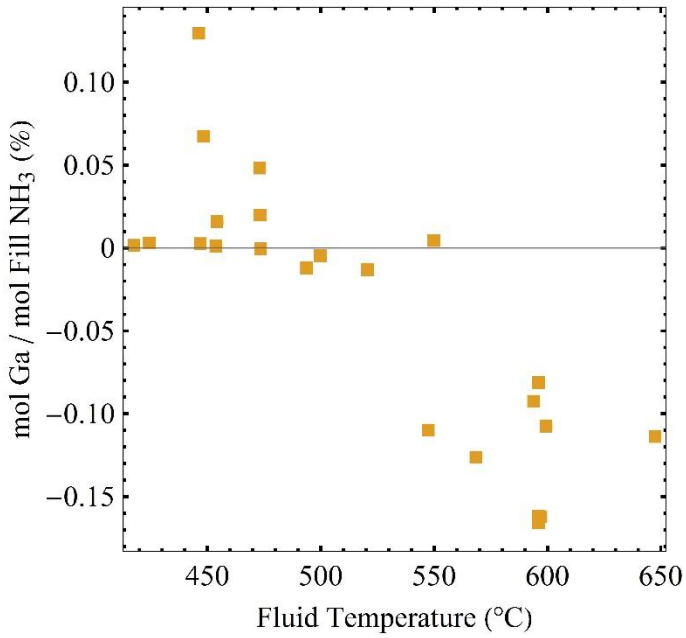

Figure 2-5. Ga solubility, normalized by fill NH_3, added to (or subtracted from, if negative) the supercritical NH_3-Na solution as a function of fluid temperature, based on the mass change of the GaN-containing basket.

Figure 2-5 presents the moles of Ga, normalized by fill NH_3, added to (or subtracted from, if negative) the supercritical NH_3-Na solution based on the mass change of the GaN-containing basket for each experiment. It is reasonable to assume that the extent to which dissolved Ga from the supercritical NH_3-Na solution can alloy with the Ga-Ni surface of the wire is dependent on at least three factors (if diffusion-limited): the temperature of the system (this dependence is shown in Figure 2-5), the exposure time of the wire to the solution, and the difference in chemical potential between Ga in the solution and Ga in the wire. Additional experiments are required to elucidate the effect of exposure time on the mass change of the GaN-containing basket. It is more complicated to understand the chemical potential gradient of Ga between the solution and the wire, as one would need a priori knowledge of the solubility of Ga in supercritical NH_3-Na solution. However, the effect of this chemical potential gradient can be thought of qualitatively in terms of a *memory effect*.

All previous experiments dictate how much Ga has alloyed with the GaN-containing basket prior to each subsequent experiment, thereby fixing the chemical potential of Ga in the wire once the wire reaches thermal equilibrium with the solution. Therefore, the scatter observed in Figure 2-5 is expected, as most solubility experiments were conducted at different soak times, and most GaN-containing baskets were exposed to different temperatures and soak times in previous experiments.

2.3.2.2 *Gallium in Standoff (Inconel 625)*

Inconel 625 is a Ni-Cr alloy with additional alloying constituents. It contains a comparable amount of Cr as the 80-20 Ni-Cr alloy (~ 20—23 wt. %) and as such it could behave similarly to the previously discussed 80-20 Ni-Cr wire. EDX analysis of an Inconel 625 standoff cross-section sample suggests Ga-alloying occurred in the surface layer (see Figure 2-6).

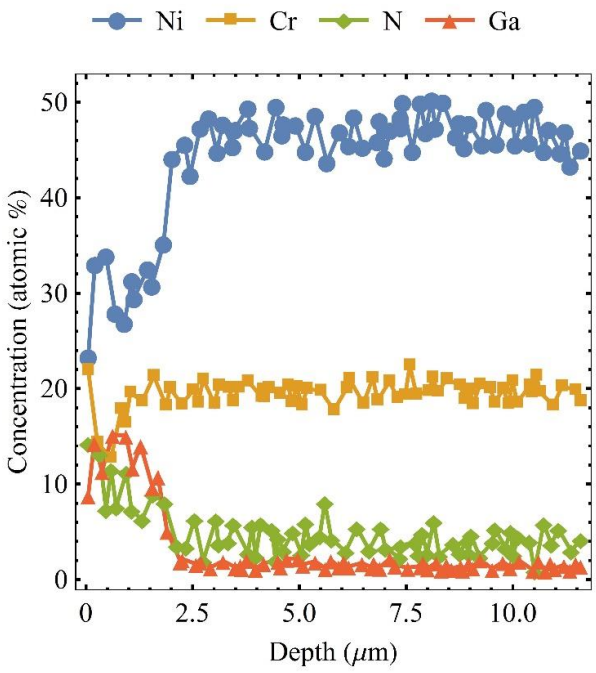

Figure 2-6. Representative chemical composition (measured by EDX) of an Inconel 625 sample cross-section, which was exposed to supercritical NH_3-Na solutions with dissolved Ga. For clarity, some dilute alloying elements are excluded from the plot.

In contrast to the 80-20 Ni-Cr wire, the Inconel 625 material exhibited a smooth tail of N into the bulk and a depletion of Ni and Cr on the surface. As continuous nitriding of Inconel 625 may be possible, mass changes of the Inconel 625 standoff can be attributed to Ga uptake or depletion from/to the supercritical NH_3-Na solution, N uptake, and leeching of alloying elements into the NH_3-Na solution. Given the uniform distribution of alloying elements as a function of depth (not shown in Figure 2-6) and the larger atomic mass of Ga as compared to N, it will be assumed for the purposes of this study that any mass change of the Inconel 625 standoff is only due to Ga uptake or depletion.

Figure 2-7 presents the moles of Ga, normalized by fill NH_3, added to (or subtracted from, if negative) the supercritical NH_3-Na solution based on the mass change of the Inconel 625 standoff for each experiment. As is evident in comparing Figure 2-5 and Figure 2-7, the effect is substantially smaller than the contributions from the GaN-containing basket, partially due to the ~20—40x smaller surface area of the standoffs. There is also scatter in the temperature dependence of Ga solubility attributed to the standoff, which can once again be explained by the *memory effect* of Ga in the standoff from previous experiments, and from various soak times at different temperatures.

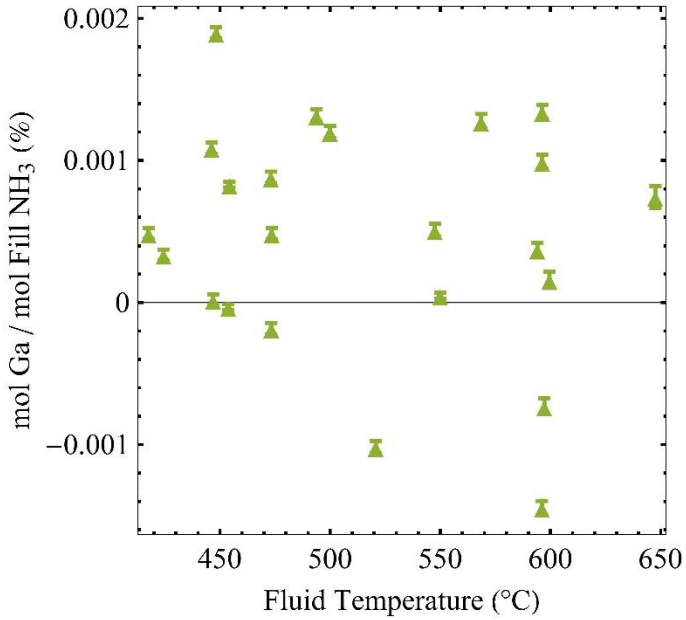

Figure 2-7. Ga solubility, normalized by fill NH_3, added to (or subtracted from, if negative) the supercritical NH_3-Na solution as a function of fluid temperature, based on the mass change of the Inconel 625 standoff.

2.3.2.3 *Gallium in Autoclave Wall (Rene 41)*

Experimental verification of the Ga-alloying effect in Rene 41 was conducted to determine if correction to the apparent GaN solubility curve was necessary for the autoclave wall. After conducting a 600 °C solubility experiment, an autoclave was neutralized, rinsed with deionized water and isopropanol, and allowed to dry. A pure Ni foil (99.5% metals basis purity) was then placed inside the empty autoclave and re-run at the previous experimental conditions (600 °C, 164 hour soak time, 20:1 molar NH_3:Na fill ratio) to act as a Ga sink for dissolved Ga from the autoclave wall. The mass change of the Ni foil was +47.04 mg. EDX analysis was performed on a cross-section of the Ni foil sample (see Figure 2-8). It is evident that the mass increase of the Ni is primarily due to Ga-uptake, which could only have been sourced from the Rene 41 autoclave wall in this experiment.

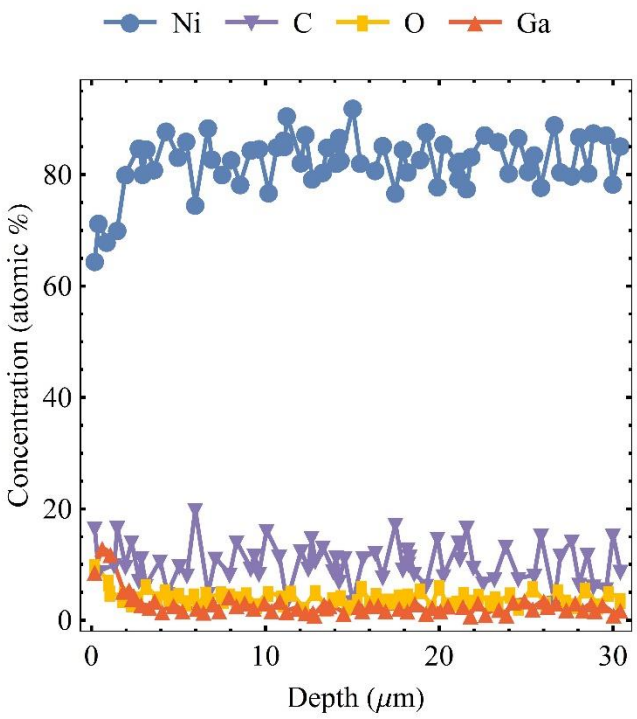

Figure 2-8. Representative chemical composition (measured by EDX) of a Ni foil sample cross-section, which was exposed to supercritical NH_3-Na solution at 600 °C. The Ga observed in the surface layer could only originate from the autoclave wall. For clarity, some dilute contaminate elements are excluded from the plot.

Knowledge of the *memory effect* of Ga in the autoclave wall was only gained towards the end of this study, and mass change of the autoclave can be attributed to several factors, making it impossible to determine its effect on Ga solubility by direct mass change measurements of the autoclave. Given accurate information on the mass change of the Inconel 625 standoff, and assuming the Rene 41 autoclave wall material behaves comparably (they have similar amounts of Ni: ~55-69 wt. % and ~47-59 wt. %; and similar amounts of Cr: ~20-23 wt. % and ~18-20 wt. %, for Inconel 625 and Rene 41, respectively), the mass change of the Inconel 625 standoff was extrapolated to the nominal surface area of the autoclave inner wall for each experiment. Estimated errors for this extrapolation are ~50% due to the surface roughness of both components. The moles of Ga, normalized by fill NH_3, added to (or

subtracted from, if negative) the supercritical NH_3-Na solution based on this extrapolation are shown in Figure 2-9. An experimentally-determined lower bound estimation of ~0.05 mol. % Ga (normalized by fill NH_3) dissolved in the autoclave wall from the supercritical NH_3-Na solution at 600 °C can be calculated using the mass gain of the Ni foil, as previously described. Therefore, it is likely that the Ga solubility plotted in Figure 2-9 is an underestimation as it pertains to autoclave wall effects.

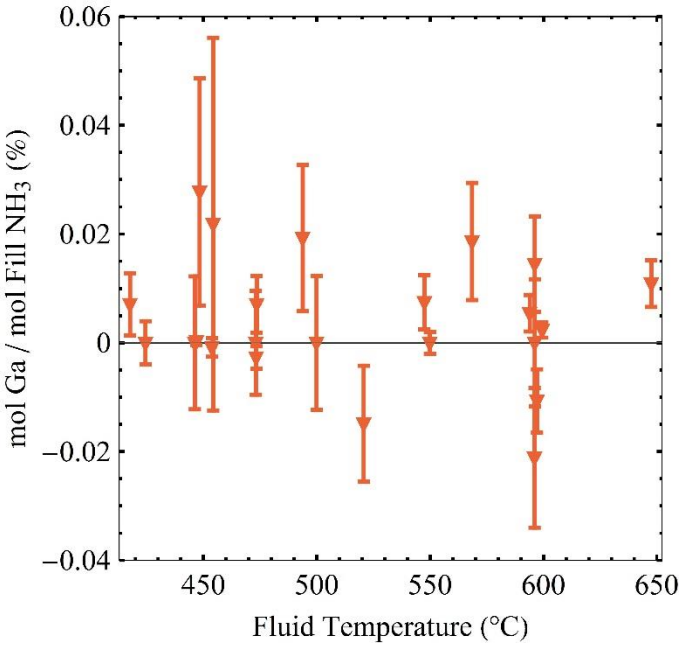

Figure 2-9. Ga solubility, normalized by fill NH_3, added to (or subtracted from, if negative) the supercritical NH_3-Na solution as a function of fluid temperature, based on the mass change of the Inconel 625 Standoff which was extrapolated to the surface area of the Rene 41 Autoclave wall.

It should be noted that the cleaning process of the autoclave after each experiment was inconsistent: for certain runs abrasives were used to remove the nitride surface layers, whereas for others abrasives were not used. Removal of the surface layer is anticipated to remove an unverified amount of retained Ga from the autoclave wall. For runs performed in previously abrasive-cleaned autoclaves, the autoclave wall was not treated as a Ga-source for the

supercritical NH_3-Na solution, and as such the autoclave wall extrapolation was taken as 0 in Figure 2-9.

2.3.3 Gallium in Sodium-Rich Phase

Although the solubility of Na in liquid NH_3 has been extensively studied, there has been no published effort to measure the solubility of Na in supercritical NH_3 [92][93]. The following evidence collected in this study would suggest that the 20:1 NH_3:Na molar filling concentration used in these GaN solubility measurements exceeded the solubility limit of Na in supercritical NH_3 under the explored conditions, thereby allowing for the presence of a Na-rich second phase (most likely through the reaction of Na with NH_3 to form $NaNH_2$) in the autoclave during each experiment. Due to the rapid evacuation (< 1 second) of the autoclave at elevated temperatures at the conclusion of each experiment, the corresponding momentum of the supercritical NH_3-Na solution being evacuated, and the lack of visible streaking down the autoclave wall (which would be present if molten Na-species came out of solution and fell to the bottom of the autoclave), we believe the Na-containing powder was present in the liquid state during each experiment. This material present at the bottom of the autoclave (on the order of grams) excludes the small amount of Na-containing powder (on the order of milligrams) which was observed in the tubing connecting the autoclave to the line filter, and the Na-containing powder in the line filter itself (on the order of tens to hundreds of milligrams). The Na-containing powder observed in the tubing was thought to be transported from the autoclave during each experiment due to the large temperature gradient between the autoclave and the initial length of tubing. However, the Na-containing powder in the line filter was thought to be crystallized from the rapid evacuation process, as the temperature gradient between the final length of tubing and the line filter during the experiment was small, and the only interaction of

hot gas effluent with the high surface area line filter occurred during the evacuation process. Further evidence for the presence of the Na-rich second phase includes consistently observed changes in surface coloration across a distinct interface on the Inconel 625 standoff, which varies in height with varying fill Na content. Similar observations suggest that this second phase is present during growth experiments as well.

As the ability of the Na-rich phase to absorb Ga is unknown, six dedicated experiments at different temperatures were performed to collect the Na-rich powder post-run. ICP analysis was then conducted on two sample dilutions from each powder, so as to determine the precision of the Ga-concentration measurement of the tool. The moles of Ga dissolved in the Na-rich powder (determined from the ICP Ga-concentration measurement and the mass of the powder, normalized by the moles of fill Na) is plotted as a function of the fluid temperature of each of these six experiments in Figure 2-10.

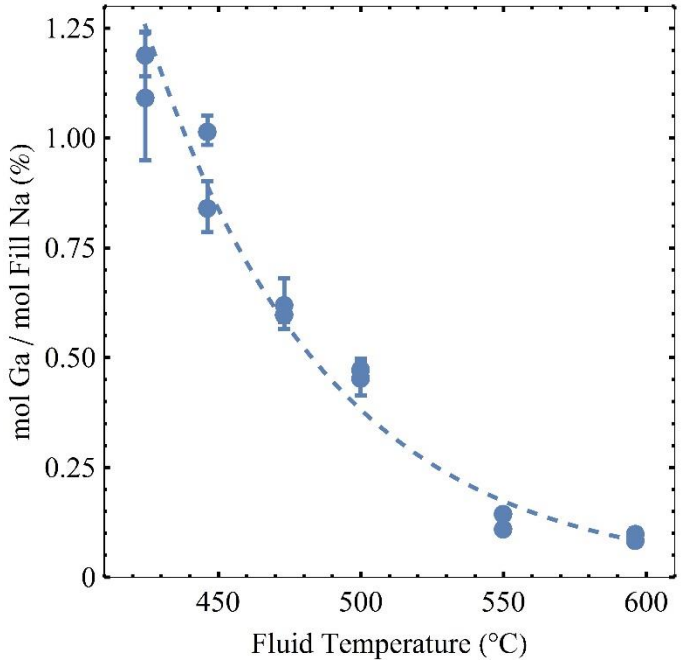

Figure 2-10. Ga solubility in the Na-rich powder, normalized by fill Na, as a function of the fluid temperature. The dashed line provides an exponential fit to the data.

It should be noted that the 550 °C experiment was conducted in the large volume autoclave, while all other experiments in this series were conducted in the small volume autoclaves. Additionally, the mass of Na added to each autoclave was adjusted to provide a nominal NH_3:Na molar fill ratio of 20:1, with the fill NH_3 being adjusted to target a nominal total system peak pressure of 200 MPa. As such, the mass of Na added to the autoclaves was different for each temperature. It is apparent from Figure 2-10 that Ga dissolution in the Na-rich phase has an intensive, exponential correlation with temperature, indicating Arrhenius behavior.

It is assumed that the measured Ga dissolution in Figure 2-10 is repeatable and can be applied (with an exponential fit to the data) to all other solubility experiments. As such, Figure 2-11 shows the moles of Ga, normalized by fill NH_3, lost from the supercritical NH_3-Na solution (represented by negative values) based on the Na-rich phase *sink* behavior. The contribution to error in Ga dissolution is estimated from the accuracy of the ICP tool, as this value exceeds the error calculated from the coefficient of determination (R^2) based on the exponential fit to the data. It should be noted that the mass of the aforementioned Na-containing powder observed in the tubing connecting the autoclave to the line filter was too small to support an appreciable dissolved Ga mass ($<10^{-4}$ mol. % Ga, normalized by fill NH_3), and as such its contribution as a Ga sink was neglected in this study. As the Na-containing powder in the line filter was thought to be transported from the solvent during the rapid evacuation process, its contribution as a Ga sink was also neglected.

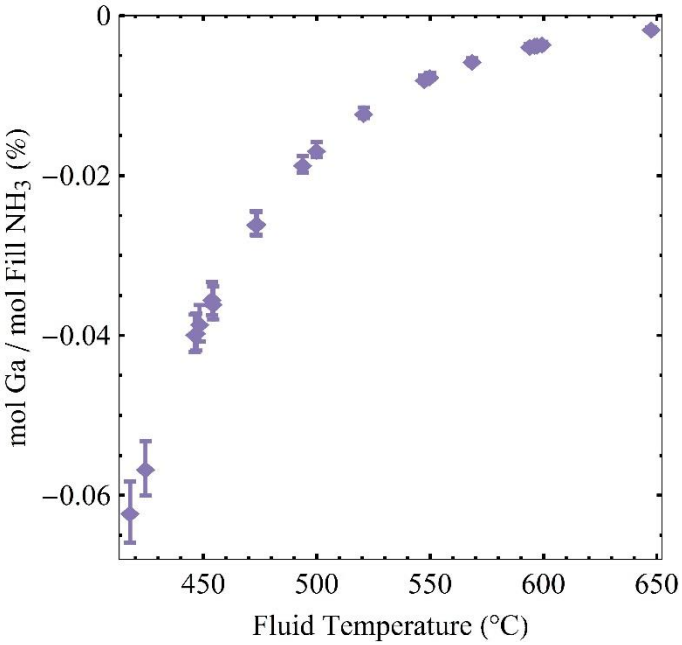

Figure 2-11. Ga solubility, normalized by fill NH_3, lost from the supercritical NH_3-Na solution (indicated by negative values) as a function of fluid temperature, based on the mass of Ga measured in the Na-rich powder.

2.3.4 GaN Dissolution Kinetics

Kinetic GaN solubility series were performed as a function of soak time at two temperatures, 450 °C and 600 °C, to ensure that the treatment of the solubility data was correct (including the correction of GaN solubility for all known Ga *sources* and *sinks*) and that the

supercritical NH_3-Na solutions reached saturation. Figure 2-12 displays these kinetic series at the specified temperatures.

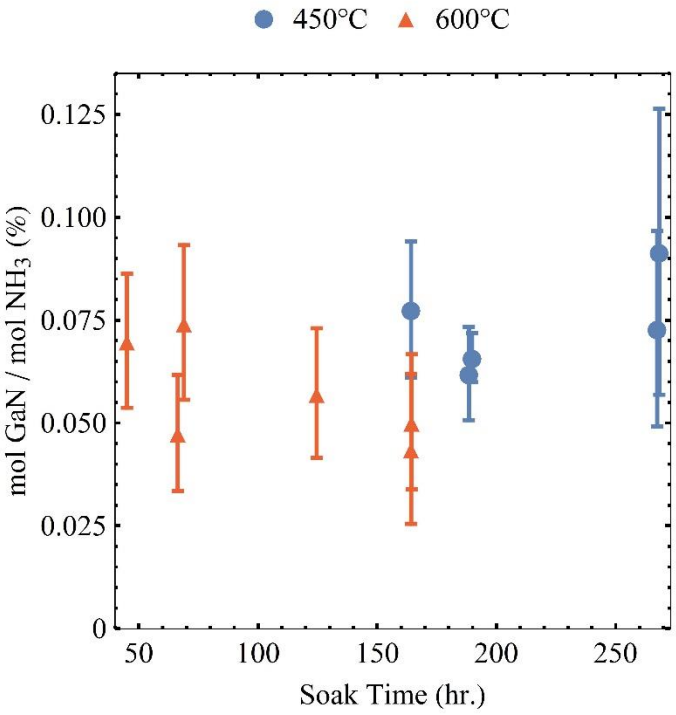

Figure 2-12. Refined GaN solubility, normalized by fill NH_3, as a function of soak time for experiments performed at 450 °C and 600 °C.

As is apparent in Figure 2-12, there is no obvious positive correlation of GaN solubility with soak time at either temperature. This suggests that the supercritical NH_3-Na solution was saturated with GaN in less than 45 hours for the 600 °C experiments, and less than 164 hours for the 450 °C experiments. All GaN solubility experiments were therefore conducted for longer durations than these soak times to ensure saturation of the supercritical NH_3-Na solution. It is possible that that the apparent drop in GaN solubility with increasing soak time at 600 °C indicates an overestimate for the Ga-alloying effect in the autoclave wall at long soak times, or an underestimate for this same effect at short soak times.

2.3.5 Refined Solubility Curve

The various contributions of dissolved Ga to supercritical NH_3-Na solutions discussed in this work are summed in Figure 2-13, yielding a more accurate GaN solubility curve.

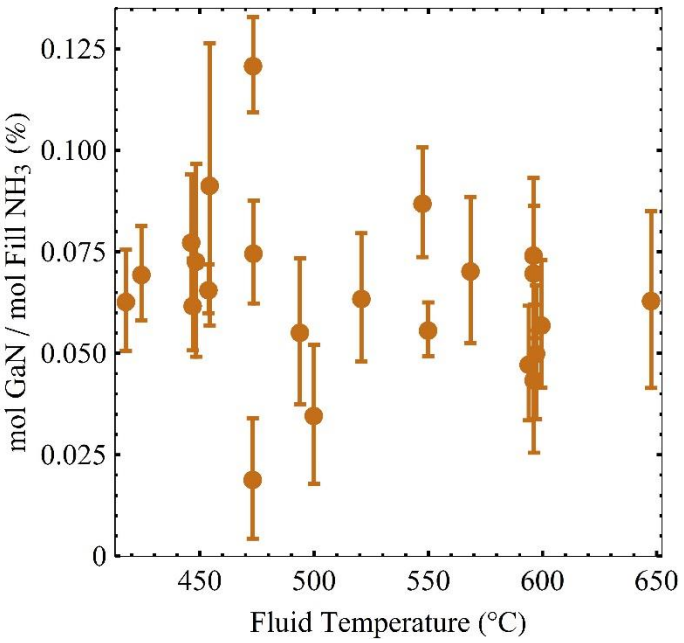

Figure 2-13. Refined GaN solubility in supercritical NH3-Na solutions, normalized by fill NH_3, as a function of fluid temperature, accounting for all discussed data corrections for Ga sources/sinks.

It is apparent from Figure 2-13 that the GaN solubility magnitude measured in this study is lower than previously measured by Hashimoto et al [85]. Furthermore, a clear retrograde dependence of GaN solubility with respect to temperature (as one would anticipate from growth conditions) cannot be determined from Figure 2-13, due to the scatter and experimental errors in the data. Two dominant, temperature-dependent, competing trends can be noted from Figure 2-5 and Figure 2-11, respectively: the GaN-containing basket depletes Ga from the supercritical NH_3-Na solutions at temperatures above 475 °C (while enriching the

supercritical NH_3-Na solutions with Ga below 475 °C), and the Na-rich phase depletes less Ga from the supercritical NH_3-Na solutions at high temperatures as compared to low temperatures (as dictated by an exponential dependence). These trends act to flatten the refined solubility curve with respect to fluid temperature, as shown in Figure 2-13.

There are a few possibilities that might result in the scatter observed in Figure 2-13. As discussed previously, there are memory effects present in all Ni-containing components in the system. These effects were explicitly measured for the GaN-containing basket and the Inconel 625 standoff, but not for the autoclave wall. Evidence was presented to suggest that the extrapolation of the Inconel 625 standoff was insufficient to correct for uptake/depletion of Ga to/from the Rene 41 autoclave wall, thus it is likely that Ga-alloying of the autoclave wall played a significant factor in this scatter. It is also possible that the extrapolation used for the Ga dissolution in the Na-rich phase was not sufficiently accurate to correct all of the solubility data with. The experiments used to generate the Na-rich powder, which was further analyzed using ICP as the basis for this extrapolation, were all conducted in autoclaves which were treated with abrasives prior to use. It is possible that some additional Ga from the autoclave wall was dissolved in the Na-rich phase in experiments with autoclaves not treated with abrasives.

The evolution of H_2 through the anticipated formation of $NaNH_2$, NH_3 decomposition, and related loss of H_2 from the system due to outward diffusion at higher temperatures were not considered for this study and could also affect the results. While all solubility data for this study was normalized by the initial fill NH_3, further investigations are needed to determine the equilibrium chemical composition of the supercritical NH_3-Na solution. This will enable the

determination of true GaN solubility with respect to Na concentration in the supercritical fluid, and with respect to the equilibrium solvent composition (NH_3, N_2, and H_2).

2.4 Summary

An accurate determination of GaN solubility in supercritical NH_3-Na solutions has been reported through the course of 23 gravimetric solubility experiments under ammonothermal conditions (T = 415-650 °C, P ≈ 200 MPa, molar NH_3: Na fill ratio = 20:1). The band of GaN solubility, mostly within 0.03-0.10 mol. % GaN, normalized by fill NH_3, was found to be lower than the previously reported range: 0.023-0.245 mol. % GaN, normalized by fill NH_3 (for 1.5 mol% $NaNH_2$ in NH_3) [85]. This analysis indicated that there was no peak in GaN solubility at 600 °C (within the precision of these measurements), which was previously reported in the $NaNH_2$ study [85]. The target total system peak pressure in our study was 200 MPa, whereas the previous $NaNH_2$ study targeted 83 MPa, which could also impact the disparity in solubility results [85].

Two previously unreported error sources were identified in the gravimetric determination of GaN solubility in the NH_3-Na system under the explored ammonothermal conditions: Ga-alloying of Ni-containing components (identified using EDX), and Ga dissolution in the Na-rich, second phase (identified using ICP). In general, Ni-containing components depleted Ga from the supercritical NH_3-Na solution at high temperatures (> 475 °C), while the Na-rich phase depleted more Ga from the NH_3-Na solution at lower temperatures than at higher temperatures. The aforementioned error sources, and corrections thereof, are thought to be mostly responsible for the accurate refinement of the gravimetric solubility curve from an operational standpoint (i.e. excluding solubility dependence on the equilibrium solvent composition). While new sources of error cannot be ruled out, the observed scatter which was

introduced in the refined GaN solubility curve is thought to be a result of the inability to measure Ga-alloying of the exposed autoclave wall for each experiment. This led to the inability to measure a clear temperature dependence of GaN solubility.

Chapter 3 The Effect of Fluid Temperatures on Bulk Gallium Nitride Crystal Growth in Supercritical Ammonia-Sodium Solutions

3.1 Motivation

As previously described, the ammonothermal literature has many reports demonstrating then-record growth rates, impurity incorporation, crystal quality, and defect structures. In addition to "hero" result demonstration publications, sometimes an attempt to correlate these metrics with externally-controlled experimental parameters (such as external autoclave temperature gradients, autoclave/liner material selection, etc.) is made [78][79]. Also, there has been an extensive effort to measure the properties of supercritical ammonia solutions, including viscosity [94], GaN solubility and dissolution kinetics [81][95], the effect of solution chemistry on material stability [45][47], and the ammonia equilibrium constant in the ammonothermal growth regime [89]. Despite these growth metric and fluid characterization publications, at present there exist no reports attempting to correlate directly-measured internal fluid temperatures with bulk GaN growth metrics. The reasoning for this may be two-fold: 1) introducing thermocouple probes into the growth environment is challenging due to the high system pressure and flow-restriction baffle geometry, and 2) researchers may wish to withhold this information from the scientific community at large in order to maintain a competitive advantage over other research groups, especially if they are part of a commercial enterprise.

The lack of available information linking growth metrics of bulk GaN crystals with the specific fluid properties they were grown in makes scaling and improving the ammonothermal method very challenging. For instance, if researchers desire to increase bulk GaN boule thickness, the autoclave bore diameter provides an upper bound for allowable boule size. When this was attempted at UCSB by scaling autoclave size from a one inch diameter bore to a two inch diameter bore, it was found that growth rates were dramatically reduced. This is presumably because the fluid temperatures will vary by heater and insulation placement, autoclave material and wall thickness, baffle open area and placement in the bore, and bore size. This scenario is also applicable to research groups at different institutions comparing growth metrics with one another. Unless the same exact experimental setup and procedure is utilized, the possibility of different dissolution and growth zone fluid temperatures cannot be excluded.

For a scientist to fully understand a crystal growth process, they must know the thermodynamic and kinetic limitations of the system they are utilizing. Thermodynamic knowledge, such as the temperature coefficient of solubility, can allow one to change the chemical potential driving force for crystal growth in the ammonothermal system (if independent control of dissolution and growth zone temperatures is possible) [95]. Chemical potential driving force determines whether it is thermodynamically favored for crystals to grow from or dissolve into solution, it affects the size of critical nucleus formation, and it can determine the growth mode by which seeded crystal growth occurs [96]. Kinetic processes in ammonothermal crystal growth include source dissolution rate, solute diffusivity, surface attachment and desolvation of mineralizer and solvent species from growth intermediates, growth unit diffusion along crystal surfaces, incorporation of growth units into kink sites, and

the transport of the heat of crystallization from the crystal surface [97]. The aforementioned thermodynamic and kinetic processes are functions (directly or indirectly) of fluid temperatures, and as such, a direct measurement of fluid temperatures in the growth environment may elicit a greater understanding of the limitations of ammonothermal crystal growth. What follows in this chapter is an attempt to correlate the dissolution and growth zone fluid temperatures with as-grown bulk GaN crystal growth kinetics, crystal quality, and impurity incorporation.

3.2 Experimental Methods

Ammonothermal crystal growth was performed on {0001} and {10$\bar{1}$0} orientation HVPE GaN seed crystals in supercritical NH_3-Na solutions at various internal fluid temperature conditions. It should be noted that the {10$\bar{1}$0} crystals had a nominal 2° miscut towards <0001> to allow nucleation to occur more readily. In total, 12 week-long growth experiments were performed, with varying quantities and positioning of the aforementioned seed crystal orientations. The total system peak pressure ranged from 181 MPa to 263 MPa for these experiments.

To measure the internal fluid temperature in the dissolution and growth zones of the autoclave, Inconel-sheathed type K thermocouple probes were inserted into each respective zone. The convection baffles and crystal hanging stand described in previous UCSB publications, and the loading procedure itself, were therefore redesigned to allow access of these thermocouple probes into the growth environment [79]. Traditionally, holes in seed crystals were drilled such that they could be a hung on a stand placed at the bottom of the autoclave blind bore. The baffles were then placed on top of the crystal hanging stand, above which a basket filled with polycrystalline GaN was placed. This stacking sequence of crystals

and components is sufficient to grow in a retrograde solubility regime, but it suffers from two key disadvantages: 1) the stand, baffles, and basket are only held in place by gravity, and it is possible that each component may shift with respect to each other during manipulation of the autoclave and during the experiment in the presence of strong fluid flow, thereby potentially changing fluid temperatures and flow patterns, and 2) there is no way to probe the growth zone fluid temperature, as the autoclave is designed with a blind bore (permitting only access from the top). In this study, the crystal hanging stand and baffle plates were assembled as a monolithic piece, referred to as the furniture assembly, and fixed in space with respect to the autoclave nozzle. The furniture assembly was held together by Ni99 alloy rods, running almost the entire axial length of the autoclave bore, and preventing movement of any of the component pieces. By inserting the thermocouple probes through the nozzle and furniture assembly, loading the requisite chemistry (GaN seed crystals, polycrystalline GaN source material, and Na mineralizer), sealing the autoclave, and finally filling with NH_3, measurement of each temperature zone was made possible.

In this study, the baffle open area and hole pattern was kept the same as previous UCSB growth efforts. Also, the baffle plate spacing and positioning with respect to the external resistive heater stack was maintained to be consistent with previous UCSB growth studies. The origins of this design come from reports in the quartz hydrothermal growth literature [98][99]. A cross-section of the experimental setup is shown in Figure 3-1. The furniture assembly includes three baffle plates, separated from each other by 0.75 inches. The top-most baffle plate has four holes drilled off-center, clocked at 90° with respect to one another. The holes and annulus between the autoclave bore and baffle plate outer diameter combine to yield an 8% open area with respect to the 1 inch autoclave bore opening. The middle baffle plate has

one large hole drilled at the center, yielding a 10% open area (also including the annulus formed between the autoclave bore and baffle plate outer diameter). The bottom-most baffle plate has the same design as the top-most baffle plate. A consequence of this baffle stack design is that there is no line-of-site down the axis of the autoclave bore, excluding the area left open between each baffle plate outer diameter and the autoclave inner wall.

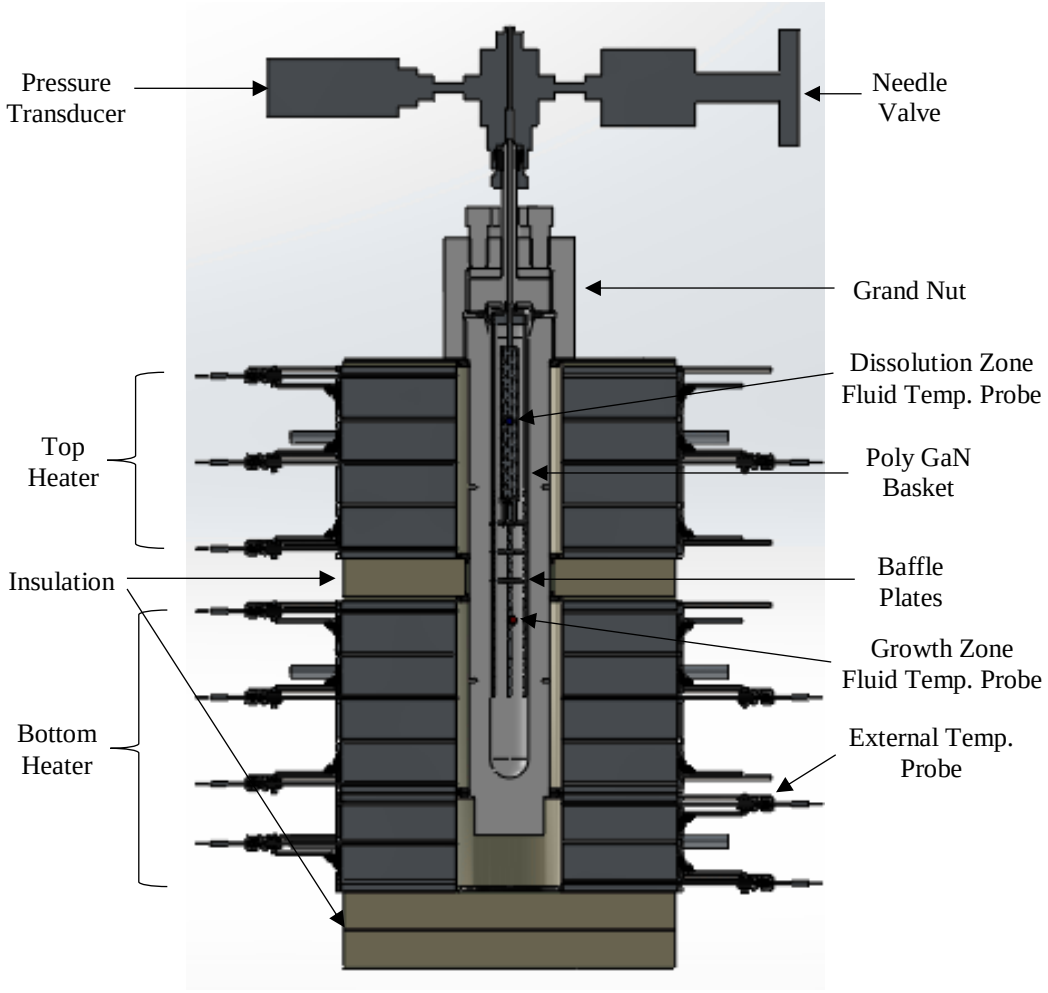

Figure 3-1. Cross-section of the experimental setup, showing the resistive heater stack, autoclave assembly, and furniture assembly. The blue circle in the top portion of the autoclave (located inside the poly GaN basket) represents where the dissolution zone fluid temperature is measured, while the red circle represents where the growth zone fluid temperature is measured.

To determine the range of achievable dissolution and growth zone fluid temperatures using this baffle scheme, a temperature series was conducted at different top heater and bottom heater external temperatures with the experimental setup shown in Figure 3-1. It should be noted that, as indicated in Figure 3-1, the grand nut was neither directly heated nor insulated. The external temperature range has an upper bound determined by an increased likelihood of creep rupture of the autoclave. For the Rene 41 autoclaves used in this study, this temperature was limited to 650°C at the ammonothermal pressures of interest. Figure 3-2 and Figure 3-3 show the dissolution zone and growth zone fluid temperatures, respectively, as a function of top and bottom heater temperature setpoint. The solid black points which appear on the contour plots indicate conditions that were directly measured, with the contours between said points linearly interpolated. Figure 3-4 demonstrates the difference between growth and dissolution zone fluid temperatures (positive values indicate that the growth zone was hotter).

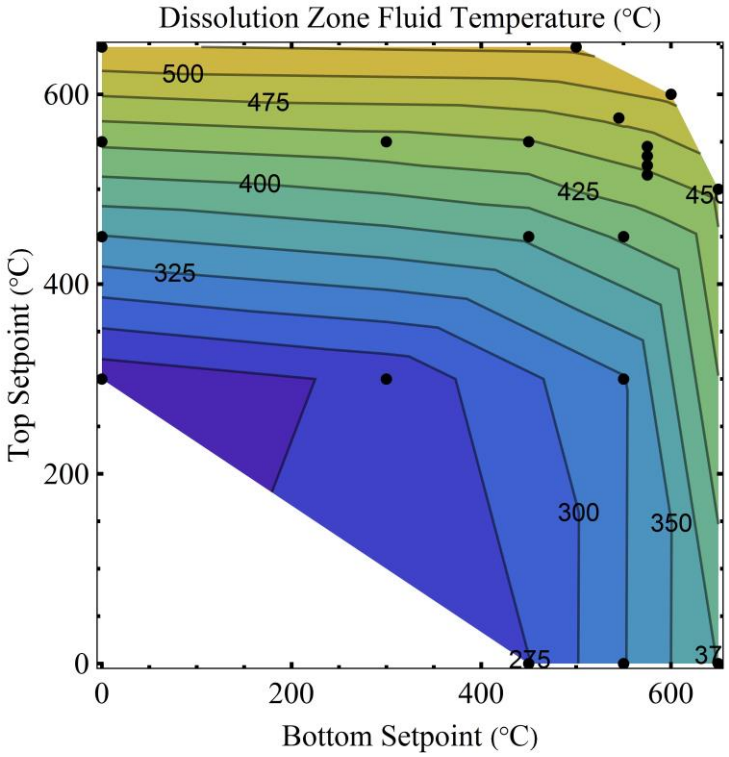

Figure 3-2. Dissolution zone fluid temperature contours as a function of top and bottom heater setpoint with uninsulated grand nut configuration.

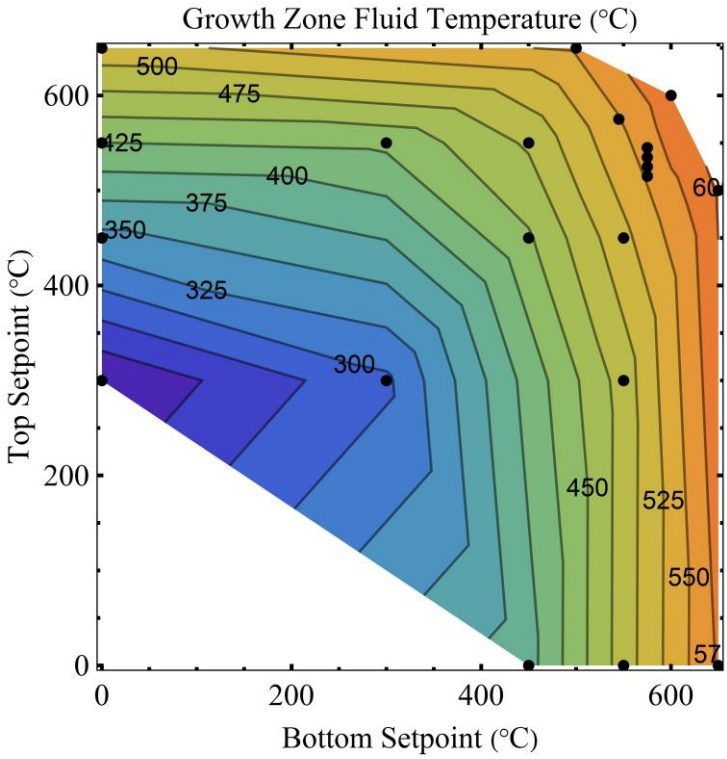

Figure 3-3. Growth zone fluid temperature contours as a function of top and bottom heater setpoint with uninsulated grand nut configuration.

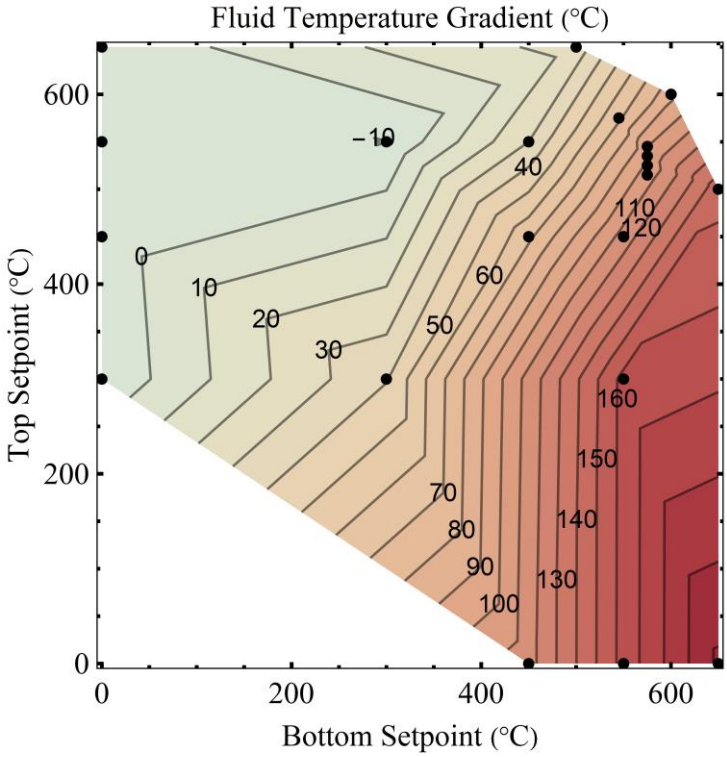

Figure 3-4. Fluid temperature gradient contours (growth – dissolution) as a function of top and bottom heater setpoint with uninsulated grand nut configuration.

It can be observed from the above figures that there is a significant deviation in external autoclave temperature and internal fluid temperature. Both the dissolution and growth zone fluid temperatures are functions of top and bottom heater setpoint, but it is clear that the largest temperature deviation exists between the external autoclave temperature in the top heater zone and the dissolution zone fluid temperature. This is likely due to the heat lost through the unheated/uninsulated grand nut. This heat loss mechanism limits achievable global temperatures, and also limits the system from achieving large negative temperature gradients (hotter dissolution zone than growth zone), which may be desirable for etch-back steps before seeded crystal growth occurs [79]. A second temperature series was conducted by directly heating the grand nut to the same temperature as the top heater zone to examine the effects of removing this heat loss mechanism. The dissolution zone fluid temperature, growth zone fluid temperature, and temperature gradient for a heated grand nut configuration are shown in Figure 3-5, Figure 3-6, and Figure 3-7, respectively.

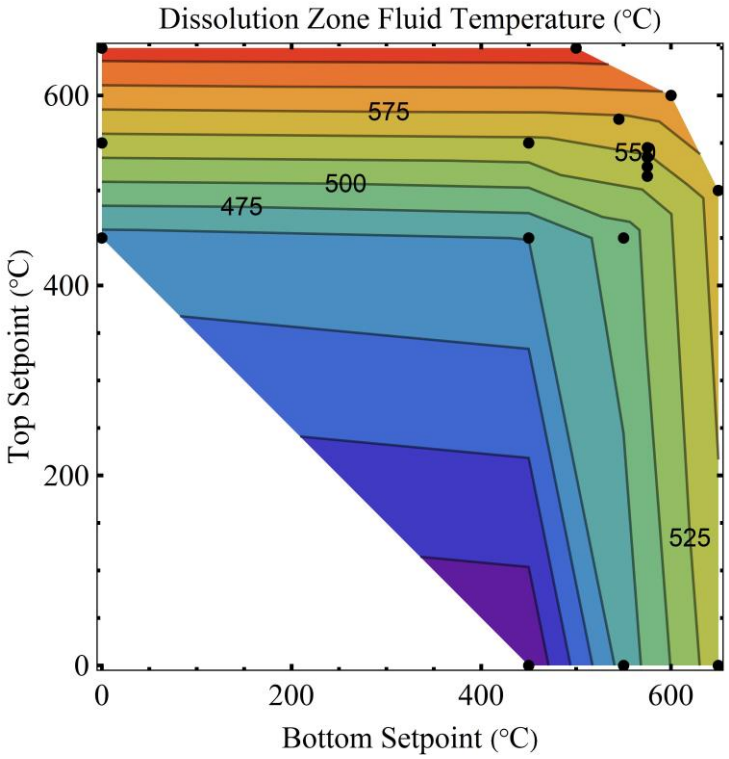

Figure 3-5. Dissolution zone fluid temperature contours as a function of top and bottom heater setpoint with grand nut heated to the top heater setpoint.

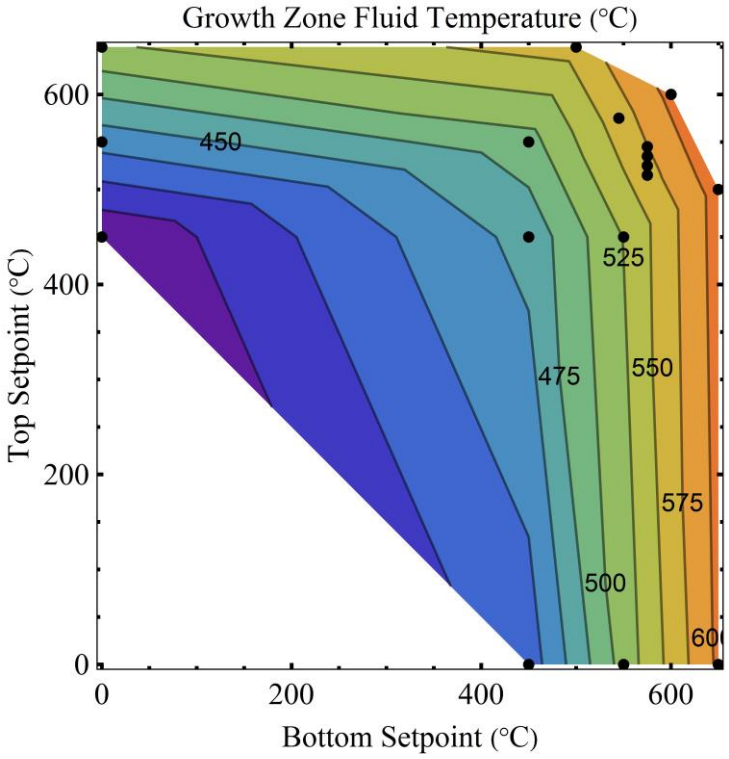

Figure 3-6. Growth zone fluid temperature contours as a function of top and bottom heater setpoint with grand nut heated to the top heater setpoint.

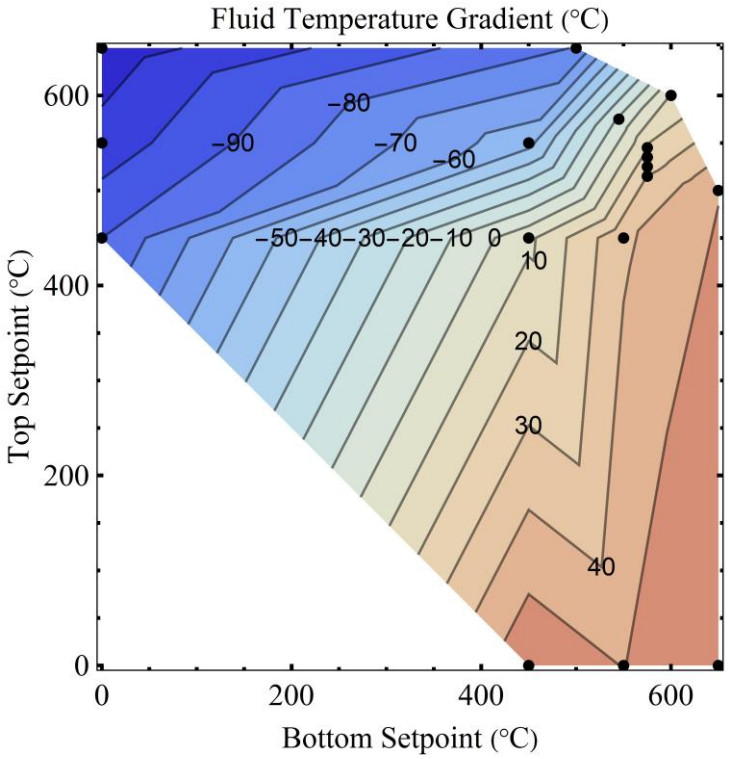

Figure 3-7. Fluid temperature gradient contours (growth – dissolution) as a function of top and bottom heater setpoint with grand nut heated to the top heater setpoint.

The aforementioned temperature series (or "calibration" runs) were used to select top and bottom heater setpoints to achieve the desired fluid temperature conditions for the 12 growth runs in this study. Nevertheless, thermocouple probes were still included in each growth run, as some deviation from the calibration runs was expected. The loading sequence for each growth run was carried out as follows. Epi-ready, double-side polished HVPE GaN seed crystals, of the aforementioned crystallographic orientations, were procured from Mitsubishi Chemical Co. and Suzhou Nanowin Science and Technology Co., Ltd (Nanowin). The crystal quality of the {0001} orientation seeds was analyzed using a high resolution X-ray diffractometer (Philips X'Pert Panalytical MRD Pro) in double-axis geometry by collecting four ω-rocking curve (ω-XRC) scans on each face of the seed: the Ga-face, or (0001) orientation, and the N-face, or (000$\bar{1}$) orientation. The beam spot for this analysis was

approximately 10 mm x 1 mm. The four ω-XRC scans included two symmetric reflections (satisfying the 002 reflection condition) at orthogonal incident beam angles ($s_0 \parallel [11\bar{2}0]$, and $s_0 \parallel [10\bar{1}0]$), in addition to two asymmetric reflections (satisfying the 112 and 102 reflection conditions), with the incident beam projected along $[10\bar{1}0]$ and $[11\bar{2}0]$, respectively. The figure of merit for each ω-XRC scan was the full-width at half maximum (FWHM) of the reflection, which was compared to the value of the ammonothermally-grown resultant crystal after each growth run.

After ω-XRC analysis, each seed was cut down to the desired size using a diamond scribe, with each resultant seed crystal section drilled using a 0.75 mm diameter diamond-coated drill bit in order to be hung on the furniture assembly. The seeds were then solvent cleaned in subsequent baths of acetone, isopropanol, and de-ionized water. The thickness and mass of each seed was then catalogued using a micrometer (Mitutoyo No. 293-765-30, accuracy: ± 1 μm) and high precision balance (Mettler Toledo AB135-S/FACT, precision: ± 0.01 mg), respectively. The same high precision balance was used to measure the mass of the polycrystalline GaN (poly GaN) feedstock, which was sourced from MCC as a parasitic byproduct during their production of HVPE GaN boules. The poly GaN was also solvent cleaned prior to use in each growth run. The average grain size of the poly GaN was approximated to be 2 mm in diameter.

As previously mentioned, the GaN seed crystals were hung on the furniture assembly using 80-20 Ni-Cr wire in the growth zone of the autoclave, and the poly GaN feedstock was placed in an 80-20 Ni-Cr mesh basket in the dissolution zone of the autoclave. After positioning the thermocouple probes in immediate proximity to both the poly GaN feedstock and the seed crystals, the autoclave assembly was moved to a nitrogen-filled glovebox (ambient containing

≤ 1 ppm O_2 and H_2O), where the Na (sourced from Alfa Aesar, 99.95% metals basis purity) was prepared, weighed, and added to the autoclave according to procedures described in [79]. The amount of Na added to the autoclave was selected to form a 20:1 NH_3:Na molar fill ratio to be consistent with Ref. [95]. After the Na was added, the autoclave assembly was weighed, the free volume was measured, and the autoclave assembly was filled with high-purity NH_3 (Denko K.K., 99.99995% purity and further purified to ≤ 1 ppb H_2O, O_2, and CO_2 using a Japan Pionics purifier and a SAES MicroTorr point-of-use purifier) according to procedures described in [95]. It should be noted that the NH_3 fill density was adjusted to target a total system peak pressure of 200 MPa for each experiment. After the autoclave assembly was filled with NH_3 and allowed to warm back up to room temperature, it was placed in a resistive heater stack (shown in Figure 3-1) with either a heated or open grand nut depending on the target internal fluid temperatures. The top and bottom heaters were then gradually ramped up to their target temperature setpoints at a maximum rate of 2 °C/minute, as measured by Type K thermocouples (accuracy: ± 0.4% of reading) placed in contact with the external autoclave wall. These temperature setpoints were maintained for growth runs of roughly one week, during which the total system pressure was monitored with a pressure transducer (Honeywell model with ± 3 MPa accuracy, or Omegadyne model with ± 0.3 MPa accuracy) and the internal fluid temperatures in the dissolution and growth zones were monitored using the aforementioned Inconel-sheathed Type K thermocouple probes (accuracy: ± 0.4% of reading). It should be noted that the internal thermocouple probes did fail on occasion. The typical failure mode was a short across the wires before the junction, which resulted from a crushed Inconel-sheath (due to the high system pressure, and pinch points in the furniture assembly), and could be recognized by large, non-physical temperature fluctuations. Rarely did the crushed sheath

result in appreciable NH_3 loss, as these leaks tended to self-seal. If the thermocouples failed before the fluid temperature reached equilibrium, the reported fluid temperature was extrapolated from the ramp step before failure, and the external thermocouple temperature-time trace. The error bars were extended in measurements resulting from failed thermocouples, where appropriate.

After the week-long growth run, the autoclave assembly was allowed to cool down to room temperature. This assembly was then vented, opened, neutralized, and cleaned according to procedures described in Ref. [95]. The post-run mass of the poly GaN feedstock and ammonothermally-grown crystals was recorded using the same precision balance as before the run. Due to surface roughness of the as-grown crystals (particularly on the Ga-face of the {0001} orientation crystals), a less-accurate drop micrometer with a finer probe tip (Mitutoyo No. 543-252, accuracy: ± 3 μm) was used to record the post-run thickness of the crystals by averaging over a large number of measurements. The {0001} orientation crystals were then measured in the same fashion as the seeds, using ω-XRC analysis on both the Ga-face and N-face. After ω-XRC analysis, impurity incorporation in the ammonothermally-grown {0001} crystals was quantified by secondary ion mass spectrometry (SIMS) using a high depth resolution tool (Cameca IMS 7f Auto SIMS) equipped with high density cesium and oxygen primary ion beam sources for atmospheric and metallic impurity identification, respectively. To avoid measuring surface contamination, the Ga-face and N-face of each of these crystals was ablated until bulk level impurity concentrations were measured, as identified by an asymptotic concentration-depth profile.

3.3 Results and Discussion

The key experimental parameters for each of the 12 growth runs in this study are presented in Table 3-1.

Table 3-1. Key experimental parameters for the growth runs in the "Effect of Fluid Temperatures" study.

Heated Grand Nut? (Y/N)	**Top Heater Setpoint (°C)**	**Bottom Heater Setpoint (°C)**	**Dissolution Zone Fluid Temp. (°C)**	**Growth Zone Fluid Temp. (°C)**	**Peak Pressure (MPa)**	**Soak Time (hr)**	**# {0001} seeds**	**# {10$\bar{1}$0} seeds**
N	450	525	410	486	200	168	1	1
N	590	525	479	529	180	151	1	1
N	250	600	341	534	218	168	3	1
N	515	560	443	545	228	151	1	1
N	545	575	466	551	226	168	1	1
N	545	575	454	558	225	168	3	1
N	650	500	532	565	209	168	1	1
N	545	575	460	568	211	168	1	1
N	440	625	401	571	239	168	1	1
N	460	650	419	591	259	168	1	1
N	590	600	497	600	261	168	2	2
Y	550	610	554	606	220	168	1	1

The reason for the considerable spread in pressures across all experiments is likely the result of under-valuing the contribution of the growth zone fluid temperature on the average fluid temperature in the entire autoclave. To clarify this point, a "global" average temperature for the fluid in the autoclave was estimated by equally-weighting the target dissolution and growth zone fluid temperatures (which had roughly the same internal volumes). This global

average temperature was then used in accordance with the NIST-extrapolated NH_3 equation of state to select a target NH_3 fill density to achieve a total system peak pressure of 200 MPa. It would appear that the measured total system peak pressure scaled somewhat with growth zone fluid temperature, implying that the growth zone should have had a greater weight in determining the global average fluid temperature. Additional factors contributing to pressure deviation could include errors in free volume measurement of the autoclave assembly, errors in obtaining the proper NH_3 fill, and not obtaining the target internal fluid temperatures during the experiment. As can be seen in Table 3-1, there was some deviation in dissolution and growth zone fluid temperatures even when the same top and bottom heater setpoints were used in conjunction with the same furniture assembly. This shows that internal fluid temperature control is very difficult, and further motivates the use of internal thermocouple probes as an additional feedback loop for fine-tuning the growth process. Furthermore, as indicated in the calibration runs and in Table 3-1, on occasion an inverse external temperature gradient (hotter top heater setpoint than bottom heater setpoint) was used to achieve small retrograde fluid temperature gradients (hotter growth zone fluid temperature than dissolution zone fluid temperature). This is of note, because prior to thermocouple probe access of the fluid temperatures, these setpoints were intended to be used for etch-back processes. What follows in the subsequent sections is an analysis of the effect of internal fluid temperatures on crystal growth kinetics, crystal quality, and impurity incorporation for the 12 growth runs utilized in this study.

3.3.1 Crystal Growth Kinetics

Ammonothermal crystal growth, and other solution crystal growth techniques, can be thought of as a sequence of chemical processes which fall into three general categories: dissolution, dissolved mass transport, and crystallization. Crystal growth kinetics are limited by the slowest of these processes, therefore it is important to understand the limitations of the ammonothermal system so as to improve metrics such as growth rate. As elucidated in this section, knowledge of the fluid temperatures is key in understanding each of these processes. Figure 3-8 and Figure 3-9 display the cumulative growth rates (taking into account growth on each side of the seed, determined by thickness measurements) of the {0001} and {10$\bar{1}$0} orientation crystals, respectively. The growth rates are represented by density plots with the relevant magnitude indicated by color on the adjacent bar legend, and the growth zone and dissolution zone fluid temperatures shown on the abscissa and ordinate axes, respectively. It is helpful to visualize the results in this way, as it gives the reader some sense of the dependence of the quantity of interest on both independently-controlled fluid zone temperatures. As previously indicated in the calibration run contour plots, the black points represent experimentally-measured quantities, with the parameter space between them determined through linear interpolation.

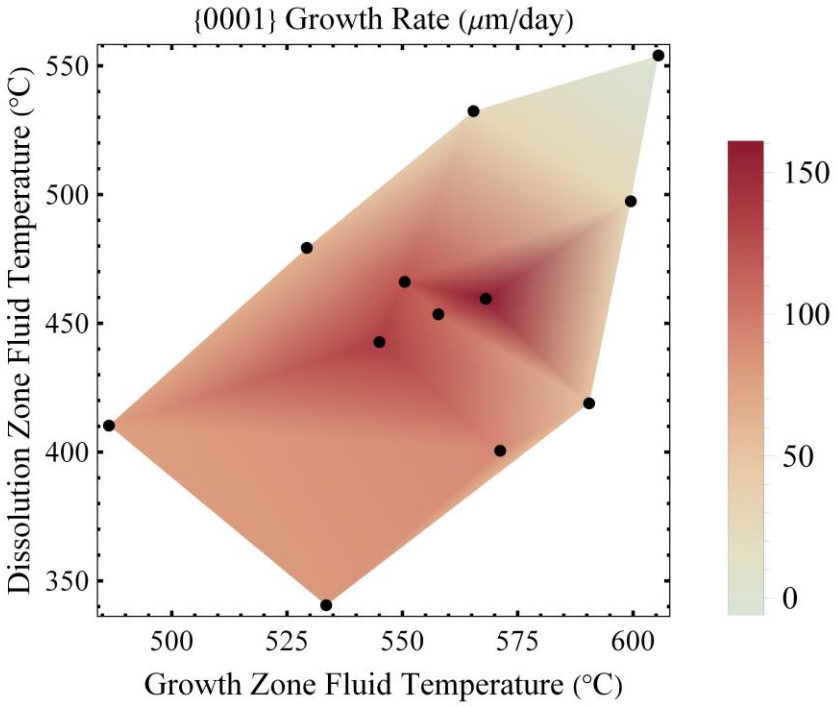

Figure 3-8. {0001} growth rate density plot as a function of dissolution and growth zone fluid temperatures.

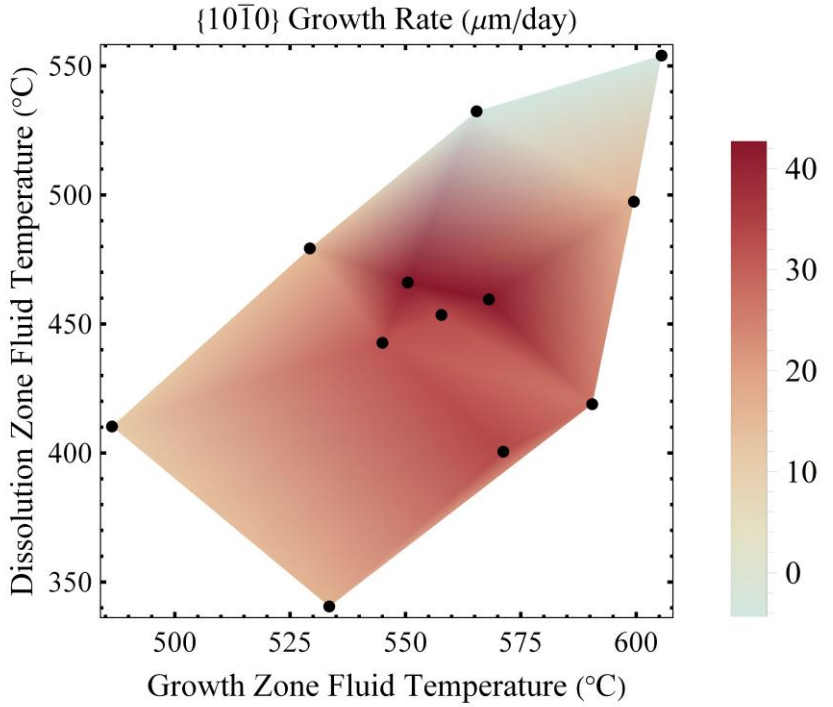

Figure 3-9. {10$\bar{1}$0} growth rate density plot as a function of dissolution and growth zone fluid temperatures.

Three important observations can be made from Figure 3-8 and Figure 3-9. First, there is a large difference in growth rate magnitude between {0001} and $\{10\bar{1}0\}$ orientation crystals, with the {0001} crystals having a far greater peak growth rate. This is a common observation within the basic ammonothermal literature [61][72][73]. Second, there is a peak growth rate observed for each crystallographic orientation within the parameter space explored (i.e. growth rate does not increase or decrease indefinitely with either dissolution or growth zone fluid temperature), implying growth rate optimization may be able to be achieved within this parameter space. Third, as anticipated from previous reports, growth appears to occur under retrograde conditions, except for low retrograde temperature gradients where etching is actually observed. This was realized for the {0001} and $\{10\bar{1}0\}$ crystals at a growth zone fluid temperature of 606°C and a fluid temperature gradient of 52°C, and for the $\{10\bar{1}0\}$ crystal at a growth zone fluid temperature of 565°C and a fluid temperature gradient of 33°C. Etching cannot be explained by the temperature coefficient of solubility at these conditions, as growth was realized for larger retrograde temperature gradients at comparable growth zone temperatures, assuming the absence of some local maximum in solubility in this regime. A likely explanation for etching at these conditions is mass transport stagnation between the dissolution and growth zones. In order to analyze the mass transport capability of the ammonothermal system, one typically starts from the continuity, momentum and thermal energy conservation equations, which are shown in Equation 3-1, Equation 3-2, and Equation 3-3, respectively (under the assumption of incompressible, Newtonian fluid flow) [100].

Equation 3-1

$$\frac{1}{\rho}\left(\frac{\partial \rho}{\partial t} + \boldsymbol{u} \cdot \nabla \rho\right) + \nabla \cdot \boldsymbol{u} = 0$$

Equation 3-2

$$\rho\left(\frac{\partial \boldsymbol{u}}{\partial t} + \boldsymbol{u}\cdot\nabla\boldsymbol{u}\right) = \Delta\rho\boldsymbol{g} - \nabla \mathrm{p} + \mu\nabla^2\boldsymbol{u} + \nabla\mu\cdot(\nabla\boldsymbol{u} + \nabla\boldsymbol{u}^{\boldsymbol{T}})$$

Equation 3-3

$$\rho C_p\left(\frac{\partial T}{\partial t} + \boldsymbol{u}\cdot\nabla T\right) = \nabla\cdot(k\nabla T)$$

The symbols in the above equations refer to the following quantities: density (ρ), time (t), fluid parcel velocity (**u**, with transpose, $\mathbf{u}^{\mathbf{T}}$), gravitational acceleration (**g**), pressure (p), dynamic viscosity (μ), heat capacity at constant pressure (C_p), temperature (T), and thermal conductivity (k). Equation 3-2 is also called the Navier-Stokes equation. Most fluid dynamic treatments of ammonothermal growth utilize the Boussinesq approximation when solving the Navier-Stokes equation, which is useful for describing systems which utilize fluid temperature gradients to support buoyancy-driven transport [100][101][102][103]. This approximation neglects variations in fluid properties with temperature, with the exception of density in the body force term of Equation 3-2 (Δρ**g**). Typically a linear dependence on temperature is assumed for density (with respect to some reference density, ρ_0, at temperature T_0), according to Equation 3-4, resulting in a simplified form of the Navier-Stokes relation, given in Equation 3-5 [100].

Equation 3-4

$$\frac{\rho_0}{\rho} = 1 + \beta(T - T_0)$$

Equation 3-5

$$\rho_0\left(\frac{\partial \boldsymbol{u}}{\partial t} + \boldsymbol{u}\cdot\nabla\boldsymbol{u}\right) = -\rho_0\beta(T - T_0)\boldsymbol{g} - \nabla \mathrm{p} + \mu_0\nabla^2\boldsymbol{u}$$

In the limit of axisymmetric heating (in this case, a temperature gradient existing only along the autoclave axis, i.e. parallel to gravitational acceleration), Equation 3-5 indicates the possibility of fluid stagnation if the buoyancy force counteracts the hydrostatic pressure contribution. This is the critical condition which when exceeded by an increasing temperature-driven density gradient, results in heat transport transitioning from pure conduction to (at least partially) convection. Above this point, nonzero fluid velocity can result in convective mass transport [100]. This simplified case is known as the Rayleigh-Benard problem, and excludes axial autoclave wall heating, which is clearly present during ammonothermal crystal growth. The analogy to this simplified problem is valid however, where a critical density gradient must be present between the dissolution and growth zones to drive convective mass transfer across the baffle plates. Below this critical density gradient, it is anticipated that fluid flow stagnates, and both source poly GaN and GaN seed crystals are dissolved in their respective zones to satisfy the solubility limit at each respective temperature. To quantify the critical density difference that must be present for convective mass transport to occur, Figure 3-10 illustrates the NIST-extrapolated fluid density differences in each of the twelve growth experiments (taking into account the temperatures in each zone, and total system peak pressures).

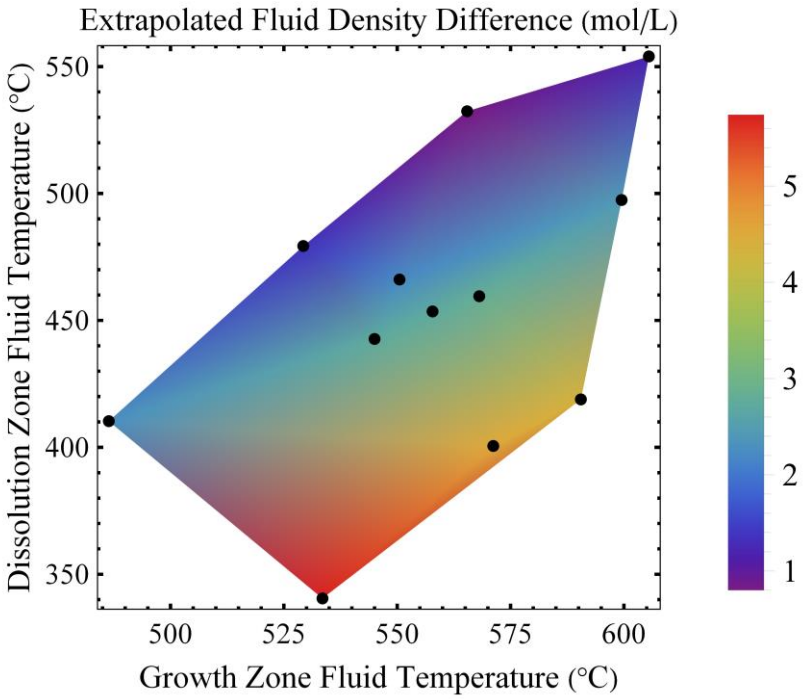

Figure 3-10. NIST-extrapolated fluid density gradient plot as a function of dissolution and growth zone fluid temperatures.

As can be seen in Figure 3-10, NH_3 density gradients exceeding 1.2 mol/L tended to result in crystal growth, while density gradients below this value resulted in etching of at least one of the seeds present. Due to the large peak pressure variation in these experiments (181 - 263 MPa), and the inaccurate accounting for NH_3 decomposition through extrapolation of the NIST fluid density data, the linear interpolation between experimental measurements can only be viewed as qualitatively accurate. However, it is clearly apparent when comparing Figure 3-8 and Figure 3-9 with Figure 3-10 that the greatest growth rates do not coincide with the greatest fluid density gradient. This implies that convective mass transport does not completely limit crystal growth kinetics in the explored fluid temperature range, excluding the aforementioned conditions where etching of seed crystals occurred. To further understand the limitations crystal growth kinetics, one must independently analyze dissolution and crystallization processes as a function of dissolution and growth zone fluid temperatures.

3.3.1.1 *Polycrystalline GaN Source Loss Flux*

The poly GaN source material had roughly the same particle size distribution for each experiment. However, defining/analyzing a poly GaN source loss flux, as opposed to a simple source mass loss, enables one to account for variations in growth run time (see Table 3-1) and initial source mass. To calculate the source loss flux, the poly GaN mass change and growth run time were directly measured, while the total surface area was approximated by treating the poly GaN charge as a population of 2 mm diameter spheres (with standard deviation estimated at 0.4 mm). The source loss flux density plot is shown in Figure 3-11, excluding the runs where seed etching was observed (per discussion in 3.3.1).

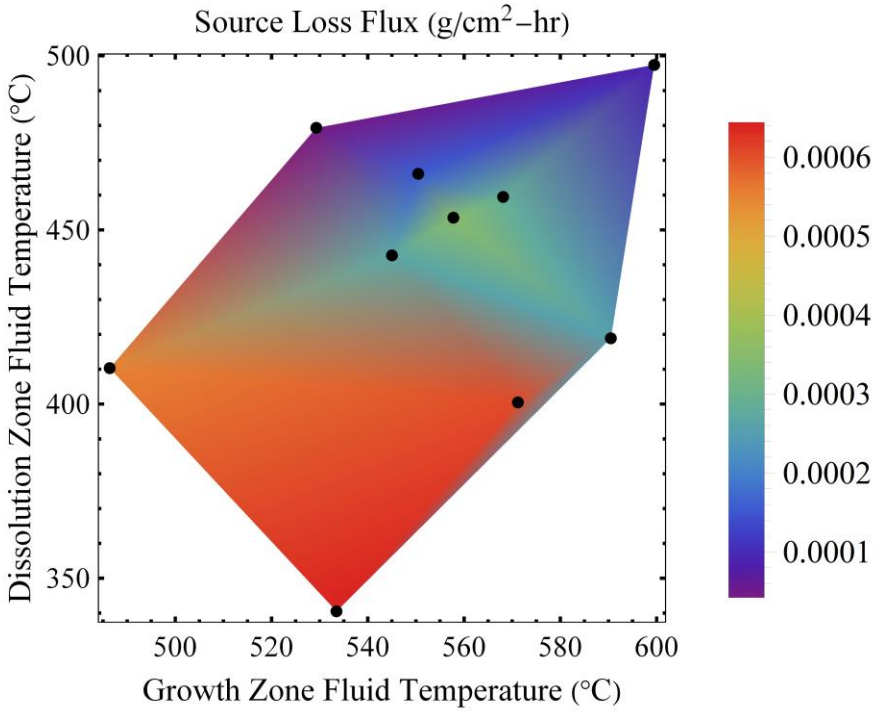

Figure 3-11. Source loss flux density plot as a function of dissolution and growth zone fluid temperatures, showing strong correlation with dissolution zone flud temperature.

It is apparent from Figure 3-11 that the poly GaN source loss flux is more closely correlated with dissolution zone fluid temperature than growth zone fluid temperature (with Pearson correlation coefficients of -0.89 and -0.36, respectively). Source loss flux is plotted

directly against dissolution zone fluid temperature in Figure 3-12 to give the reader a better understanding of the expected errors associated with this analysis. The aforementioned best-fit line is included in the plot. The noise in the data is anticipated to come from the dependence of source loss flux on the extrapolated fluid density difference (with a Pearson correlation coefficient of 0.70), which is clearly a function of both dissolution and growth zone fluid temperatures, as shown in Figure 3-10. The behavior of source loss flux is consistent with both a retrograde solubility curve, and mass transport which is at least partially limited by convection. However, poly GaN mass loss includes contributions from dissolution alone (in both the supercritical fluid and in the Na-rich phase), parasitic nucleation/growth on autoclave components, and seeded growth. Therefore, the correlation between seeded crystal growth and source loss must be further explored.

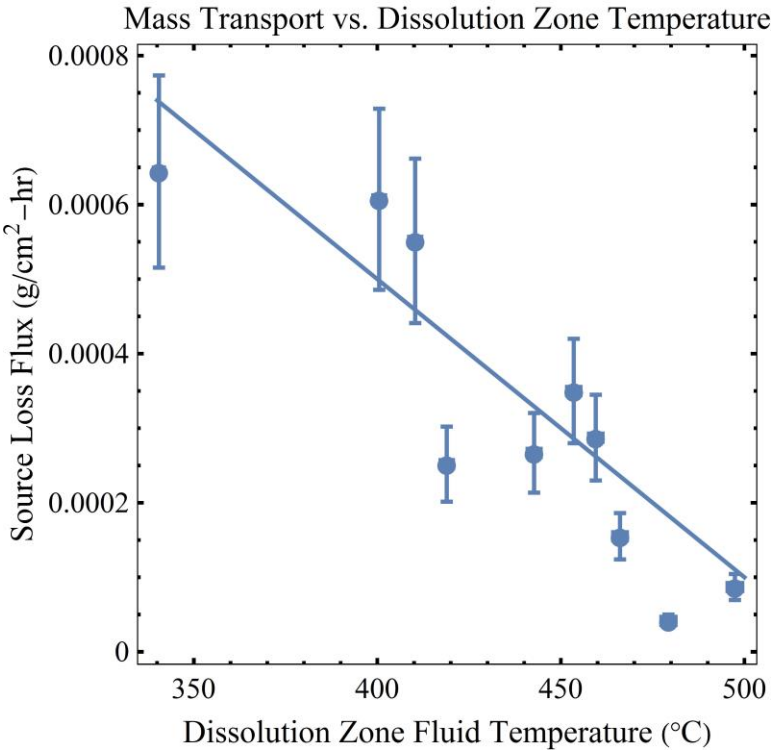

Figure 3-12. Source loss flux as a function of dissolution zone fluid temperature, with error bars and best fit line included (R^2 = 0.79).

3.3.1.2 *Seeded Growth Flux*

The standard metric used in the literature to report crystal growth kinetics is growth rate. As explained in the Experimental Methods section, this quantity was measured by micrometer, but significant error was introduced due to the surface roughness of the as-grown crystals. Furthermore, it is fairly common to observe different growth rates on seed crystals of the same orientation depending on their position in the autoclave. This could be caused by many factors, but temperature stabilization in the growth zone is thought to be the most likely determinant. In order to compare growth runs which contained different numbers of seed crystals of {0001} and $\{10\bar{1}0\}$ orientations (which can be viewed in Table 3-1) with a less "noisy" metric, a seed mass flux analysis was employed. Similar to source loss flux, the starting mass and thickness measurement of each seed allows one to very accurately estimate its surface area (neglecting the small surface area of edges). This surface area of each seed can be summed for the entire batch, which when coupled with mass change and experiment time, yields a cumulative seed mass flux for each experiment. This quantity is plotted in Figure 3-13, again excluding experiments where seed etching occurred.

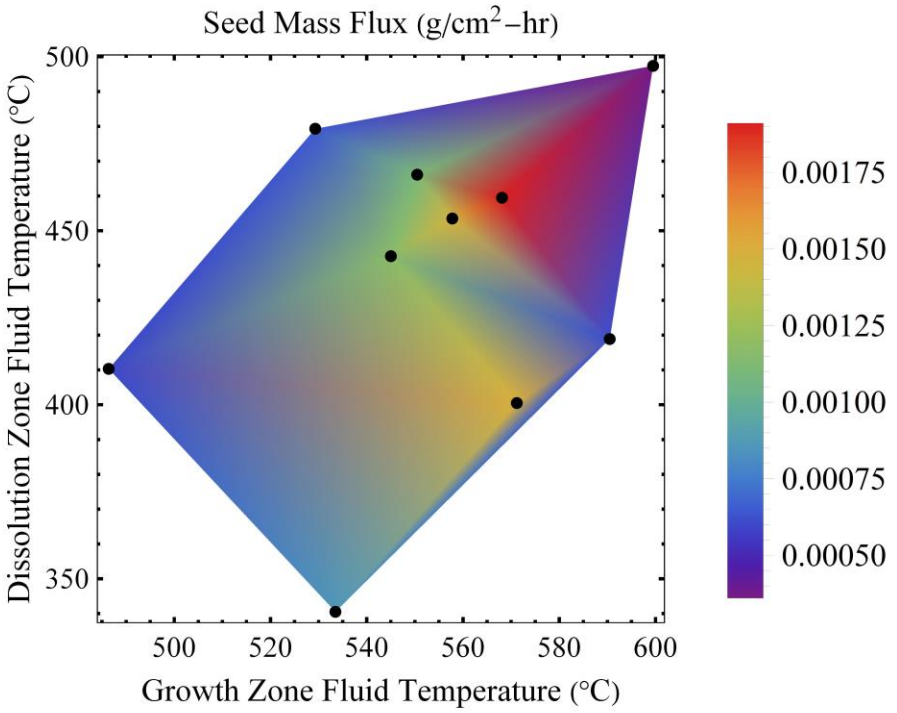

Figure 3-13. Seed mass flux density plot as a function of dissolution and growth zone fluid temperatures, showing similar qualitative behavior as the analogous growth rate density plots.

As one might expect, Figure 3-13 is qualitatively similar to Figure 3-8 and Figure 3-9, as seed mass flux is analogous to growth rate, but averaged over each orientation and includes GaN added through faceting. Once again, enhanced seeded growth kinetics are realized within a specific dissolution and growth zone fluid temperature range, with no obvious dependence on one of these temperatures in particular. However, given that source loss flux is almost exclusively dependent on dissolution zone fluid temperature and extrapolated fluid density difference, and that both measured fluxes do not covary, one plausible explanation is that seed mass flux is surface integration limited.

Growth from solution in the surface integration limit is characterized by rapid dissolved mass transport. In this limit there is effectively no boundary layer thickness in the solution around the crystal, pinning the concentration of the solute at the seed-solution interface to the solubility limit in the dissolution zone [96]. There have been many derivations of rate equations

for surface integration limited growth, the boundary conditions of which typically depend on the growth mode (spiral, step-flow, etc.). One such rate equation, elucidated by Doherty et al. from the work of Vekilov and De Yoreo for spiral growth (typically at low supersaturation) is shown in Equation 3-6 [96].

Equation 3-6

$$G_{SI} = \frac{hV_M\beta(C_\infty - C_{eq})}{y}$$

The symbols in Equation 3-6 refer to the following quantities: surface integration limited perpendicular growth rate of a crystallographic face (G_{SI}), step height (h), molecular volume (V_M), step kinetic coefficient (β), distance between steps (y), concentration of the bulk solution, which in this case is the solubility in the dissolution zone (C_∞), and equilibrium concentration, which in this case is the solubility in the growth zone (C_{eq}). The step kinetic coefficient is defined in Equation 3-7 [96].

Equation 3-7

$$\beta = a_p\rho_k\overline{\nu}\exp\left(\frac{-\Delta U}{RT}\right)$$

The symbols in Equation 3-7 refer to the following quantities: step propagation distance through addition of a row of molecules (a_p), kink site density (ρ_k), frequency factor ($\overline{\nu}$), incorporation energy barrier (ΔU), the ideal gas constant (R), and growth zone temperature (T). It is clear that Equation 3-7 (and therefore Equation 3-6) has an Arrhenius dependence on growth zone fluid temperature, as do most rate equations derived for surface integration limited growth [104]. Therefore, the natural log of seed mass flux is plotted against inverse growth zone fluid temperature in Figure 3-14 to ascertain whether a characteristic incorporation energy barrier is observed.

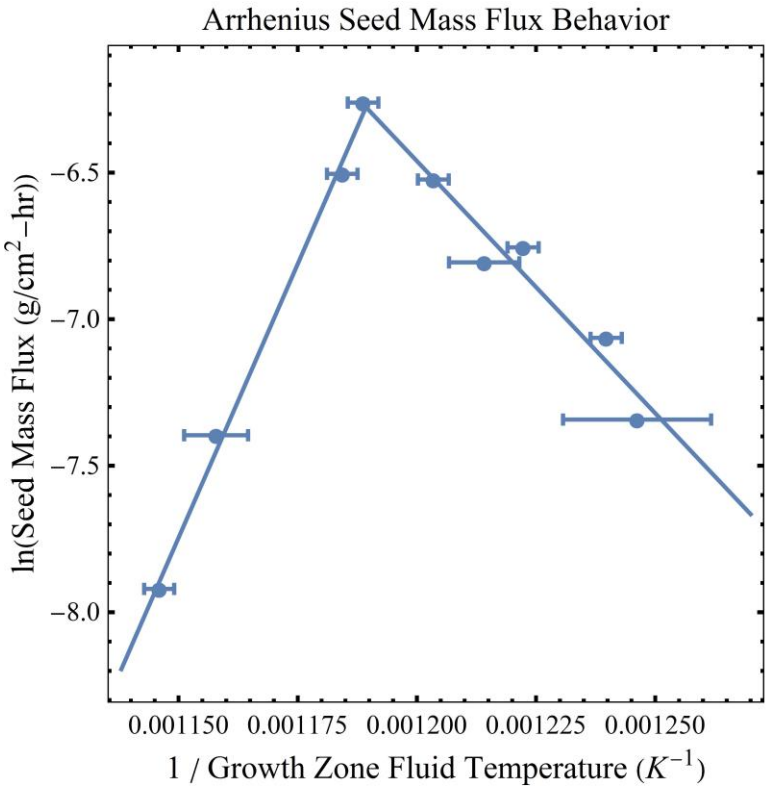

Figure 3-14. Arrhenius behavior of seed mass flux as a function of inverse growth zone fluid temperature, with error bars and best fit lines included for the seemingly endothermic region (from 529 – 568°C, with R^2 = 0.956) and exothermic region (from 568 – 600°C, with R^2 = 0.996).

As can be seen in Figure 3-14, utilizing seed mass flux allows one to limit the ordinate error bar magnitude (they are included in the plot, but are generally smaller than the size of the data markers), thereby enabling a clear temperature analysis. There are two distinct regions of the Arrhenius plot, both of which display strikingly linear behavior (as indicated in the figure with best fit lines). From 529°C to 568°C there appears to be an endothermic activation energy of 143 kJ/mol (with coefficient of determination, R^2 = 0.956), and from 568°C to 600°C there appears to be an exothermic activation energy of -311 kJ/mol (with coefficient of determination, R^2 = 0.996). It should be noted that the lowest growth zone fluid temperature run, at 486°C, was excluded from Figure 3-14 as there were not enough measurements collected at comparable temperatures to ascertain a temperature dependence. The presence of

two different activation energies implies that at least two different Arrhenius processes are in competition to limit seed mass flux. A simple knowledge of the growth zone fluid temperature dependence cannot identify these processes, but candidates may include: the presence of two different intermediate species, limited adsorbed growth unit diffusion at low temperatures, limited transport of the heat of crystallization at high temperatures, and increased NH_3 decomposition with subsequent increased H_2 diffusion out of the autoclave at high temperatures [96][97]. Too many assumptions about the system must be made to quantify the effects of growth unit diffusion and heat of crystallization transport, but competing intermediate species and NH_3 decomposition/ H_2 diffusion are discussed below as they might pertain to the observed seed mass flux behavior.

The suspected intermediate species present during ammonothermal growth in NH_3-Na chemistry are sodium tetra-amidogallate ($NaGa(NH_2)_4$) and sodium penta-amidogallate ($Na_2Ga(NH_2)_5$). The anticipated reactions to form GaN from these intermediate species are shown in Equation 3-8 and Equation 3-9 for the tetra-amidogallate and the penta-amidogallate, respectively, under the assumption that the stable Na-species is $NaNH_2$. These species were identified in powders produced by isothermal ammonothermal experiments post-run, and therefore have not been detected in situ [69]. However, in comparing their prevalence with run parameters, the tetra-amidogallate species tends to dominate at high pressure (>200 MPa) and low temperature (<450°C), while the penta-amidogallate tends to dominate at low pressure and high temperature [69]. While the bonding structures of these compounds are known in their crystalline form, no information could be found in the literature on their energetics (i.e. enthalpies of formation) and behavior when solvated. An attempt was made to calculate the enthalpy of formation of each intermediate species using Born-Haber analysis, with lattice

energies estimated from a quantitative structure-property relationship (QSPR) model for inorganic species [105]. However, the resultant enthalpies of formation were both endothermic, and too large (~6.3 MJ/mol for the tetra-amidogallate, and ~7.5 MJ/mol for the penta-amidogallate) to put much faith in this analysis. Using these enthalpies of formation, the enthalpies of reaction for Equation 3-8 and Equation 3-9 are approximately -6.7 MJ/mol and -8.0 MJ/mol, respectively, which are clearly too high to be compared to the activation energies derived from Figure 3-14. It is likely that the size and partially-covalent nature of these compounds makes Born-Haber type analysis invalid, to say nothing of the validity of the QSPR model, therefore additional information about the nature of these intermediate species is required to assess their likelihood to kinetically-control GaN growth.

Equation 3-8

$$NaGa(NH_2)_{4(sol)} \rightleftharpoons NaNH_{2(sol)} + 2NH_{3(g)} + GaN_{(s)}$$

Equation 3-9

$$Na_2Ga(NH_2)_{5(sol)} \rightleftharpoons 2NaNH_{2(sol)} + 2NH_{3(g)} + GaN_{(s)}$$

As elucidated by Pimputkar and Nakamura, NH_3 decomposition is significant under the explored experimental conditions, with equilibrium concentrations on the order of 80-90% of the fill amount between 500-600°C for pure NH_3 [89]. Additionally, chemical reactions, such as the formation of $NaNH_2$, will further decrease the amount of NH_3 present. It is not clear what effect a loss of solvent might have on ammonothermal crystal growth, but a reasonable conjecture is that it would adversely affect the ability of the fluid to transport intermediate species to the seed crystal interface, thereby hindering growth. NH_3 formation is an exothermic process (with enthalpy of formation equivalent to -46 kJ/mol), therefore

increasing the temperature of the autoclave biases the NH_3 formation reaction towards the reactants (H_2 and N_2) according to La Chatelier's principle. Loss of H_2 due to diffusion out of the autoclave would additionally push the aforementioned reaction towards favoring NH_3 decomposition. H_2 diffusion through structural materials has been thoroughly explored, which enables one to assign activation energies to this process, assuming Arrhenius behavior. Unfortunately, most of these analyses were performed at low pressure for pure Ni (5-10 kPa) in the temperature regime of interest (600-900 K), but the resultant activation energies were roughly 69 kJ/mol [106]. As for the effect of alloying, no studies could be found for H_2 diffusion through Rene 41, but the activation energy for Inconel 625 at similar conditions was 60 kJ/mol [107]. This implies that H_2 diffusion may occur more readily in Ni-Cr superalloys, such as Rene 41, than in pure Ni. While the diffusive activation energies for Ni-base autoclaves do not align with those derived from Figure 3-14, it is of note that they are significantly lower than the activation energy for H_2 diffusion through Ag (which has been reported at 126 kJ/mol for 2 kbar from 923-1084 K) [108]. This might explain why the use of a Ag capsule permits enhanced growth rates in the NH_3-Na system, although other catalytic processes cannot be ruled out [79].

3.3.1.3 *Crystal Shape Evolution*

The growth rates as determined by thickness measurements are shown as a function of dissolution and growth zone fluid temperatures for {0001} and $\{10\bar{1}0\}$ orientation crystals in Figure 3-8 Figure 3-9, respectively. Based on the appearance that overall seed mass flux is surface integration limited, plane-specific growth rates must be analyzed in greater depth for a growth zone fluid temperature dependence. Of particular interest is how crystal shape evolves

with growth zone temperature. Therefore, the {0001}:{10$\bar{1}$0} growth rate ratio (including errors associated with surface roughness) is plotted against growth zone fluid temperatures in Figure 3-15 for all runs excluding those in which seed crystals were etched.

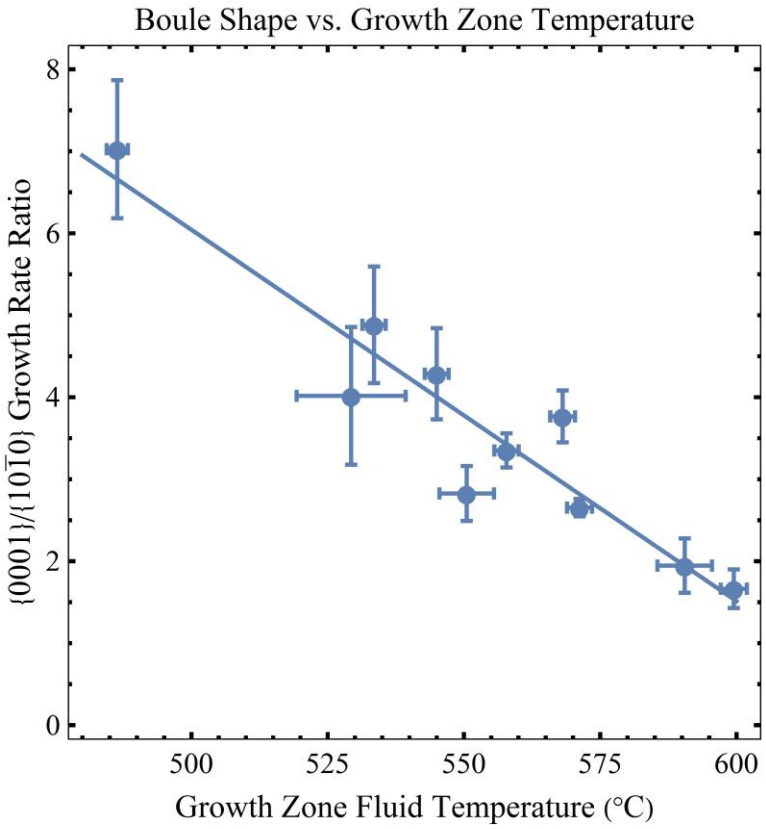

Figure 3-15. {0001}:{10$\bar{1}$0} growth rate ratio as a function of growth zone fluid temperature, with error bars and best fit line included (R^2 = 0.89).

It is clear from Figure 3-15 that the {0001}:{10$\bar{1}$0} growth rate ratio decreases with increasing growth zone fluid temperature (with best fit line indicated in the figure, R^2 = 0.89). It is unclear, however, whether the {0001}:{10$\bar{1}$0} growth rate ratio levels off at 1 (yielding an equiaxed crystal shape), or at 0 (indicating that {10$\bar{1}$0} growth rates far exceed {0001} growth rates, resulting in platelet-like crystal shape). There are many plausible explanations for this trend that fit within the kinetic arguments made in the previous section. For example, if two competing intermediate species were present with different adsorption character on polar and nonpolar planes (due to their own bond character), then it is possible that {10$\bar{1}$0} growth

is enhanced at high temperature through the growth zone temperature dominance of one intermediate over the other. Further study is of course needed to definitively state the cause of the $\{0001\}$:$\{10\bar{1}0\}$ growth rate ratio temperature dependence.

Another important aspect of bulk GaN crystal shape evolution is polar axis anisotropy. Many research groups operating with $NaNH_2$ and KNH_2 mineralizers have reported an enhancement of (0001), or Ga-face, growth rates over $(000\bar{1})$, or N-face, growth rates. Still, other research groups utilizing the same chemistry report enhanced N-face growth rates over Ga-face growth rates. This is surprising, as one would expect that similar intermediates (negatively-charged amidogallate species) should show uniform polar axis anisotropy (likely incorporating on the partially-positive Ga-face), with all other conditions being equal. With the added benefit of in situ temperature probes, the (0001):$(000\bar{1})$ growth rate ratio is plotted against growth zone fluid temperatures in Figure 3-16 for all runs excluding those in which seed crystals were etched.

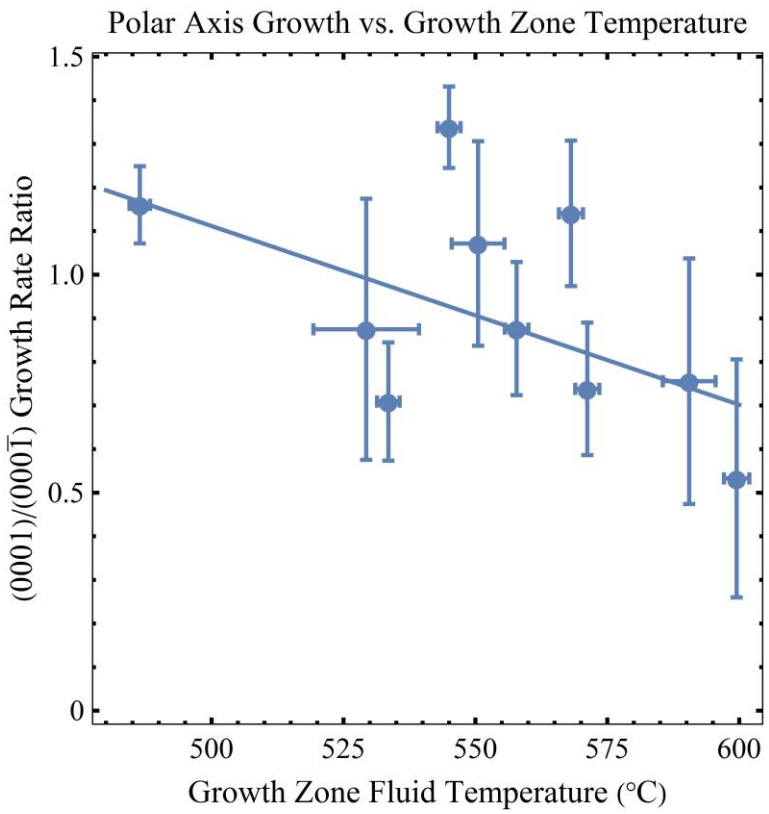

Figure 3-16. (0001):(000$\bar{1}$) growth rate ratio as a function of growth zone fluid temperature, with error bars and best fit line included (R^2 = 0.28).

Unlike the {0001}:{10$\bar{1}$0} growth rate ratio, there is not a strong correlation of the (0001):(000$\bar{1}$) growth rate ratio with growth zone fluid temperature (with best fit line indicated in Figure 3-16, R^2 = 0.28). Instead, the (0001):(000$\bar{1}$) growth rate ratio appears to be somewhat randomly distributed around an average value of ~ 1. It is possible that the resolution of the measurement technique was not sufficient to accurately determine a temperature dependence (as can be seen with the substantial ordinate error bars), or that there is no dominant polar growth anisotropy that scales with temperature. The specific Ga-face and N-face growth rates were determined by observing the perpendicular growth distance from the seed interface utilizing dark field optical microscopy. As shown in Figure 3-17, this was accomplished by collecting/measuring micrographs with a sight-line along <10$\bar{1}$0>, since the as-grown {10$\bar{1}$0} facets were smooth enough to enable the distinction of each growth-front from the seed. The

N-face material is typically darker than the Ga-face material, and semipolar faceting is typically observed on the Ga-face but not on the N-face.

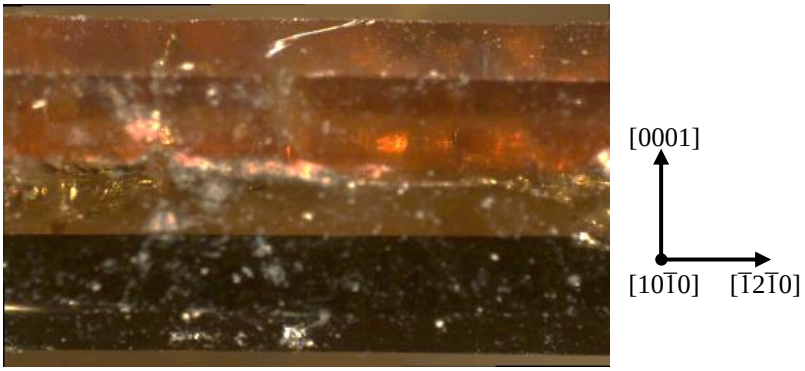

Figure 3-17. Dark field optical micrograph of a {0001} crystal looking along the <10$\bar{1}$0> direction, with perpendicular growth thicknesses of the (0001) and (000$\bar{1}$) ammonothermal material measured from the interface of the (transparent) HVPE GaN seed.

3.3.2 Crystal Quality

As previously indicated, the crystal quality of the (0001) and (000$\bar{1}$) orientation ammonothermally-grown material was assessed by ω-XRC analysis. As one might anticipate based on the discussion in 3.3.1, there was a much stronger correlation of crystal quality with growth zone fluid temperature than with dissolution zone fluid temperature. Therefore, what follows in this section are plots of the FWHM of symmetric and asymmetric reflections of the as-grown material as a function of the growth zone fluid temperature. It should be noted that there was a spread in initial seed crystal quality, which is reflected by the red-dashed lines in the following plots, providing an upper and lower seed crystal quality bound for each reflection analyzed. Although fractional change of the FWHM with respect to the seed was quantified, the absolute FWHM of the resulting crystal was much more closely-correlated with growth zone fluid temperature, which is why the data is reported in this way. Although twist and tilt of grains in crystalline films displaying some degree of mosaicity can be quantified according to the broadening of symmetric and asymmetric reflections, respectively, the goal of this work

is to display generalized trends with growth temperature. As such, quantification of specific broadening factors (twist, tilt, dislocation density, lattice plane curvature, etc.) will not be attempted.

3.3.2.1 *(0001) Orientation*

Ammonothermal growth on (0001) orientation seeds has presented a challenging problem for the field. Although the specific reasoning for generally poor crystal growth on this orientation has eluded researchers, it is commonly noted that growth proceeds in a columnar fashion, thereby leading to high mosaicity. As can be seen in Figure 3-18 - Figure 3-21, growth zone fluid temperatures in excess of ~575°C are required to match (and occasionally improve upon) the quality of the HVPE seed. This might explain why (0001) crystal quality has been slow to improve, as achieving these temperatures in the fluid pushes the limit of externally-heated Ni-base superalloy autoclave materials at high pressures.

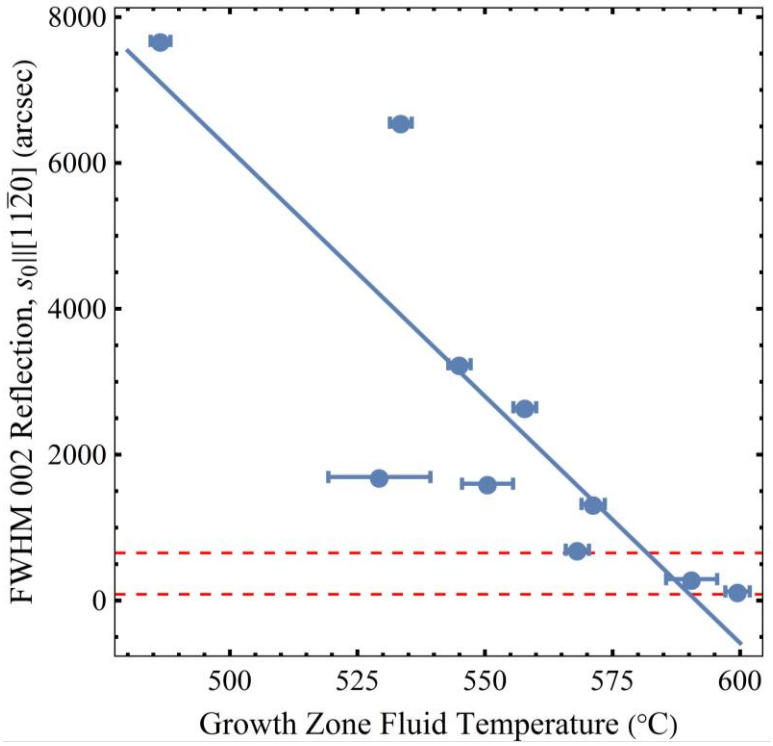

Figure 3-18. 002 peak width vs. growth temp, with error bars and best fit line included (R^2 = 0.72).

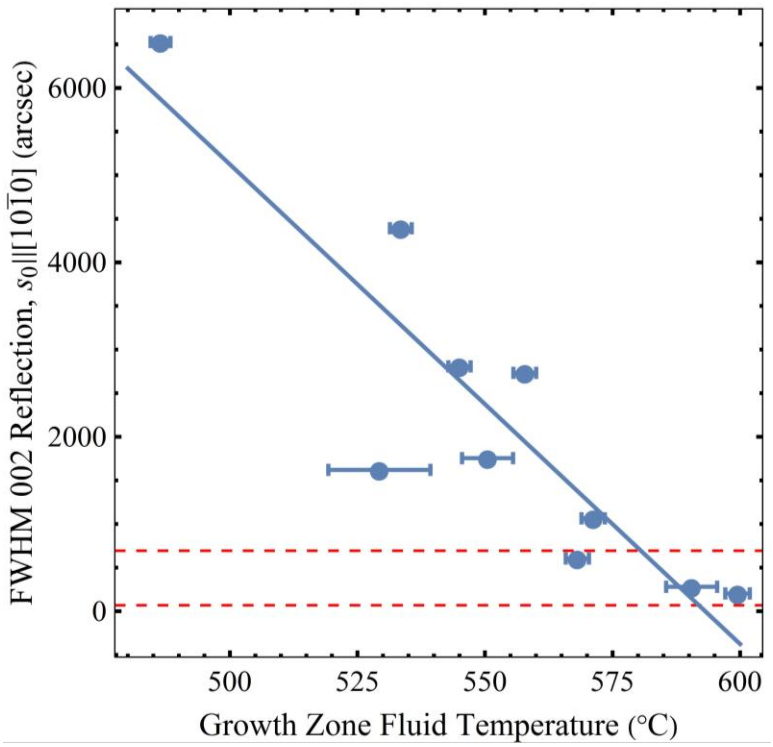

Figure 3-19. 002 peak width vs. growth temp, with error bars and best fit line included (R^2 = 0.79).

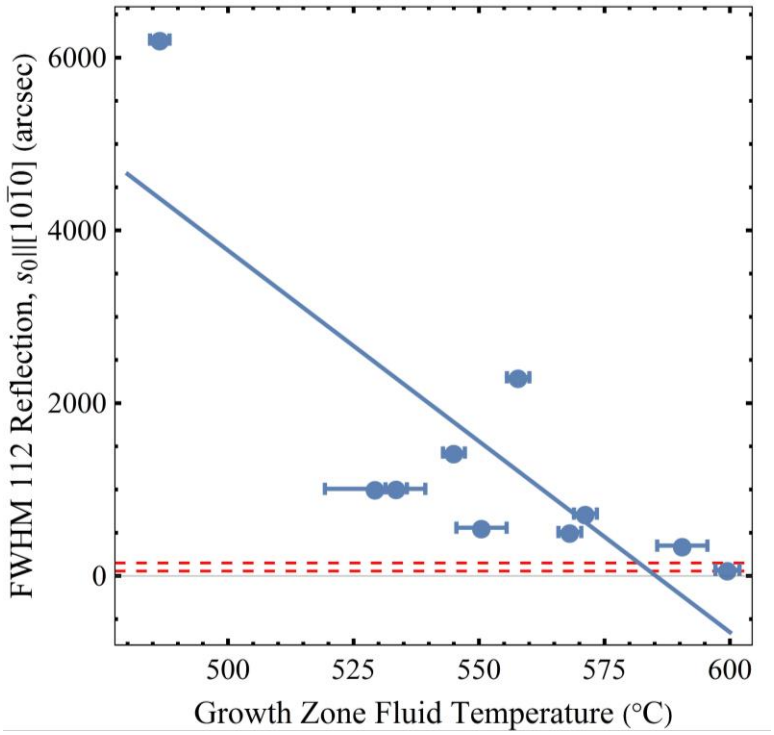

Figure 3-20. 112 peak width vs. growth temp, with error bars and best fit line included (R^2 = 0.65).

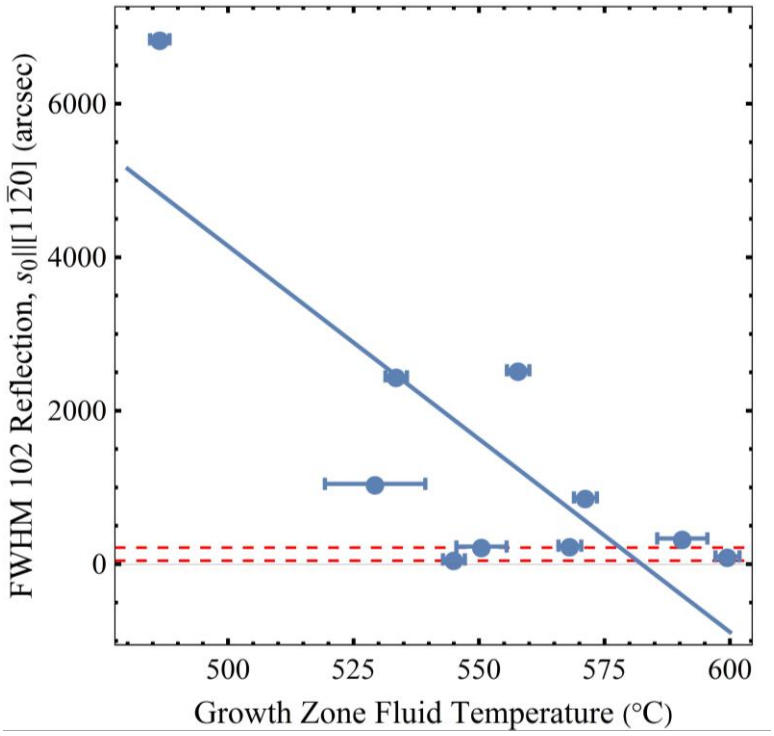

Figure 3-21. 102 peak width vs. growth temp, with error bars and best fit line included (R^2 = 0.62).

3.3.2.2 *(000$\bar{1}$) Orientation*

The crystal quality of the (000$\bar{1}$) orientation ammonothermal growth is far less correlated with growth zone fluid temperature (or any other parameter) than is the (0001) orientation growth. Once again, the specific reason for this is unknown. As is shown in Figure 3-22 - Figure 3-25, the crystal quality of the grown material typically falls within the range of seed crystal quality independently of the growth zone fluid temperature. This would suggest that the crystal quality of the seed can safely be extended into the (000$\bar{1}$) ammonothermal material, but that crystal quality improvement beyond that of the seed is not well understood with respect to growth zone fluid temperature.

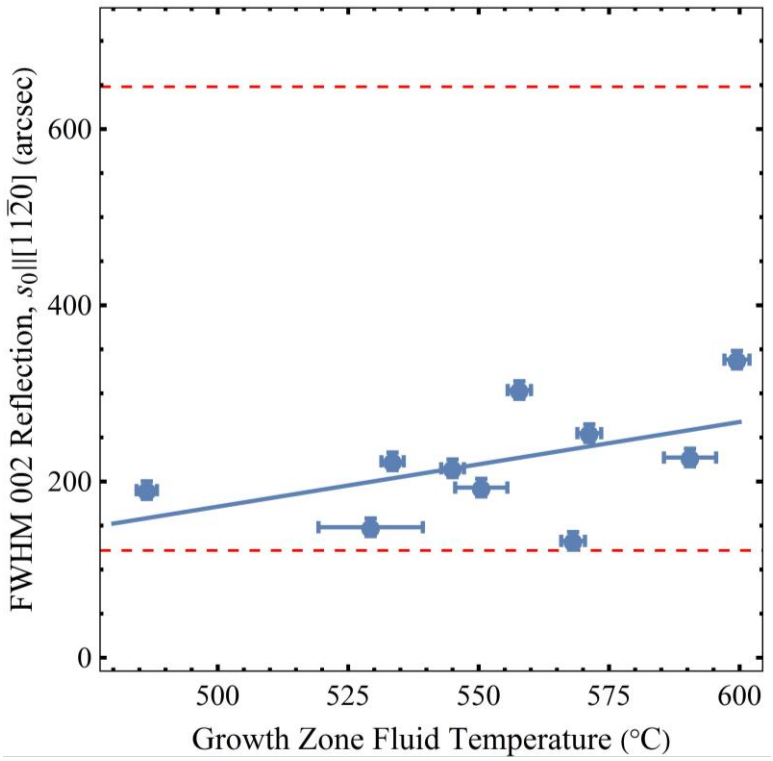

Figure 3-22. 002 peak width vs. growth temp, with error bars and best fit line included (R^2 = 0.21).

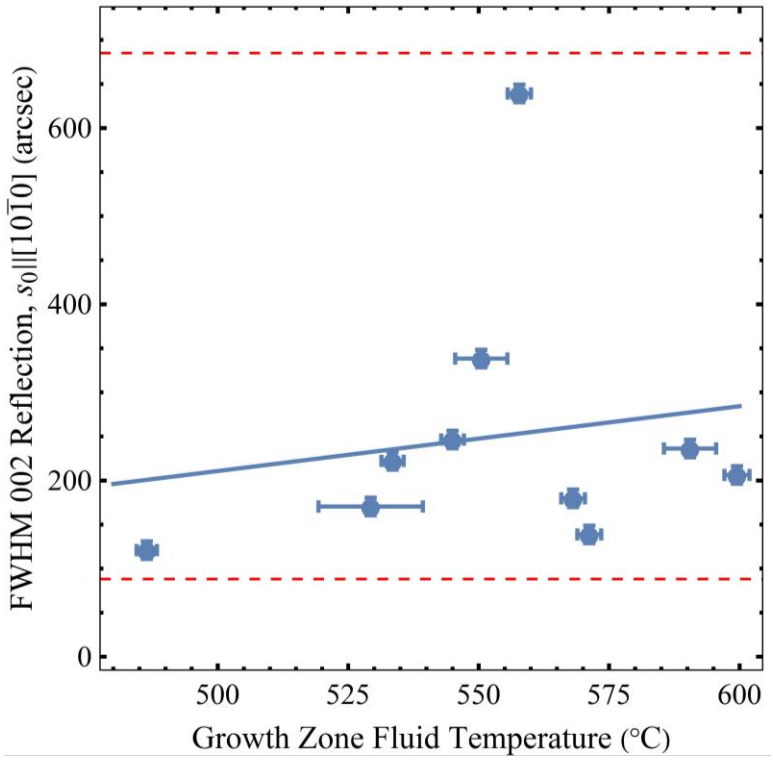

Figure 3-23. 002 peak width vs. growth temp, with error bars and best fit line included (R^2 = 0.03).

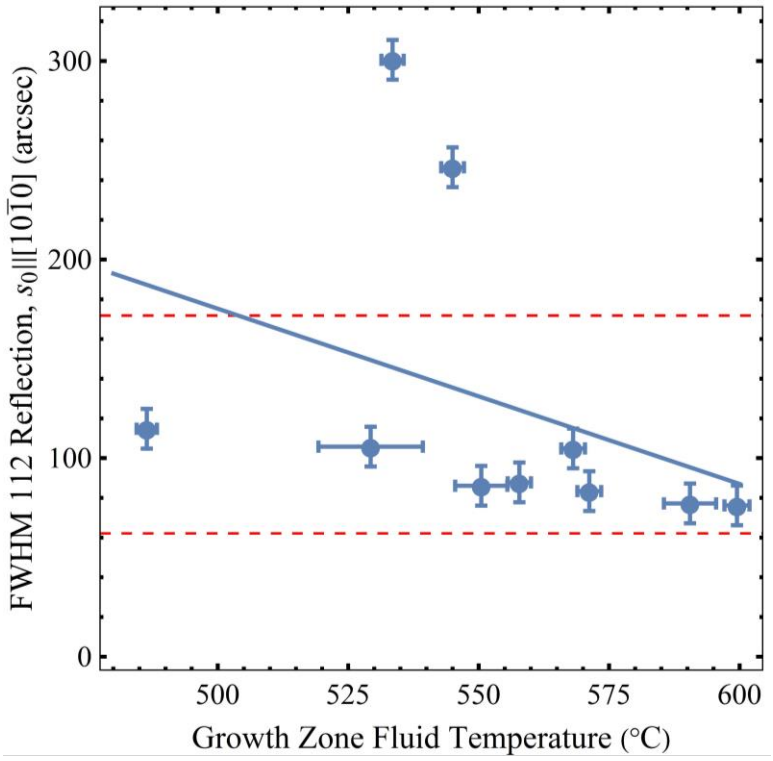

Figure 3-24. 112 peak width vs. growth temp, with error bars and best fit line included (R^2 = 0.13).

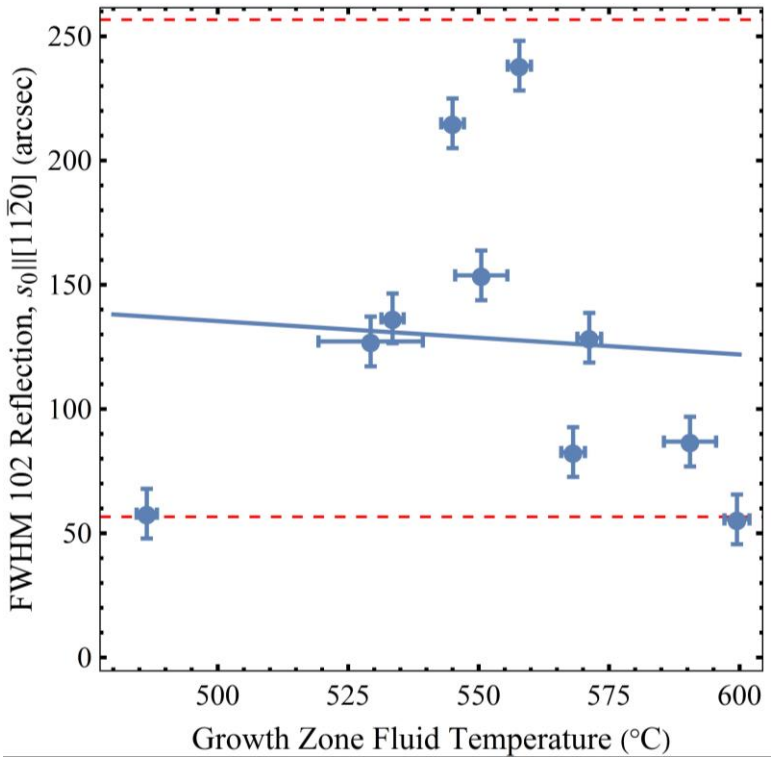

Figure 3-25. 102 peak width vs. growth temp, with error bars and best fit line included (R^2 = 0.01).

3.3.3 Impurity Incorporation

SIMS was performed on the as-grown (0001) and (000$\bar{1}$) orientation ammonothermal crystals to probe the correlation of dissolution and growth zone fluid temperatures with plane dependent impurity incorporation. As such, the resulting impurity incorporation magnitudes are represented by logarithmic density plots as a function of both internal fluid temperatures. Please note that the color scale associated with each plot should be read in base 10 units (e.g. a color represented by "18.5" on the scale bar indicates impurity incorporation of ~3.2E18 at/cm^3). The Pearson correlation coefficients for each internal fluid temperature are included in the caption of each plot. The specific metallic impurities that were quantified include: Na,

Al, Si, Fe, Mn, and Mg. The specific atmospheric impurities that were quantified include: O, C, and H.

While some of the data is noisy, some general trends exist for both orientations. Impurities which incorporated in the ammonothermal material with a greater dissolution zone fluid temperature correlation than growth zone fluid temperature correlation, as determined by Pearson coefficients, include: Al, Si, and Mn. All of these impurities increased with increasing dissolution zone fluid temperature. Impurities which incorporated in the ammonothermal material with a greater growth zone fluid temperature correlation than dissolution zone fluid temperature correlation, as determined by Pearson coefficients, include: Na, Fe, O, C, and H. All of these impurities decreased with increasing growth zone fluid temperature, with the exception of C in the $(000\bar{1})$ orientation crystals. While the incorporation magnitudes differ by orientation, these trends are consistent with Al, Si, and Mn either originating in the dissolution zone (i.e. introduced to the growth environment from the source poly GaN), or becoming activated from a greater autoclave volume (i.e. being driven off the wall in the dissolution zone, and transported to the growth zone at higher temperatures). Furthermore, the negative correlation of Na, Fe, O, and H impurity incorporation with growth zone fluid temperature is consistent with defect-site incorporation, especially given the greater magnitude of the Pearson coefficients for O and H in (0001) orientation crystals compared to $(000\bar{1})$ orientation crystals, and the increasing (0001) crystal quality with growth zone fluid temperature.

3.3.3.1 *(0001) Orientation*

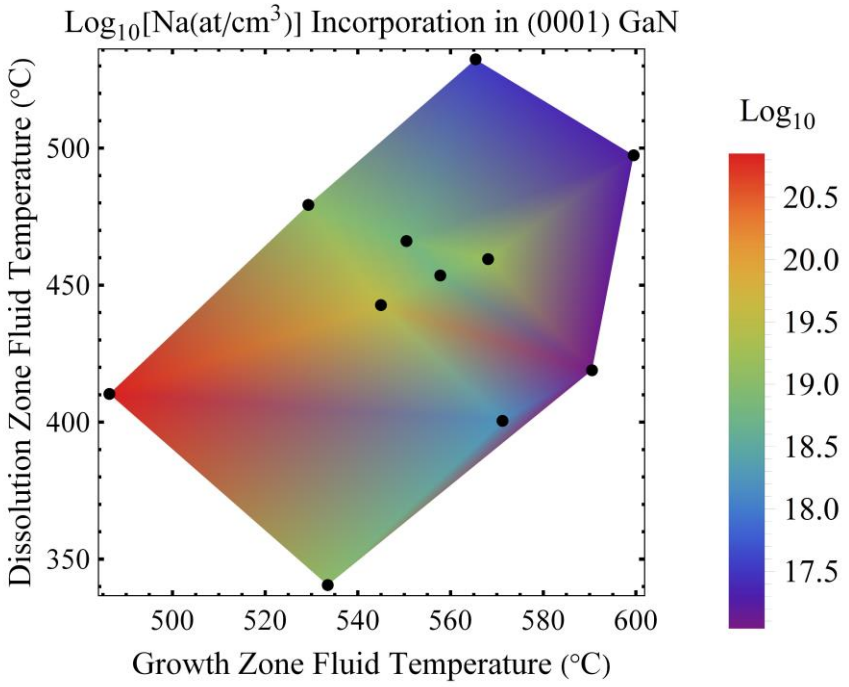

Figure 3-26. Na incorporation in (0001) GaN. Dissolution temp. r = -0.23; Growth temp. r = -0.74.

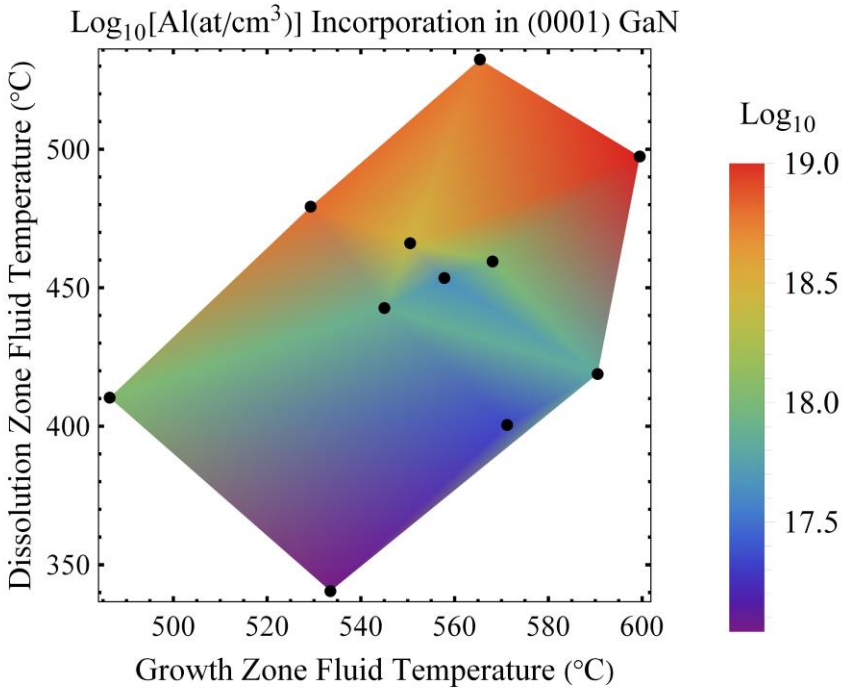

Figure 3-27. Al incorporation in (0001) GaN. Dissolution temp. r = 0.71; Growth temp. r = 0.32.

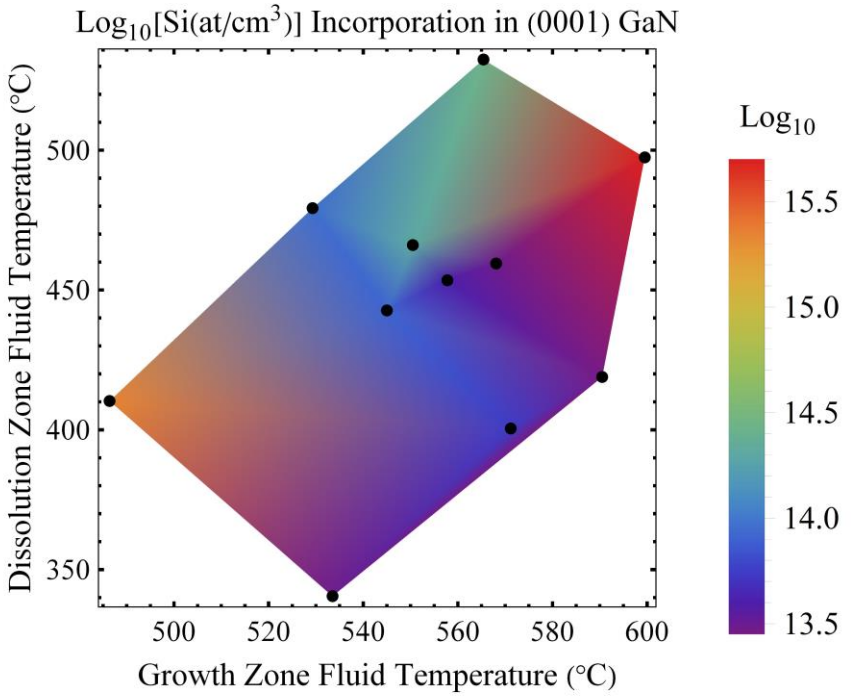

Figure 3-28. Si incorporation in (0001) GaN. Dissolution temp. r = 0.25; Growth temp. r = 0.16.

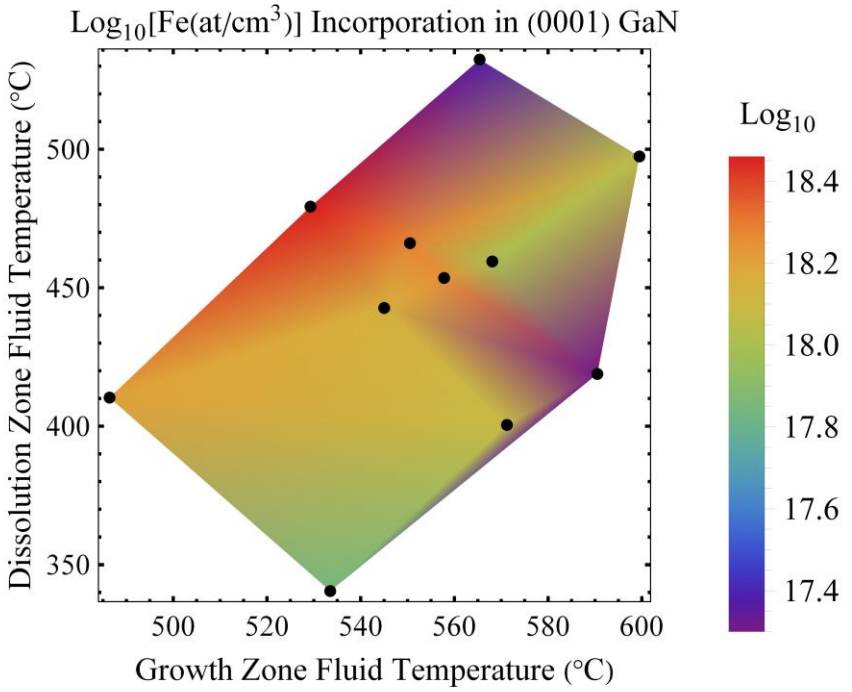

Figure 3-29. Fe incorporation in (0001) GaN. Dissolution temp. r = 0.12; Growth temp. r = -0.48.

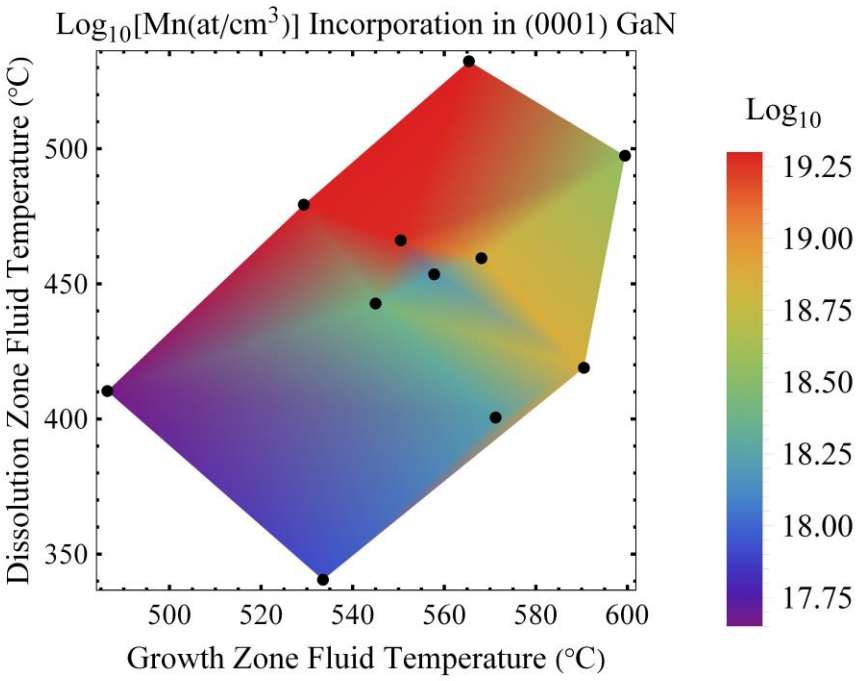

Figure 3-30. Mn incorporation in (0001) GaN. Dissolution temp. r = 0.65; Growth temp. r = 0.05.

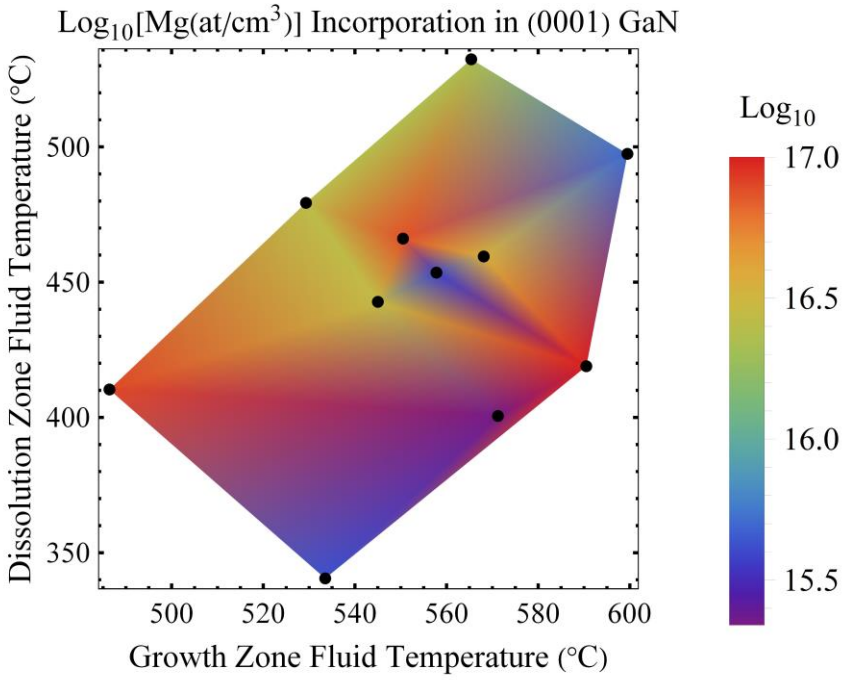

Figure 3-31. Mg incorporation in (0001) GaN. Dissolution temp. r = -0.06; Growth temp. r = -0.19.

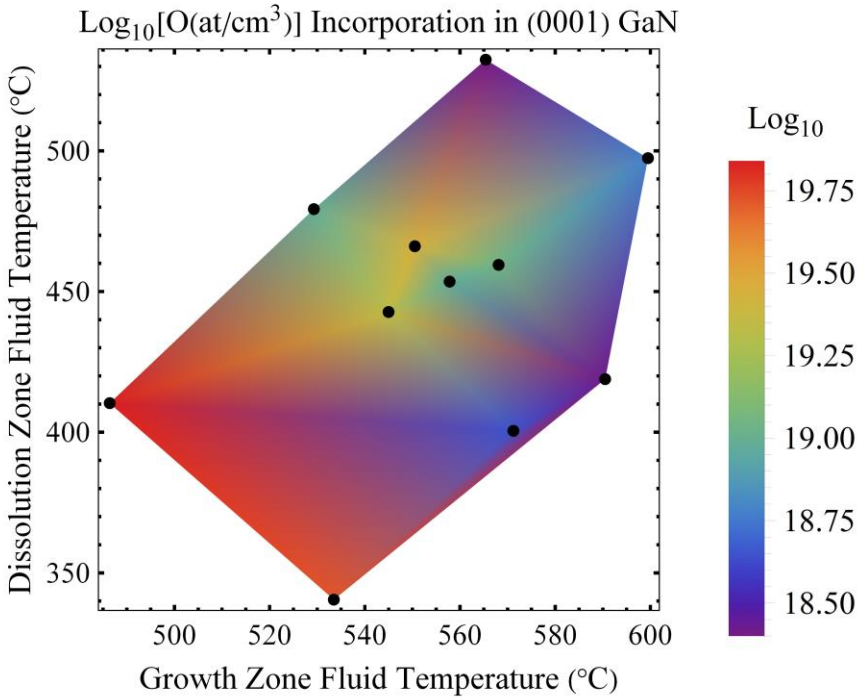

Figure 3-32. O incorporation in (0001) GaN. Dissolution temp. r = -0.58; Growth temp. r = -0.82.

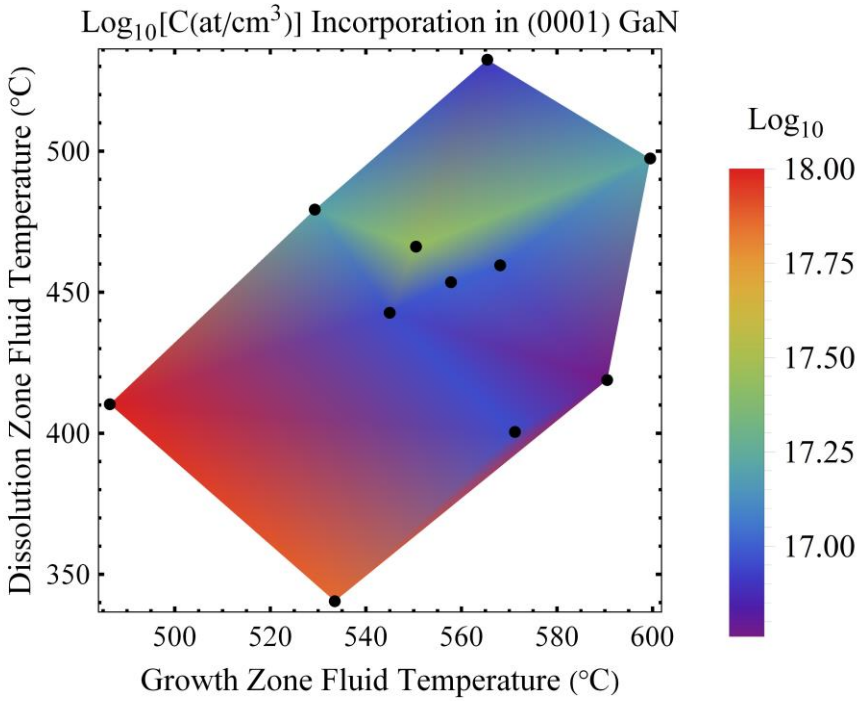

Figure 3-33. C incorporation in (0001) GaN. Dissolution temp. r = -0.55; Growth temp. r = -0.78.

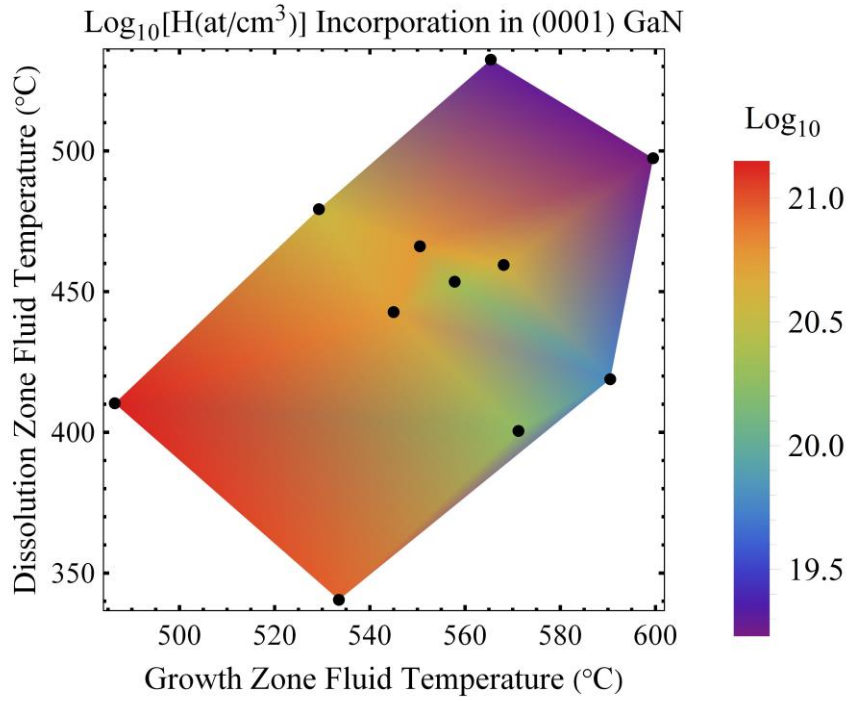

Figure 3-34. H incorporation in (0001) GaN. Dissolution temp. r = -0.55; Growth temp. r = -0.89.

3.3.3.2 *(000$\bar{1}$) Orientation*

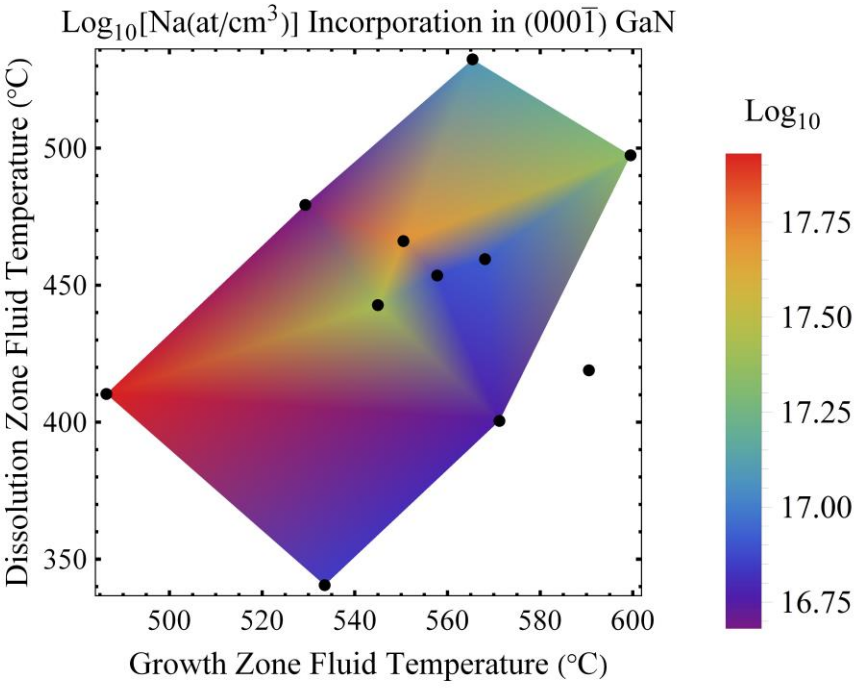

Figure 3-35. Na incorporation in (000$\bar{1}$) GaN. Dissolution temp. r = -0.09; Growth temp. r = -0.61.

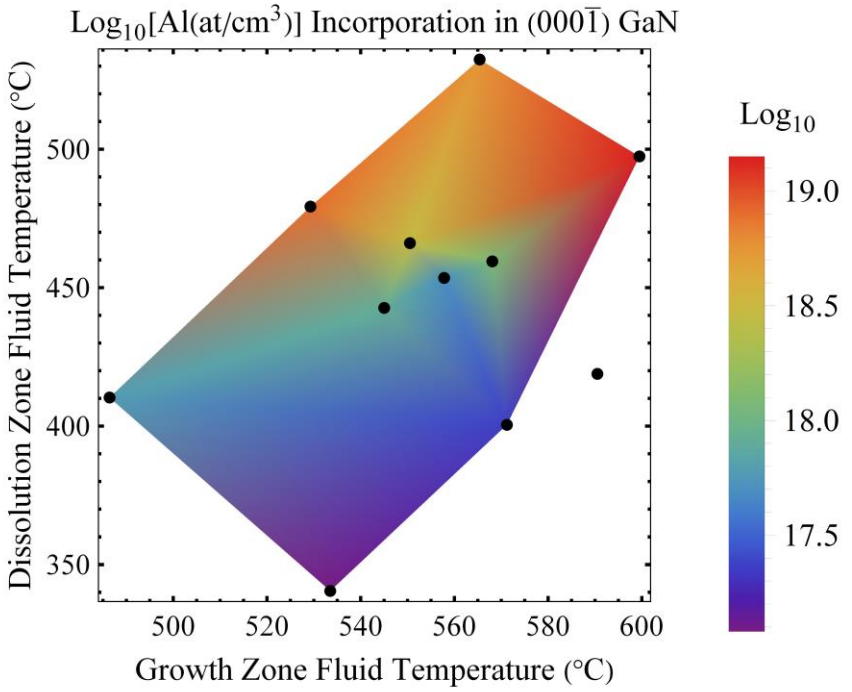

Figure 3-36. Al incorporation in (000$\bar{1}$) GaN. Dissolution temp. r = 0.65; Growth temp. r = 0.47.

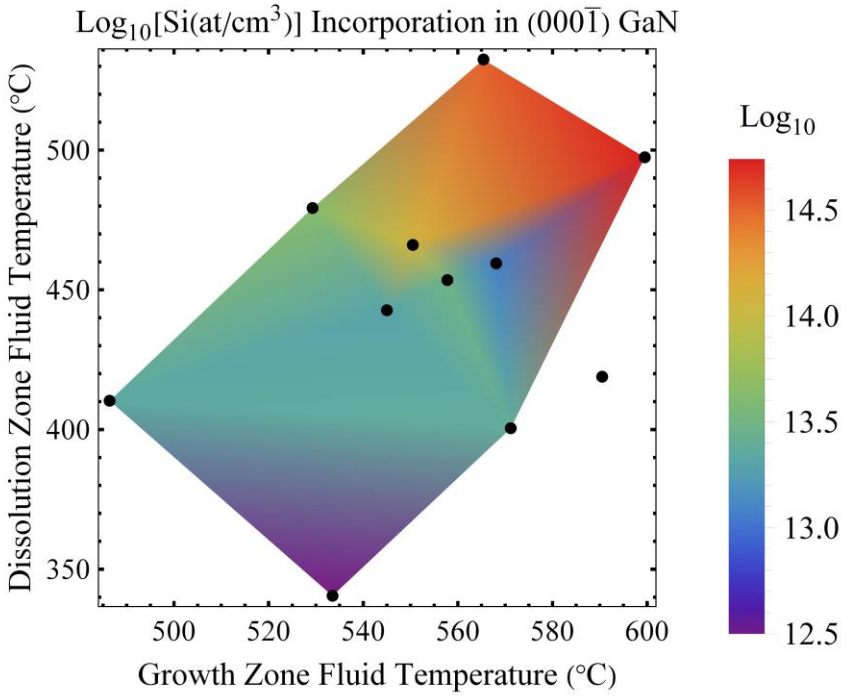

Figure 3-37. Si incorporation in (000$\bar{1}$) GaN. Dissolution temp. r = 0.64; Growth temp. r = 0.60.

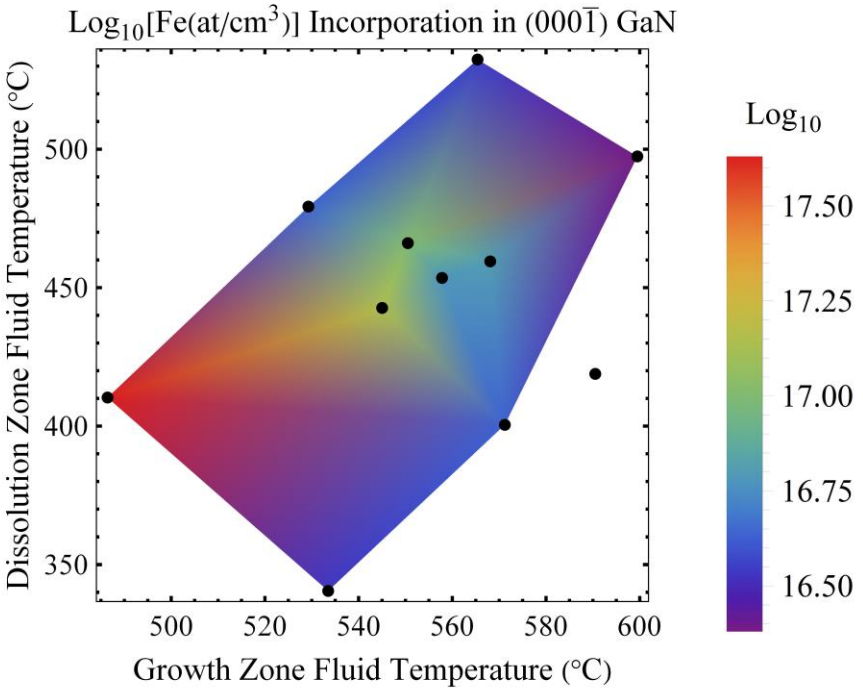

Figure 3-38. Fe incorporation in (000$\bar{1}$) GaN. Dissolution temp. r = -0.24; Growth temp. r = -0.78.

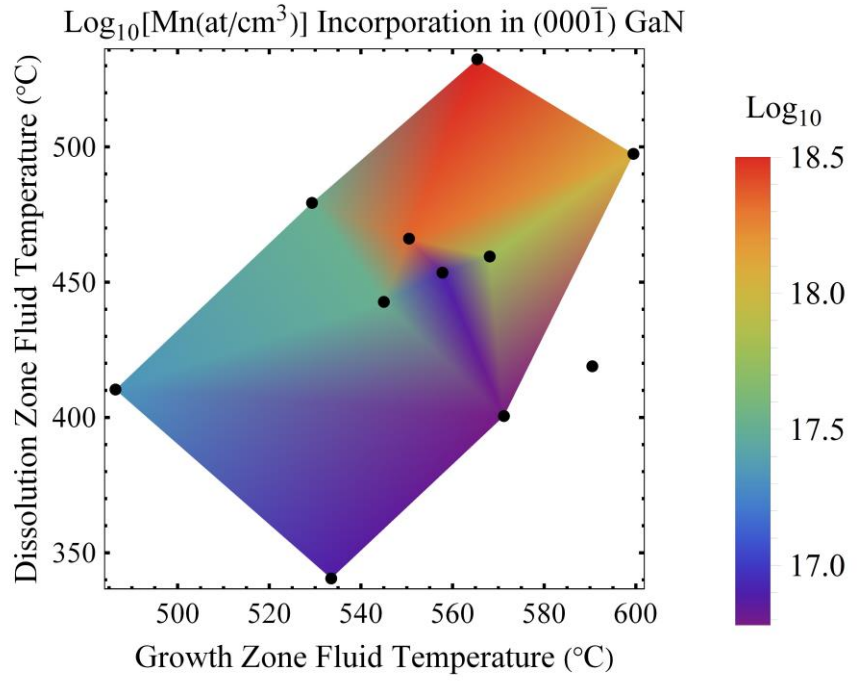

Figure 3-39. Mn incorporation in (000$\bar{1}$) GaN. Dissolution temp. r = 0.70; Growth temp. r = 0.32.

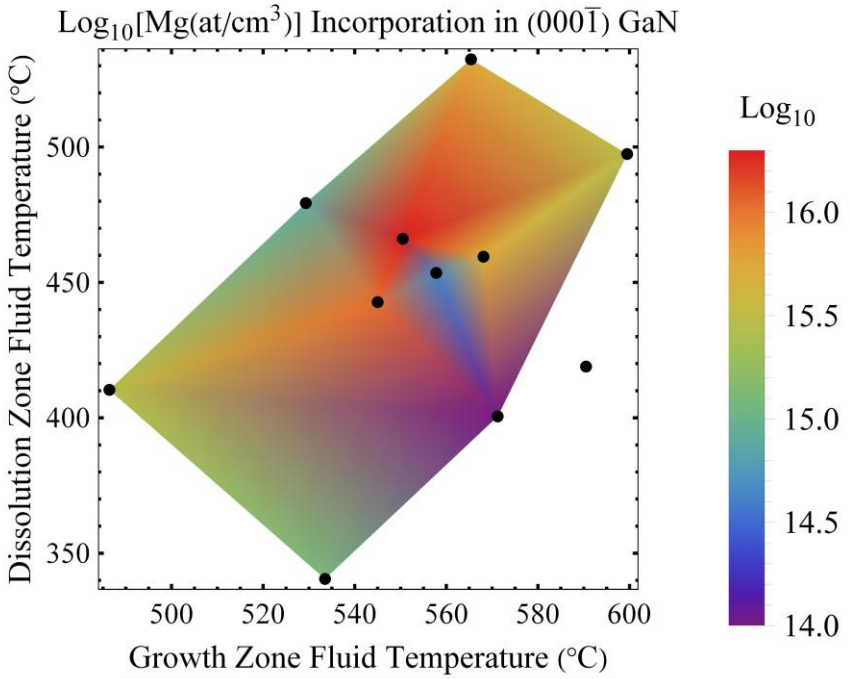

Figure 3-40. Mg incorporation in (000$\bar{1}$) GaN. Dissolution temp. r = 0.25; Growth temp. r = 0.02.

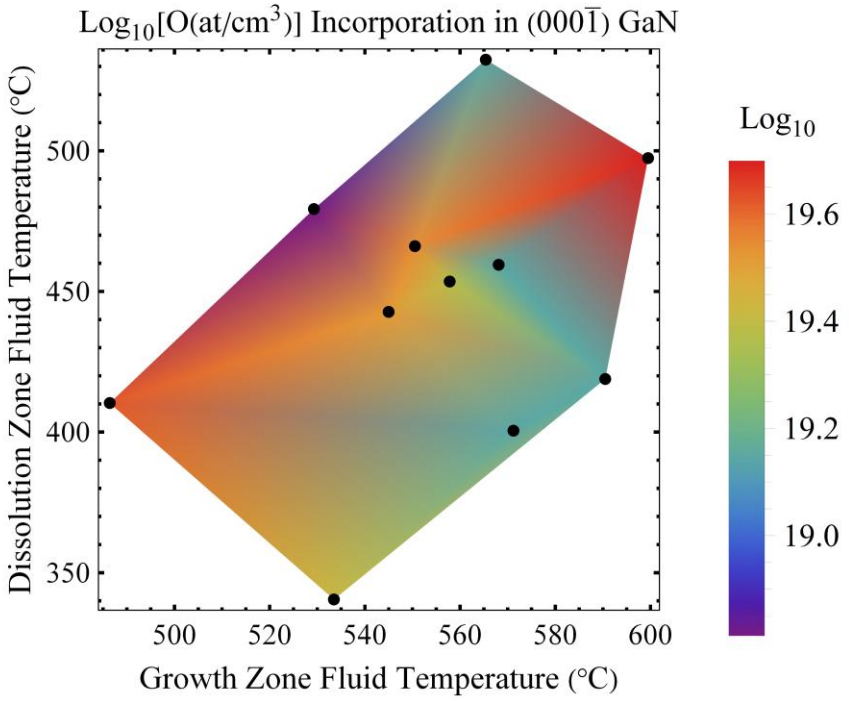

Figure 3-41. O incorporation in (000$\bar{1}$) GaN. Dissolution temp. r = -0.02; Growth temp. r = -0.13.

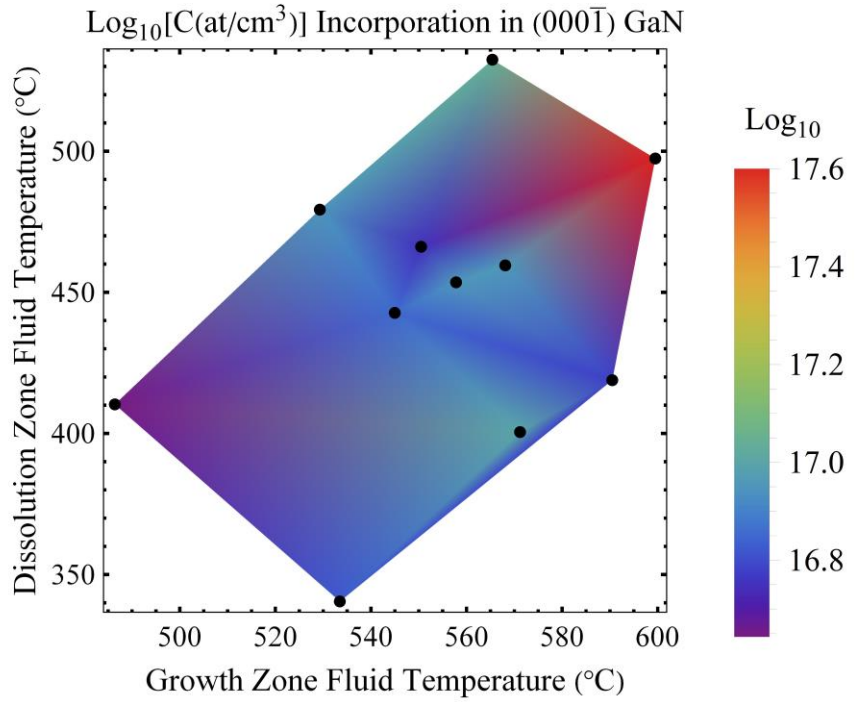

Figure 3-42. C incorporation in (000$\bar{1}$) GaN. Dissolution temp. r = 0.42; Growth temp. r = 0.56.

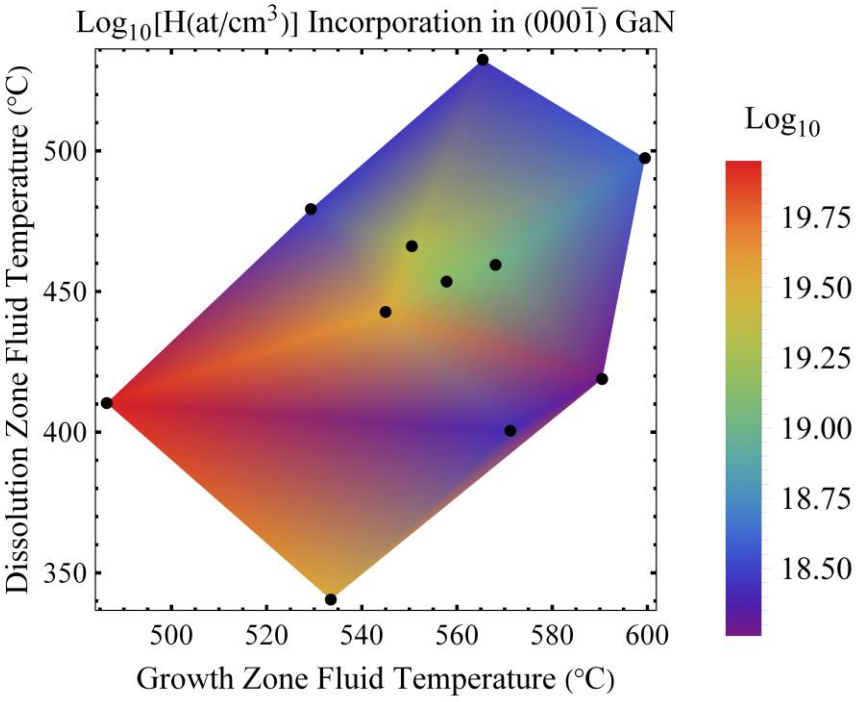

Figure 3-43. H incorporation in (000$\bar{1}$) GaN. Dissolution temp. r = -0.41; Growth temp. r = -0.82.

3.4 Summary

Bulk GaN crystal growth kinetics, crystal quality, and impurity incorporation were correlated to ammonothermal dissolution and growth zone fluid temperatures in supercritical NH_3-Na solutions through the course of 12 week-long crystal growth experiments. To allow direct measurement of the supercritical fluid, a novel baffling assembly was developed in tandem with internal thermocouple probes. These fluid temperature measurements provided direct experimental evidence to confirm the retrograde solubility of GaN in supercritical NH_3-Na solutions in the temperature and pressure regimes of interest (~350 – 600°C and ~180 – 260 MPa, respectively).

Two dominant bulk GaN growth regimes were identified in this system: a mass transport limited regime at low extrapolated fluid density gradients (<1.2 mol/L), and a surface integration limited regime above this critical fluid density gradient. In surface integration limited growth, two different Arrhenius processes appear to dominate, one above and one below ~570°C. Further analysis is needed to ascertain the specific Arrhenius processes at play. Knowledge of polar {0001} and nonpolar $\{10\bar{1}0\}$ growth kinetics enabled the assessment of crystal shape evolution with growth zone fluid temperature. It was found that equiaxed crystals (equivalent {0001} and $\{10\bar{1}0\}$ growth rates) are favored at high growth zone temperature, and needle-like crystals (high {0001} growth rates compared to $\{10\bar{1}0\}$) are favored at low growth zone temperature. Additional experiments are needed to determine if $\{10\bar{1}0\}$ growth rates will exceed {0001} at temperatures beyond those measured in this study.

The crystal quality of (0001) orientation ammonothermal material was found to be highly correlated with growth zone fluid temperature, requiring temperatures in excess of ~575°C to match or improve the quality of the HVPE seed crystal. The crystal quality of the

$(000\bar{1})$ orientation material, by comparison, was not obviously affected by growth zone fluid temperature. Al, Si, and Mn impurities, identified using SIMS, were found to incorporate in the growing crystals more readily at high dissolution zone fluid temperature, implying they either originate in the poly GaN source material, or become activated from a greater autoclave volume at elevated temperatures. Na, Fe, O, and H impurities were reduced with increasing growth zone fluid temperature, in a consistent fashion with defect-site incorporation.

Chapter 4 Growth of Bulk Group-III Nitride Crystals from Group-III Alloy Source Materials in Supercritical Ammonia-Sodium Solutions

4.1 Motivation

As outlined in the previous chapters of this work, ammonothermal growth is typically practiced with poly GaN source material and single crystal GaN seeds. The temperature dependence of the GaN solubility curve is utilized to dissolve, transport, and crystallize GaN on the seed crystals. The purpose of utilizing the temperature dependence of solubility as a crystal growth "knob", as opposed to the pressure dependence for instance, is a matter of convenience when growing from solution in a nominally-isobaric system. As long as the source material is the same composition as the desired crystalline product, supersaturation in the growth zone must be achieved by manipulating some parameter that modulates solubility. This constraint limits both the design of the growth system, and the type of crystal that can be grown in said system. For example, it was shown in Chapter 3 that extreme forward and reverse internal fluid temperature gradients, and high global fluid temperatures, were difficult to achieve due to the geometry and material selection (Rene 41) of the autoclave, in addition to the baffling design. One might be able to adjust the aspect ratio of the autoclave to increase the achievable temperature gradients and global temperatures, but there will inevitably be some fundamental limit reached, whether it is in the production of a Rene 41 ingot of suitable size/grain structure, or in the thermal management of an autoclave with poor heat transport properties.

An even greater challenge, as previously alluded to, is the development of a crystal growth method that does not rely on a competing technique for source material and seed crystals. The standard at UCSB, and presumably in the ammonothermal community at large, is HVPE-produced source and seed GaN. Early on in the development of ammonothermal growth, Ga metal was attempted as a source material, but it was found to be too difficult to control supersaturation in the system, as GaN is always more stable than Ga in the presence of NH_3 at these conditions [49][57]. Eventually the field moved on to limited success with in situ conversion of Ga to GaN in the dissolution zone before growth was initiated, or to source materials produced by competing techniques, such as HNPS or HVPE. Seeds were/are produced either through heterogeneous nucleation on the autoclave wall, or from the same competing techniques.

While the ammonothermal growth of GaN has enjoyed many research successes by utilizing HVPE source/seed materials, there have also been many shortcomings. It has been verified in this work, and in others, that HVPE materials act as impurity sources (for some, but not all observed impurities) for ammonothermally-grown material [79]. Furthermore, the crystal quality of HVPE GaN seeds, while improving, may be a limiting factor in the resultant ammonothermally-grown crystals. Another challenge, which has been ignored by the bulk GaN community at large, is that of an application specific, lattice-matched substrate. Since most Nitride devices are actually composed of a stack of materials in a ternary alloy system (e.g. InGaN/GaN for visible optoelectronics, and AlGaN/GaN for UV optoelectronics and power electronics), the lack of a bulk ternary Group-III Nitride substrate limits device design. Interest in tailor-made ternary Group-III Nitride substrates has been expressed, but little work has been done to realize them. The aforementioned shortcoming of ammonothermal growth

leads one to ask: 1) how can ammonothermal GaN growth be dramatically improved over the competing techniques it relies on, and 2) how will bulk ternary Group-III Nitride crystals be produced ammonothermally if competing techniques cannot/will not produce them to begin with? The answers to these questions clearly entail removing the dependence of ammonothermal growth on competing techniques, like HVPE, for source material production. What follows in this chapter is the theoretical foundation of a new supercritical NH_3-Na solution growth technique for bulk GaN crystals. This technique introduces the Ga (or other Group-III species) in the form of an alloy, and relies on the supercritical NH_3-Na solution to provide the N-species. Initial growth demonstration results will be discussed.

4.2 Thermodynamic Growth Model

The chemical potential driving force for ammonothermal growth by means of establishing a temperature gradient between GaN source and seed materials in the dissolution and growth zones, respectively, is given in Equation 2-1. As previously described, this growth model (referred to in the remainder of this chapter as "traditional ammonothermal growth") utilizes the temperature dependence of the GaN solubility curve to establish supersaturation in the growth zone. When one replaces GaN source material with metallic Ga-species, the equilibrium shown in Equation 4-1 implies that a temperature gradient is no longer required to crystallize GaN. As stated previously, this reaction resulted in Ga not being used as a source material in traditional ammonothermal growth because GaN was always thermodynamically favored over Ga [109]. Indeed, GaN growth is not useful if it occurs in a polycrystalline fashion over the source material, as opposed to the growth of a single crystal layer on a seed. However, if Ga-species can be dissolved in the supercritical NH_3-Na solution without spontaneously

nitriding, then Equation 4-1 implies that GaN growth on the seed is possible in the absence of a temperature gradient, should the dissolved Ga be transported to the seed by means of a concentration gradient in the supercritical solution.

Equation 4-1

$$\mathrm{Ga}_{\,(\mathrm{sol})} + \mathrm{NH}_{3\,(\mathrm{g})} \rightleftharpoons \mathrm{GaN}_{\,(\mathrm{s})} + \frac{3}{2}\mathrm{H}_{2\,(\mathrm{g})}$$

To prevent spontaneous nitriding of Ga, Ga-metal can be alloyed with another species, referred to in the remainder of this chapter as an "excipient alloying element". As further discussed in 4.3, the purpose of the excipient alloying element is to effectively dilute the Ga-species to prevent its nitridation, while still enabling Ga to be solvated by the supercritical NH_3-Na solution. This phenomenon has been realized before, as outlined in Ref. [95], with metallic-Ga transport to/from Ni-components. The use of a Ga-alloy source, as compared to pure metallic-Ga, is immensely important since it enables continuous isothermal growth on GaN seed crystals. A new chemical potential driving force equation for GaN growth can therefore be derived, which is source composition and temperature-modulated, instead of modulation by the temperature dependence of GaN solubility. The chemical potential driving force ($\Delta\mu$) is now pinned between the chemical potential of Ga in GaN ($\mu_{\mathrm{Ga}}^{\mathrm{GaN}}$, which represents the lower potential if growth is to occur) and the chemical potential of Ga in the source alloy ($\mu_{\mathrm{Ga}}^{\mathrm{source}}$, which represents the higher potential if growth is to occur), assuming NH_3 is added in excess with respect to Ga. An idealized expression for $\Delta\mu$ is shown in Equation 4-6, which is derived through simple thermodynamic analysis of the end-point Ga chemical potentials in Equation 4-2 - Equation 4-5.

Equation 4-2

$$\overline{G}_{\mathrm{Ga}} + \overline{G}_{NH_3} = \overline{G}_{\mathrm{GaN}} + \frac{3}{2}\overline{G}_{NH_3}$$

Equation 4-3

$$\overline{G}_{\mathrm{Ga}} + \mu^0_{\mathrm{NH_3}} + \mathrm{RT} * \ln\left[\mathrm{p_{NH_3}}\right] = \mu^0_{\mathrm{GaN}} + \frac{3}{2}\mu^0_{\mathrm{H_2}} + \frac{3}{2}\mathrm{RT} * \ln\left[\mathrm{p_{H_2}}\right]$$

Equation 4-4

$$\overline{G}_{\mathrm{Ga}} \equiv \mu^{\mathrm{GaN}}_{\mathrm{Ga}} = \mu^0_{\mathrm{GaN}} + \frac{3}{2}\mu^0_{\mathrm{H_2}} - \mu^0_{\mathrm{NH_3}} + \mathrm{RT} * \ln\left[\frac{\mathrm{p}^{3/2}_{\mathrm{H_2}}}{\mathrm{p_{NH_3}}}\right]$$

Equation 4-5

$$\mu^{\mathrm{source}}_{\mathrm{Ga}} = \mu^0_{\mathrm{Ga}} + \mathrm{RT} \cdot \ln[\gamma^{\mathrm{source}}_{\mathrm{Ga}} * \mathrm{X}^{\mathrm{source}}_{\mathrm{Ga}}]$$

Equation 4-6

$$\Delta\mu \equiv \mu^{\mathrm{source}}_{\mathrm{Ga}} - \mu^{\mathrm{GaN}}_{\mathrm{Ga}} = \mu^0_{\mathrm{Ga}} - \mu^0_{\mathrm{GaN}} - \frac{3}{2}\mu^0_{\mathrm{H_2}} + \mu^0_{\mathrm{NH_3}} + \mathrm{RT} * \ln\left[\frac{\gamma^{\mathrm{source}}_{\mathrm{Ga}} * \mathrm{X}^{\mathrm{source}}_{\mathrm{Ga}} * \mathrm{X_{NH_3}}}{\mathrm{P}^{1/2}_{\mathrm{Tot}} * \mathrm{X}^{3/2}_{\mathrm{H_2}}}\right]$$

The symbols used in Equation 4-6 refer to the following quantities: the standard state partial molar Gibbs free energy of each component (μ_i^0), the ideal gas constant (R), the fluid temperature (T), the activity coefficient of Ga in the Ga-alloy source ($\gamma_{\mathrm{Ga}}^{\mathrm{source}}$), the mol fraction of Ga in the Ga-alloy source ($\mathrm{X}_{\mathrm{Ga}}^{\mathrm{source}}$), the mol fraction of NH_3 in the fluid ($\mathrm{X_{NH_3}}$, as defined by Equation 4-7), the mol fraction of H_2 in the fluid ($\mathrm{X_{H_2}}$, as defined by Equation 4-8), and the total system pressure (P_{Tot}, equivalent to the sum of the NH_3 and H_2 partial pressures, $\mathrm{p_{NH_3}}$ and $\mathrm{p_{H_2}}$, defined in Equation 4-9 and Equation 4-10, respectively). It should be noted that Equation 4-9 and Equation 4-10 assume ideal mixing of each component gas.

Equation 4-7

$$X_{NH_3} \equiv \frac{n_{NH_3}}{n_{NH_3} + n_{H_2}}$$

Equation 4-8

$$X_{H_2} \equiv \frac{n_{H_2}}{n_{NH_3} + n_{H_2}}$$

Equation 4-9

$$p_{NH_3} \equiv X_{NH_3} P_{Tot}$$

Equation 4-10

$$p_{H_2} \equiv X_{H_2} P_{Tot}$$

To first order, the fluid composition can be assessed by assuming that two reactions proceed to completion. The first reaction was given by Equation 4-1, which allows one to assess how much NH_3 is consumed and how much H_2 is evolved, given the amount of Ga added to the system (again, NH_3 is added in excess). The second reaction that is assumed to take place involves the formation of $NaNH_2$ from Na-metal. This reaction is shown in Equation 4-11, with the NH_3 added in excess (allowing a similar calculation of NH_3 consumption and H_2 evolution if the reaction proceeds to completion). The gas contributions from each reaction are summed, which allows for the mol fractions of NH_3 and H_2 to be quantified by the amount of each species added to the autoclave, shown in Equation 4-12 and Equation 4-13, respectively. The initial molar fill of NH_3 is represented by $n_{NH_3}^{i}$, while n_{Ga} and n_{Na} represent the added molar quantities of Ga and Na, respectively. Equation 4-12 and Equation 4-13 are substituted into Equation 4-6 to yield an expanded form of the chemical potential driving force expression in Equation 4-14 (where the standard state contributions are summed in the term $\Delta\mu^0$, defined by Equation 4-15). It should be noted that the effects of NH_3 decomposition and

H_2 diffusion are neglected for simplicity in this analysis. In reality, there will also be N_2 present in the fluid due to these processes.

Equation 4-11

$$\mathrm{Na}_{(s)} + \mathrm{NH}_{3\,(g)} \rightleftharpoons \mathrm{NaNH}_{2\,(s)} + \frac{1}{2}\mathrm{H}_{2\,(g)}$$

Equation 4-12

$$\mathrm{X}_{\mathrm{NH}_3} = \frac{n^i_{NH_3} - \mathrm{n}_{Ga} - \mathrm{n}_{Na}}{n^i_{NH_3} + \frac{1}{2}\mathrm{n}_{Ga} - \frac{1}{2}\mathrm{n}_{Na}}$$

Equation 4-13

$$\mathrm{X}_{\mathrm{H}_2} = \frac{\frac{3}{2}\mathrm{n}_{Ga} + \frac{1}{2}\mathrm{n}_{Na}}{n^i_{NH_3} + \frac{1}{2}\mathrm{n}_{Ga} - \frac{1}{2}\mathrm{n}_{Na}}$$

Equation 4-14

$$\Delta\mu = \Delta\mu^0 + \mathrm{RT} * \ln\left[\frac{\gamma^{\mathrm{source}}_{\mathrm{Ga}} * \mathrm{X}^{\mathrm{source}}_{\mathrm{Ga}}\left(n^i_{NH_3} - \mathrm{n}_{Ga} - \mathrm{n}_{Na}\right) * \left(n^i_{NH_3} + \frac{1}{2}\mathrm{n}_{Ga} - \frac{1}{2}\mathrm{n}_{Na}\right)^{1/2}}{\mathrm{P}^{1/2}_{\mathrm{Tot}}\left(\frac{3}{2}\mathrm{n}_{Ga} + \frac{1}{2}\mathrm{n}_{Na}\right)^{3/2}}\right]$$

Equation 4-15

$$\Delta\mu^0 \equiv \mu^0_{\mathrm{Ga}} - \mu^0_{\mathrm{GaN}} - \frac{3}{2}\mu^0_{\mathrm{H}_2} + \mu^0_{\mathrm{NH}_3}$$

There are two important consequences that can be realized through this derivation of the chemical potential driving force. First, as previously mentioned, it is now clear that GaN growth can be achieved isothermally, and that the magnitude of the driving force can be changed by altering the composition of the Ga-alloy source, the total system temperature and pressure, and the amount of additional chemistry (Na mineralizer, and NH_3 added to achieve said pressure). Secondly, it is clear that the addition of excipient alloying elements reduces the

driving force by the natural logarithm term in Equation 4-6, when comparing growth from a pure Ga source to growth from a Ga-alloy source. The driving force reduction is required to prevent spontaneous nitriding of Ga in the supercritical NH_3-Na fluid.

4.3 Selection of Excipient Alloying Elements

The choice of the proper excipient element to form the Ga-alloy source is critical for the success of any isothermal growth experiment in supercritical NH_3-Na solutions. There are three primary requirements of the excipient alloying element: 1) that it is chemically-stable in the supercritical NH_3-Na solution (i.e. it will not dissolve or react), 2) that it does not form a competitive nitride with Ga, and 3) that is sufficiently miscible with Ga to form an alloy. An additional preference is that the excipient alloying element poses no extreme health hazards to humans, for ease of handling.

The stability criterion can be addressed by a study which was performed at UCSB in 2013. The purpose of this study was to survey a broad range of materials (ceramics, metals, and metalloids) to assess their behavior in basic (NH_3-Na), acidic (NH_3-NH_4Cl), and neutral (NH_3) ammonothermal chemistries. The cumulative results of this survey study are given in Appendix A, but the elements which were found to be unstable in supercritical NH_3-Na solutions include: Al, Au, Cu, Ge, Mg, Pd, Pt, Si, Ta, Ti, W, Y, and Zr [47]. The alkali, alkaline earth, and halide elements are also excluded from the list of candidate excipient alloying elements because they tend to modify the NH_3 dissociation reaction as effective mineralizer species. Also, for practical reasons, the gaseous and non-earth-abundant elements are also excluded. Many of the aforementioned unstable elements form nitride compounds, but some elements excluded from that list also form nitride compounds, the majority of which are considered more stable than GaN by Ellingham diagram analysis. These potentially-stable,

competitive nitriding elements include: B, Ce, Cr, Fe, Mo, Nb, and V. Also, elements which are considered by the National Fire Protection Association (NFPA) as a health hazard of 3 or 4 are excluded as potential excipient alloying elements due to safety/handling concerns, and these include: As, Cd, Hg, and Po. The remaining candidate elements which meet the aforementioned criteria are listed in Table 4-1, along with specific data obtained from their respective binary phase diagrams with Ga.

Table 4-1. Binary phase data from potential excipient alloying elements. Represented are the liquidus and solidus compositions at 600°C, the eutectic compositions (and temperatures), and largest liquid miscibility gap composition range (at the lowest temperature it exists).

Element	Liquidus at 600°C (at.% Ga)	Solidus at 600°C (at.% Ga)	Eutectic Points **at.% Ga** (°C)	Liquid Miscibility Gap Range **at.% Ga** (°C)
Bi [110]	--	--	**39** (222), **92** (222), **99** (29)	**39-92** (222)
Pb [111]	--	--		**6-98** (317)
Sn [112]	--	--	**92** (21), **99** (29)	--
Tl [113]	--	--		**2-96** (286)
Ag [114]	30	23	**99** (26)	--
Co [115]	97	75	**99** (29)	--
Gd [116]	98	78	**20** (850), **99** (29)	--
Hf [117]	96	75	**20** (1477), **43** (1677), **99** (29)	--
Ni [91]	91	62	**31** (1217), **99** (29)	--
Sb [118]	88	50	**12** (589), **99** (29)	--

Sc [119]	96	75	**20** (1060), **57** (1070), **99** (29)	--
Te [120]	99	50	**10** (440), **44** (785)	--
Yb [121]	90	80	**22** (605), **54** (880), **99** (27)	--

It should be noted that the values given in Table 4-1 are generally measured at atmospheric pressure, so it is difficult to say with great confidence if these quantities increase or decrease at ~200 MPa. The liquidus and solidus compositions at 600°C are meant to give the reader an impression of the composition range over which the binary alloy systems will have solid phases in equilibrium with liquid solution at realistic ammonothermal temperatures. Ga has a low melting point (~30°C) by comparison to these excipient alloying element candidates, which is why the liquidus and solidus compositions at 600°C are generally at high Ga concentrations, and also why the low temperature eutectic compositions are very nearly pure Ga. Bi, Pb, Sn, and Tl also have fairly low melting temperatures, so their binary phase equilibria favor liquid solutions over the entire composition range for realistic ammonothermal temperatures (>400°C). Liquid phase miscibility gaps are realized across large composition ranges for Ga alloys with Bi, Pb, and Tl. The values given in Table 4-1 to represent this behavior refer to the lowest temperature, and widest composition range, that the two-phase liquid is observed. The miscibility gap composition range narrows with increasing temperature until it disappears at 262°C for Bi [110], ~610°C for Pb [111], and 576°C for Tl [113], respectively. It should be noted that Ir, Os, Rh, and Ru appear to pass the aforementioned excipient alloying element criteria, but no binary phase diagrams could be found for them with

Ga (although various intermediate species have been synthesized for each, suggesting some miscibility with Ga), therefore they were excluded from Table 4-1.

An important consequence of excipient alloying element selection is that it enables precise control of the phase(s) present in the Ga-alloy source. If one selects a composition that is nominally single-phase, the source will lose Ga to the supercritical fluid as growth occurs, thereby reducing the chemical potential driving force for growth as the process proceeds (according to Equation 4-14). It is possible that if a solid, single-phase source is used, that crystal growth kinetics may be limited by the diffusion of Ga in the bulk of the alloy to the surface, where it is dissolved by the supercritical fluid. It is likely that Ga-diffusion would proceed faster in a liquid single-phase source.

It is also possible to structure the Ga-alloy source as a two-phase system. It is expected that if this were the case, Ga would be depleted from the phase in closest proximity to the supercritical fluid by means of traversing the "tie-line" in the two-phase region of the relevant phase diagram. Traversing the tie-line entails the Ga-poor phase present in the source growing at the expense of the Ga-rich phase by means of Ga and excipient element redistribution, until the Ga-rich phase completely disappears. This implies that while the Ga-alloy source is two-phase, μ_{Ga}^{source} is pinned by the composition of the Ga-poor phase, and that growth occurs under constant chemical potential driving force. This might be desired for crystal growth uniformity. Two-phase sources can be designed with two solid phases (if operating below the solidus composition), two liquid phases (if a liquid miscibility gap is present), and a solid and liquid phase (if operating between the solidus and liquidus compositions). It is important to note that any choice of excipient alloying element will most likely entail deviations from binary phase behavior with Ga. As mentioned before, an idealized Ga-alloy source would not interact

chemically with the supercritical fluid or autoclave components, but by means of intimate contact with the ammonothermal environment it is likely that Na, N, Ni, and other elements will be present in the source (whether at a contamination level, or to the extent of forming a ternary or higher order alloy).

4.4 Experimental Methods

Isothermal crystal growth was performed on HVPE GaN seed crystals in supercritical NH_3-Na solutions from various Ga-alloy source materials. The molar fill ratio of NH_3:Na (20:1) and the target total system peak pressure (200 MPa) were kept the same as the studies in Chapter 2 and Chapter 3 . These growth runs were typically conducted for one week or less, as the primary focus of this study was to determine if growth from these alloys was possible. The experimental setup was nearly identical to that which was described in 2.2, shown schematically in Figure 2-2, in which an internal thermocouple probe was used to measure the supercritical fluid. Small Rene 41 or Inconel 625 autoclaves (with free volumes of ~60-70 mL) were utilized, as it was easier to establish a uniform internal temperature condition than with taller, large volume autoclaves.

The Ga-alloy source materials used in this study were produced by a variety of methods. A tube furnace (Thermolyne 79300) was utilized to prepare Ga-Ni alloys in the first generation of experiments. For these alloys, Ga pellets (99.9999% pure) and Ni foil pieces (99.5% pure) were measured using a high precision balance (Mettler Toledo AB135-S/FACT, precision: ± 0.01 mg). The Ni was subsequently solvent cleaned in sonicated baths of acetone, isopropanol, and de-ionized water. The raw metals were then added to a pyrolytic boron nitride (PBN, 99.99% pure) crucible, which was held in the tube furnace at 1000°C for 3 days in a N_2-

ambient. The mass of each alloy was checked after tube furnace heat treatment, which verified that negligible mass was lost during the alloying process. The second generation of alloys were prepared using an Ar-ambient arc melter (Centorr Series 5 Bell Jar). These alloys employed Ag (99.99% pure) as the excipient alloying element, with either Ga or Al (99.99% pure) as the Group-III species. The raw metals were measured and cleaned using the processes previously described. The metals were then added to either a PBN crucible or Fabmate (99.9995% pure C) crucible and placed in the arc melter. Alloying was performed by striking an arc across the crucible, letting the crucible contents melt, then rapidly quenching the melt by extinguishing the arc and allowing the crucible to equilibrate with a water-cooled copper heat sink. The alloy was then flipped-over in the crucible, and the melting process was repeated. This "melt-quench-flip" process was repeated 3-4 times per alloy to target a homogenous structure, however, coupled XRD-scans of the top and bottom of selected alloy "slugs" indicated that some inhomogeneous grain structure remained (perhaps because the quench process was not rapid enough). Again, post-processing mass measurements indicated that negligible mass was lost during the alloying process. Growth utilizing a third generation of alloys, with Pb (99.999% pure) as an excipient element, was also attempted. Due to the moderate toxicity of Pb and its low melting point, this alloying process was attempted in a N_2-ambient glovebox using a conventional hotplate. This time, however, the raw metals were melted in a Ti-Zr-Mo alloy (TZM) crucible. Once again, post-processing measurements suggested that negligible mass was lost during alloying.

As previously stated, the experimental setup was nearly identical to Figure 2-2. In these experiments, however, the poly GaN basket was replaced within either a PBN or TZM crucible which contained the Ga-alloy source material. This crucible was also placed on an Inconel 625

standoff, so as to keep the source material from being submerged in the Na-rich phase. GaN seed crystals were prepared as previously described in 3.2. These crystals were hung on Ni-Cr wire directly above the Ga-alloy source-containing crucible. The Na and NH_3 were added to the autoclave assembly as previously described in this work. After the isothermal growth run was complete, the contents of the autoclave were extracted in an attempt to separate the source material from the crystalline products produced on the seed(s) and autoclave wall. EDX and powder XRD analyses were performed on these products to determine their composition (and phase-identification, where appropriate).

4.5 Results and Discussion

What follows in this section is a brief description of bulk Group-III Nitride growth results, organized by the desired crystalline product and excipient alloying element. The nominal initial alloy source composition is shown on each respective binary phase diagram according to the masses of the raw metals used in production of the alloy, and the temperature that the growth experiment was conducted at. It should be noted that additional intermediate phases may be present in the alloy source materials (i.e. other phases than one would anticipate by the masses and growth temperature, alone), which could be the result of slow quenching from the melt during the alloying process. The resulting crystals are shown in each section, with the added growth thicknesses indicated. Additional characterization results are presented where appropriate. It is important to emphasize that these results are only intended to demonstrate the feasibility of isothermal, bulk Group-III Nitride crystal growth from alloy source materials. Further studies are required to make definitive statements on the specific growth mechanisms at play, and the fundamental limits of this technique as a bulk crystal growth method.

4.5.1 Growth of Bulk GaN

4.5.1.1 *From Nickel-Containing Sources*

A Ga-Ni alloy source, of nominal composition Ga_4Ni, was prepared using a tube furnace as previously described. The growth experiment was conducted at 500°C, which as indicated by Figure 4-1, should have resulted in a Ga-rich liquid phase in equilibrium with Ga_3Ni_2. It should be emphasized once again that imperfect alloying is to be expected (especially at the temperatures that the tube furnace can achieve), therefore the phase behavior of the alloy with respect to the binary phase diagram should not be considered absolute. However, it is likely that multiple phases were present under ammonothermal conditions, therefore the constant chemical potential driving force scenario should have been achieved.

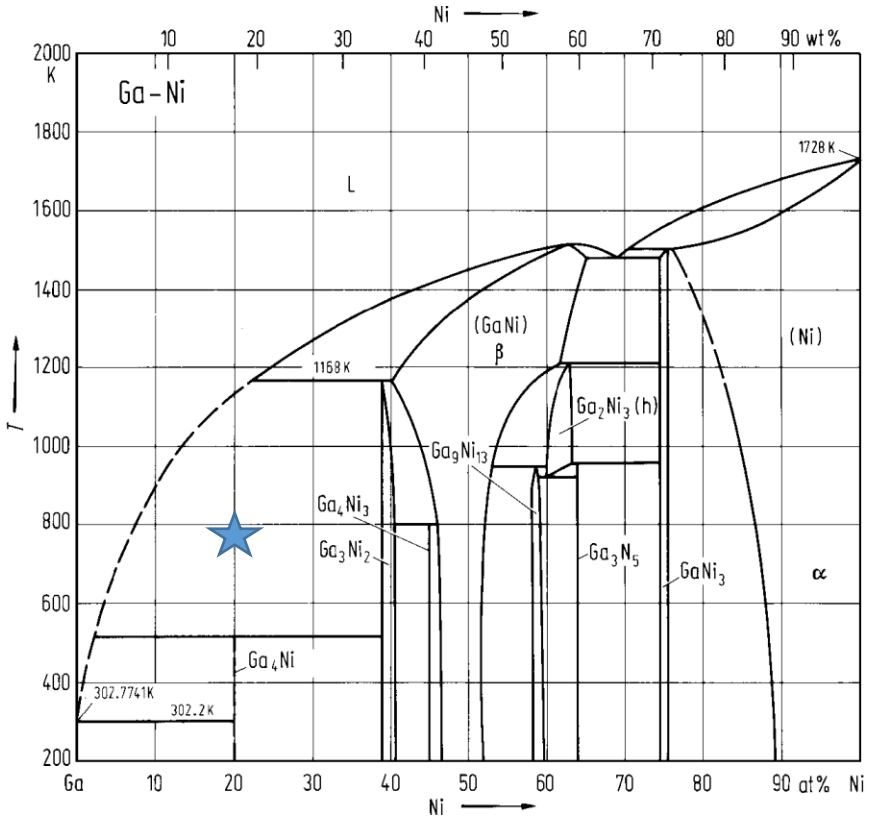

Figure 4-1. Ga-Ni binary phase diagram, with nominal Ga-alloy source initial composition at the growth temperature [91]**.**

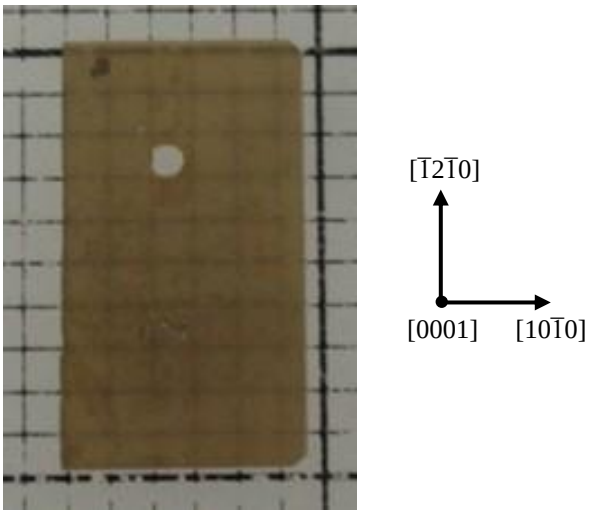

Figure 4-2. {0001}-orientation crystal resulting from the Ga-Ni alloy source experiment. The hole present in the crystal was intentionally-drilled to position it above the source material in the autoclave.

As can be seen in Figure 4-2, a total growth thickness of 67 μm was achieved on both sides of the {0001} seed crystal over one week. Inclusions in the crystal (as can be seen on the top left corner of the crystal in Figure 4-2) and polycrystalline deposition throughout the autoclave suggest that some amount of heterogeneous, non-epitaxial nucleation occurred. SIMS was performed on the (0001) face of the crystal, revealing a surface O impurity incorporation of ~1E19 at/cm^3. It should be noted that the O incorporation seemed to be dropping with increasing crystal thickness (i.e. not asymptoting to a constant value) from a peak magnitude of ~2E21 at/cm^3 at a depth of ~8 μm into the crystal. This was also the trend for other impurities, such as: C (surface: ~1E17 at/cm^3, peak: ~1E19 at/cm^3 at ~8 μm depth), Na (surface: ~2E18 at/cm^3 and dropping, peak: ~4E21 at/cm^3 at ~8 μm depth), Mn (surface: ~2E19 at/cm^3 and dropping, peak: ~3E20 at/cm^3 at ~6 μm depth), and Fe (surface: ~1E17 at/cm^3 and dropping, peak: ~1E18 at/cm^3 at ~6 μm depth), and Cr (surface: ~2E15 at/cm^3,

peak: ~3E17 at/cm^3 at ~10 μm depth). Al and Ni incorporation were uniform as a function of depth in the grown crystal, with magnitudes of ~3E19 at/cm^3 and ~5E17 at/cm^3, respectively.

The extremely high peak Na and O impurity incorporation and stoichiometry may suggest the presence of an initial Na_2O layer which forms on the crystal. However, by comparing the impurity incorporation at the (0001) surface with the crystals characterized in 3.3.3.1 at a comparable growth zone fluid temperature (500°C), it is clear that O, C, Na, and Fe are reduced with respect to traditional ammonothermal growth. This would suggest that impurities incorporate in the growing crystal early in the process, but steady state impurity transport to the crystal is reduced with respect to traditional ammonothermal growth, with the exception of Al and Mn impurities (although their concentrations may be reduced with increasing crystal thickness). Impurity incorporation early on in the growth process may be reduced by purifying the source material. Also, the depth at which the impurities increase from that of the seed layer (near 10-12 μm from the surface) suggests that most of the growth thickness was added to the (000$\bar{1}$) face.

4.5.1.2 *From Silver-Containing Sources*

Ga-Ag alloy sources of various compositions were prepared using an arc melter as previously described. Two week-long growth experiments were conducted at 500°C, which as indicated by Figure 4-3, were grown from sources of nominally the liquidus composition (~32 wt.% Ga) and single phase liquid solution (~60 wt.% Ga). Figure 4-4 and Figure 4-5 show the crystals grown from the liquidus composition source and single phase liquid solution source, respectively.

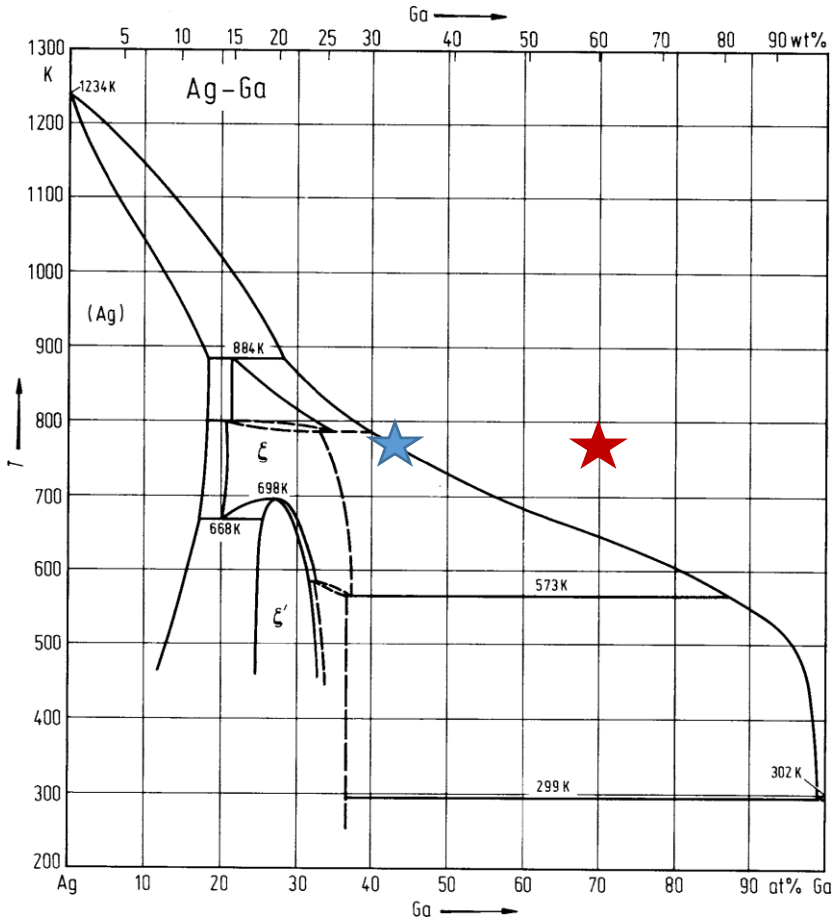

Figure 4-3. Ga-Ag binary phase diagram, with nominal Ga-alloy source initial composition at the growth temperature shown in blue for the liquidus composition and in red for the single phase liquid solution [114]**.**

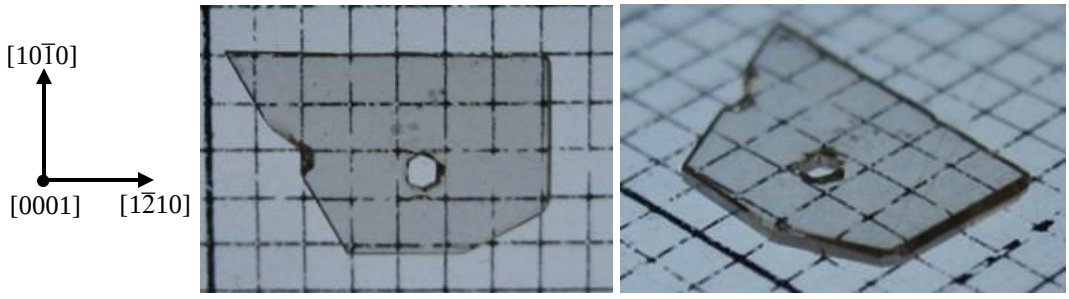

Figure 4-4. {0001}-orientation crystal resulting from the Ga-Ag liquidus composition experiment, shown in plan view and in perspective (demonstrating semipolar faceting on the (0001)-face). The hole present in the crystal was intentionally-drilled to position it above the source material in the autoclave.

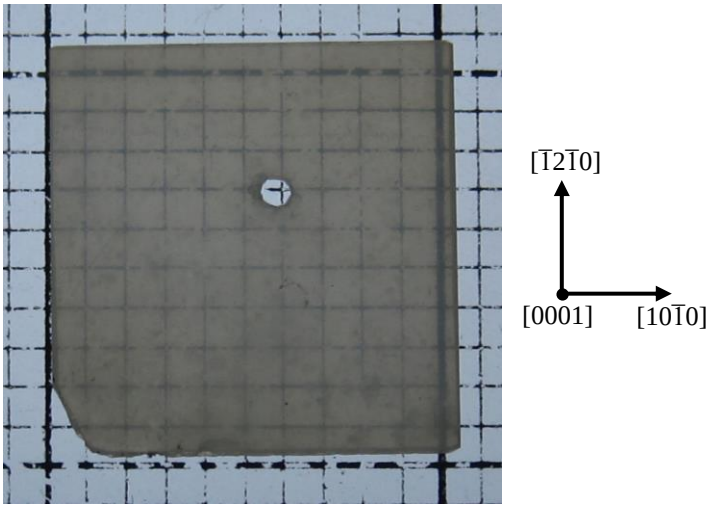

Figure 4-5. {0001}-orientation crystal resulting from the Ga-Ag single phase liquid composition experiment. The hole present in the crystal was intentionally-drilled to position it above the source material in the autoclave.

The total thickness added to both sides of the {0001} seed crystals was 40 μm for the liquidus composition source, and 105 μm for the single phase liquid solution source. Once again, inclusions in the crystal and polycrystalline deposition in the autoclave were realized for the single phase liquid solution experiment. However, there were neither crystalline inclusions nor deposition in the autoclave in the liquidus composition experiment. This may indicate that there is a threshold Ga concentration in the liquid phase (> 32 wt.% Ga), which when exceeded, causes the formation of GaN nuclei. These nuclei may form on any surface in the autoclave (due to the high μ_{Ga}^{source}) including the seed crystal. Alternatively, GaN nucleation may occur in the source material itself, which then may be transported in the supercritical fluid to the growing crystal, where it incorporates as non-epitaxially grown particles with arbitrary orientation. This explanation is consistent with the Ga-Ni source growth, which should have been composed of ~95 wt.% Ga liquid solution in equilibrium with Ga_3Ni_2.

Although the thickness of the crystal grown from the liquidus source was less than those grown from the Ga-Ni and single phase liquid solution Ga-Ag sources, it appears that the transparency was significantly improved over the other crystals beyond what one would anticipate due to the thickness reduction. Therefore, SIMS was conducted on the (0001) face of the crystal to determine if there was a reduction of impurities to match the improved transparency of the crystal. A similar impurity reduction trend with growth thickness was realized as the crystal grown from the Ga-Ni source, but all of the impurities seemed to asymptote to a steady state value at the surface, and the peak impurity incorporation occurred at a depth of only ~3 μm (which is consistent with a thinner growth layer). The magnitudes of impurity incorporation are as follows: O (surface: ~1E18 at/cm^3, peak: ~7E18 at/cm^3 at ~2.5 μm depth), C (depth independent: ~4E16 at/cm^3), Na (surface: ~1E18 at/cm^3, peak: ~3E19 at/cm^3 at ~3 μm depth), Mn (surface: ~3E18 at/cm^3, peak: ~7E18 at/cm^3 at ~2.5 μm depth), Fe (surface: ~1E17 at/cm^3, peak: ~3E18 at/cm^3 at ~3 μm depth), Cr (surface: ~1E15 at/cm^3, peak: ~2E19 at/cm^3 at ~3 μm depth), Al (depth independent: ~1E18 at/cm^3), and Ni (surface: ~1E17 at/cm^3, peak: ~2E20 at/cm^3 at ~3 μm depth).

It is apparent that both the peak impurity incorporation and surface impurity incorporation were significantly reduced in the crystal grown from the Ga-Ag liquidus source as compared to the crystal grown from the Ga-Ni source for O, C, Al, and Mn. Furthermore, the peak Na impurity incorporation was reduced for the Ga-Ag liquidus experiment, suggesting that a Na_2O layer did not form. However, the impurities seemed to be continuously dropping with increasing growth thickness for the Ga-Ni experiment, therefore the steady state impurity incorporations cannot be compared. Given that XRD analysis was not conducted on these crystals, and that SIMS was not performed on the crystal grown from a single phase liquid Ga-

Ag solution, the origin of the transparency change cannot be definitively stated. Similarly to the Ga-Ni growth experiment, the depth at which the impurities increase from that of the seed layer (near 3 μm from the surface) suggests that most of the growth thickness was added to the $(000\bar{1})$ face for the Ga-Ag liquidus experiment.

4.5.2 Growth of Bulk AlGaN

Given the success of growing transparent, low impurity GaN using the liquidus composition of the Ga-Ag alloy system at 500°C, Ag was selected as an excipient alloying element for the growth of AlGaN. Unfortunately, the ternary phase diagram is not known for the Al-Ga-Ag system. However, given the complete miscibility of Al and Ga above ~30 at.% Ga at 500°C (as shown in Figure 4-6) [122], an attempt was made to grow $Al_{0.5}Ga_{0.5}N$ using a 1:1 mol ratio of Al:Ga at the same Group-III liquidus composition as the Ga-Ag system (~32 wt.%). It is likely that the liquidus composition of the ternary Al-Ga-Ag system will increase with respect to the Ga-Ag system, given the increased melting point of Al as compared to Ga, meaning the presence of a single phase liquid solution is unlikely. The constituent metals were alloyed using an arc melter as previously described. Since the purpose of this experiment was to determine if AlGaN growth would occur at all, a semipolar $\{11\bar{2}2\}$ GaN seed was utilized, as it has been found that growth on this plane is less kinetically-limited than $\{0001\}$ or $\{10\bar{1}0\}$ [79]. Growth was conducted at 500°C for 3 days.

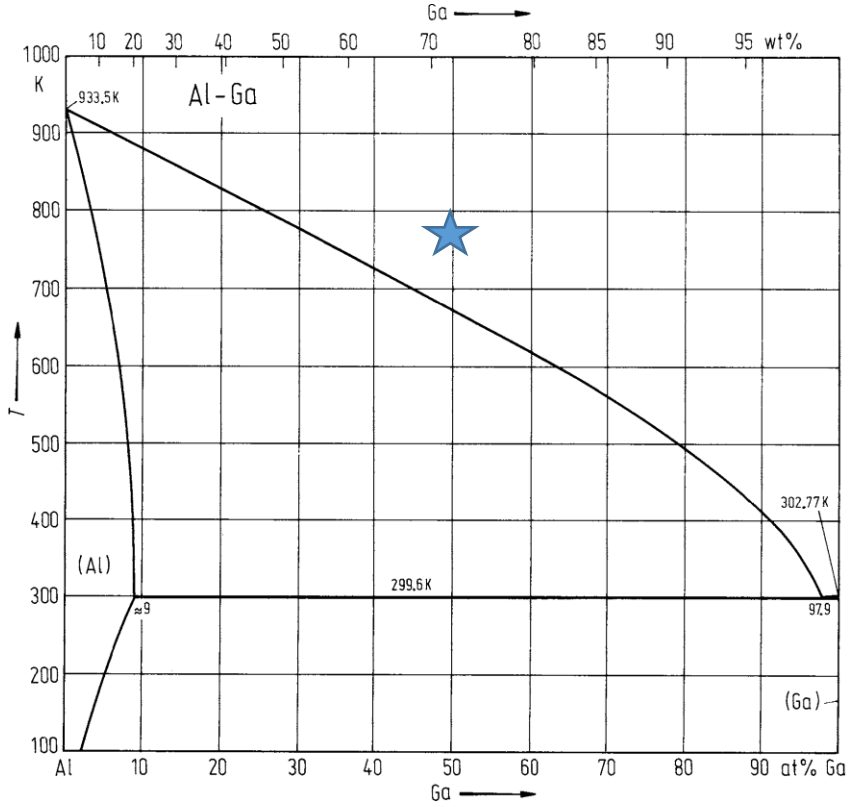

Figure 4-6. Al-Ga binary phase diagram, showing the nominal Group-III initial composition at the growth temperature [122]**.**

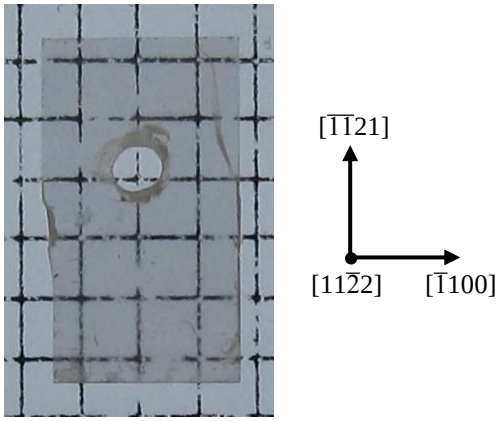

Figure 4-7. {11$\bar{2}$2}-orientation crystal resulting from the Al-Ga-Ag alloy source experiment. The hole present in the crystal was intentionally-drilled to position it above the source material in the autoclave, indicating that the bottom of the crystal, as viewed in the figure, was closest to the source during growth.

As can be seen in Figure 4-7, very little growth occurred on the seed. Similarly to the growth from Ga-Ni and the single phase liquid Ga-Ag solution, polycrystalline deposition was found throughout the autoclave. The bottom edge of the crystal as depicted in Figure 4-7 was

closest to the Al-Ga-Ag source, and as such, that region achieved the largest growth thickness of 16 μm. The center of the crystal grew ~12 μm, while the top of the crystal grew <1 μm. The presence of an axial thickness gradient (with respect to where the source material was in the autoclave) on a less kinetically-limited seed crystal supports the speculation of mass transport limited growth. Figure 4-8 shows a secondary electron micrograph and a panchromatic-CL micrograph of the growth layer at the bottom edge of the crystal. It is apparent that growth did not occur in a uniform layer, but there are regions showing hexagonal symmetry.

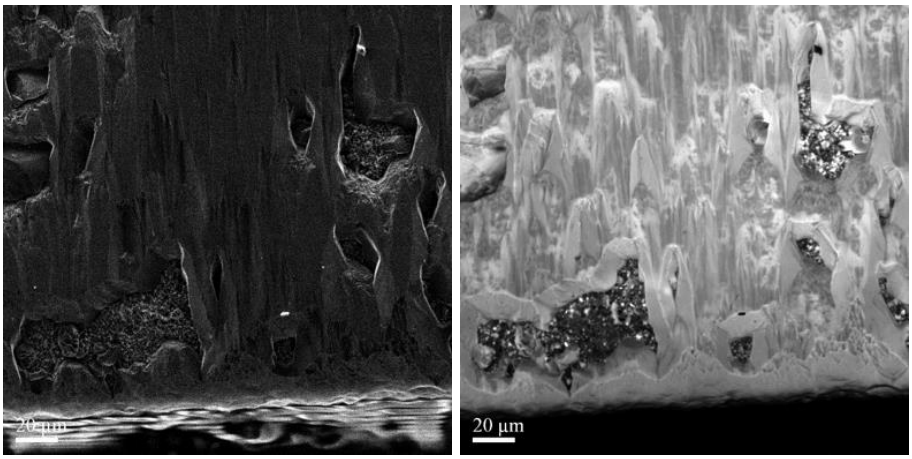

Figure 4-8. Secondary electron micrograph (left) and pan-CL micrograph of the bottom of the {11$\bar{2}$2}-orientation growth layer, with areas of the seed visible beneath.

XRD analysis was used to identify the composition of the grown material. Due to the uneven nature of the growth (which, for example, is depicted in one region of the crystal in Figure 4-8), line focus geometry enabled sampling of both the GaN seed and the growth layer of unknown composition. Thus, a coupled ω-2θ scan was sufficient to identify reflections for both the substrate and the film. The peak positions of the 00ℓ family of asymmetric reflections (where ℓ = 2, 4, and 6) were identified by scanning from ω = 15° - 67°, with the incident beam projected along [1$\bar{1}$00], as shown in Figure 4-9. After accounting for the ω-θ detector offset,

the θ-positions of the substrate peaks (indicated by blue markers in Figure 4-9) and film peaks (indicated by red markers in Figure 4-9) were used to calculate the d-spacing of each family of planes according to Bragg's Law. As shown in Figure 4-10, linear regression was used to match the d-spacings to the inverse-ℓ index according to the Bragg condition for hexagonal 00ℓ planes, as shown in Equation 4-16.

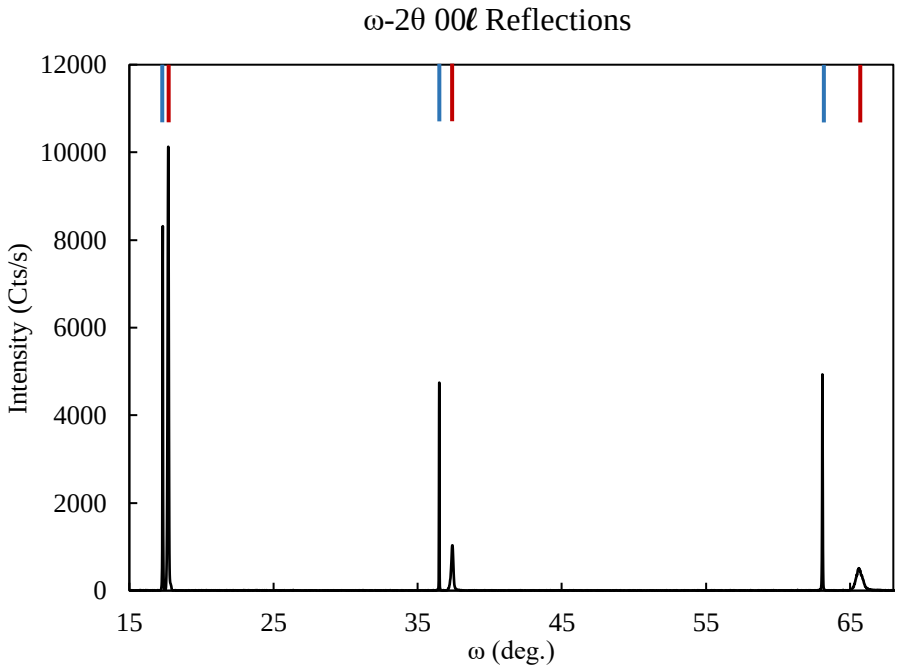

Figure 4-9. Coupled ω-2θ scan showing the 002, 004, and 006 reflections (from lowest to highest angle, respectively) for the GaN substrate (identified by blue lines) and the growth film (indentified by red lines).

Equation 4-16

$$d = \frac{\lambda}{2\sin\theta} = c * \frac{1}{l}$$

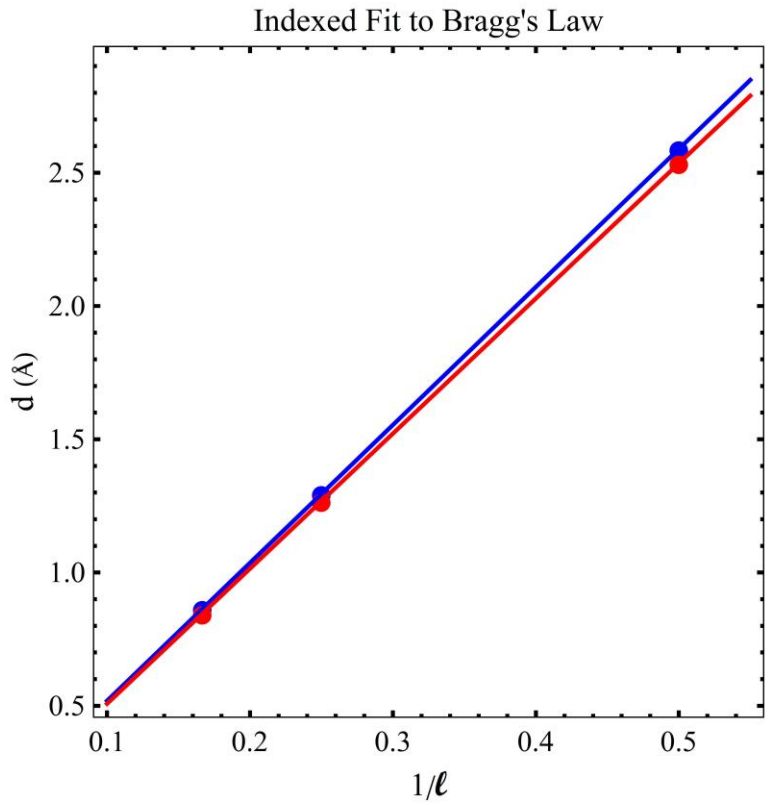

Figure 4-10. d-spacing as a function of inverse-ℓ index (as calculated by Equation 4-16) for the GaN substrate (in blue) and the growth film (in red). Linear regression enables calculation of the c-lattice parameter:5.176 Å for the substrate, and 5.069 Å for the growth film.

This linear regression approach, which resulted in perfect best fit lines, enabled correction of the XRD stage zero-point error to calculate the c-lattice parameter of both the substrate and the film. Using Vegard's Law, with c = 5.185 Å for GaN and c = 4.982 Å for AlN, the composition of the film was determined to be 57 at.% Al on the Group-III site. The composition of the substrate was determined to be 4 at.% Al, which may indicate the order of magnitude of the error for this approach (by not considering the stress state of the substrate or film, etc.). Given the apparent poor quality of the film, as is evident in Figure 4-8, the film was thought to be completely relaxed.

The composition of the film was also inspected using EDX. Quantitatively accurate detection of N is difficult using EDX at high accelerating voltages (~15 kV), which are useful

for the quantifying metallic species, such as Al and Ga. Therefore, EDX was performed on HVPE GaN material and other ammonothermal crystals to determine a baseline for an anticipated N-signal. The N-content of these reference crystals ranged from 36-38 at.%, which matched the two measurements taken from the AlGaN crystal (37 at.% N and 36 at.% N for measurements taken in the middle and bottom of the crystal, respectively). Therefore, it was determined that the Al and Ga signals could yield accurate information regarding the Group-III site occupancy. The resulting Group-III site compositions were determined to be 56 at.% Al and 55 at.% Al for the middle and bottom of the AlGaN crystal, respectively. Clearly, both measurements closely match the composition determined by XRD, and are close to the desired crystal composition of $Al_{0.5}Ga_{0.5}N$. To the best of our knowledge, this is the first demonstration of seeded, bulk ternary Group-III Nitride crystal growth.

4.5.3 Remaining Challenges

In addition to traversing the binary phase space in temperature and composition to change $\Delta\mu$, the effect of total system pressure on growth from Ga-alloy sources must be explored. There may be deviations from the behavior of the relevant binary phase diagrams, which are typically collected at 1 atm, at ammonothermal pressures of interest. Furthermore, it is unclear if appreciable Group-III species are dissolved at low pressure, thereby bottlenecking the growth process at the mass transport stage. Some survey experiments were conducted at less than 100 MPa in this work, which realized etching of the seed crystal, thus supporting this speculation. An additional concern is control over the growth of ternary Group-III Nitrides by employing ternary (or higher order) alloy sources, without established phase diagrams. To completely understand this growth process, or more importantly to pick a

reasonable starting point, the phase behavior of the constituent element solutions must be well-understood. This includes experiments to determine the activity coefficient of the Group-III species in these solutions, which may be a crucial aspect in tuning $\Delta\mu$.

In addition to required knowledge of the aforementioned intensive thermodynamic parameters, there are many engineering challenges which must still be addressed. Perhaps the most obvious challenge with this method is surface area limited alloy source material, and a fixed NH_3 volume to supply the N-species to the crystal. In order to grow large Group-III Nitride boules, continuous feeding of these materials should be explored. Additionally, many of the low melting point excipient alloying elements (Bi, Sn, Pb, etc.) are known to exhibit rapid grain boundary diffusion in structural materials [123]. With little known about the behavior of these elements in Ni-base superalloys, it is important to investigate their compatibility in the temperature, pressure, and chemical regimes of interest. Furthermore, In has been shown to contribute to stress corrosion cracking in Inconel 718 [45], which makes the growth of InGaN in Ni-base autoclaves a technical challenge. Short corrosion studies were conducted with In and Pb contained in TZM crucibles within Inconel 625 autoclaves, with no obvious corrosion products observed. However, an in-depth study on the diffusion length of these materials in coupons of Ni-base superalloys should be conducted for completeness. As previously outlined in this work, the propensity of Ni-components to take-up Ga from supercritical NH_3-Na solutions remains a problem [95], therefore alternative autoclave materials and liner systems should be explored to strictly control Group-III mass transport.

4.6 Summary

A novel supercritical NH_3-Na solution growth method for the production of bulk Group-III Nitride crystals was theorized and demonstrated to address the challenges associated

with ammonothermal growth from source materials produced by competing techniques (e.g. poly GaN produced by HVPE). This method utilizes Group-III alloy source materials under isothermal conditions to establish a chemical potential driving force for crystal growth. Although very few experiments have been performed to date, impurity reduction with respect to traditional ammonothermal growth of GaN from supercritical NH_3-Na solutions has been achieved. Furthermore, seeded growth of bulk AlGaN has been demonstrated, indicating this method may be applicable for the production of bulk ternary Group-III Nitride crystals.

Chapter 5 Conclusions

Confronted with a lack of fundamental crystal growth data/knowledge for the ammonothermal production of bulk GaN, two studies employing in situ fluid temperature analysis were conducted. In the first study, an accurate determination of GaN solubility in supercritical NH_3-Na solutions was reported through the course of 23 gravimetric solubility experiments under ammonothermal conditions (T = 415-650 °C, P ≈ 200 MPa, molar NH_3: Na fill ratio = 20:1). GaN solubility was found to be lower than the previously reported range [85]. Two previously unreported error sources were identified in the explored ammonothermal conditions: Ga-alloying of Ni-containing components (identified using EDX), and Ga dissolution in the Na-rich, second phase (identified using ICP). In general, Ni-containing components depleted Ga from the supercritical NH_3-Na solution at high temperatures (> 475 °C), while the Na-rich phase depleted Ga from the NH_3-Na solution at low temperatures.

The second study focused on identifying bulk GaN crystal growth kinetics, crystal quality, and impurity incorporation as they pertain to supercritical NH_3-Na solution temperatures by extending the in situ fluid temperature measurement capability to both the dissolution and growth zones of ammonothermal autoclaves. These fluid temperature measurements provided direct experimental evidence to confirm the retrograde solubility of GaN in supercritical NH_3-Na solutions in the temperature and pressure regimes of interest (~350 – 600°C and ~180 – 260 MPa, respectively).

Two dominant bulk GaN growth regimes were identified in this system: a mass transport limited regime at low NIST-extrapolated fluid density gradients (<1.2 mol/L), and a surface integration limited regime above this critical fluid density gradient. In surface

integration limited growth, two different Arrhenius processes appear to dominate, one above and one below ~570°C. Knowledge of polar {0001} and nonpolar $\{10\bar{1}0\}$ growth kinetics enabled the assessment of crystal shape evolution with growth zone fluid temperature. It was found that equiaxed crystals (equivalent {0001} and $\{10\bar{1}0\}$ growth rates) are favored at high growth zone temperature, and needle-like crystals (high {0001}:$\{10\bar{1}0\}$ growth rate ratios) are favored at low growth zone temperature. The crystal quality of (0001) orientation ammonothermal material was found to be highly correlated with growth zone fluid temperature, requiring temperatures in excess of ~575°C to match or improve the quality of the HVPE seed crystal. The crystal quality of the $(000\bar{1})$ orientation material, by comparison, was not obviously affected by growth zone fluid temperature. Al, Si, and Mn impurities, identified using SIMS, were found to incorporate in the growing crystals more readily at high dissolution zone fluid temperature, implying they either originate in the poly GaN source material, or become activated from a greater autoclave volume at elevated temperatures. Na, Fe, O, and H impurities were reduced with increasing growth zone fluid temperature, in a consistent fashion with defect-site incorporation

Knowledge of Ga-alloying of Ni-containing components, coupled with impurity incorporation correlated with poly GaN source material, motivated the exploration of Ga-alloy sources for the growth of bulk Group-III Nitride crystals. The chemical potential driving force for this system was derived, and growth was demonstrated. Impurity reduction with respect to traditional ammonothermal growth of GaN (without noble metal liner materials) from supercritical NH_3-Na solutions has been achieved. Furthermore, seeded growth of bulk AlGaN has been demonstrated, indicating this method may be applicable for the production of bulk ternary Group-III Nitride crystals.

References

[1] F. Berna, P. Goldberg, L. K. Horwitz, J. Brink, S. Holt, M. Bamford, and M. Chazan, "PNAS Plus: Microstratigraphic evidence of in situ fire in the Acheulean strata of Wonderwerk Cave, Northern Cape province, South Africa," *Proc. Natl. Acad. Sci.*, vol. 109, no. 20, pp. E1215–E1220, 2012.

[2] Nobel Media, "The 2014 Nobel Prize in Physics - Press Release," 2017.

[3] H. J. Round, "A Note on Carborundum," *Electr. World*, vol. 19, p. 309, 1907.

[4] N. Holonyak Jr. and S. F. Bevacqua, "Coherent (visible) light emission from Ga(As1-xPx) Junctions," *Appl. Phys. Lett.*, vol. 1, no. 4, p. 82, 1962.

[5] T. S. Perry, "M. George Craford [biography]," *IEEE Spectr.*, vol. 32, no. 2, pp. 52–55, 1995.

[6] H. Mimura, T. Matsumoto, and Y. Kanemitsu, "Blue electroluminescence form porous silicon carbide," *Appl. Phys. Lett.*, vol. 65, no. 26, 1994.

[7] K. Ohkawa, T. Karasawa, and T. Mitsuyu, "Characteristics of p-type ZnSe Layers Grown by Molecular Beam Epitaxy with Radical Doping," *Jpn. J. Appl. Phys.*, vol. 30, no. 2A, pp. 152–155, 1991.

[8] H. P. Maruska, W. C. Rhines, and D. A. Stevenson, "Preparation of Mg-doped GaN diodes exhibiting violet electroluminescence," *Mater. Res. Bull.*, vol. 7, no. 8, pp. 777–781, 1972.

[9] H. Amano, N. Sawaki, and I. Akasaki, "Metalorganic vapor-phase epitaxial growth of a high-quality GaN film using an AlN buffer layer," *Appl. Phys. Lett.*, vol. 48, no. 5, pp. 353–355, 1986.

[10] H. Amano, K. Masahiro, H. Kaxumasa, and I. Akasaki, "P-type conduction in Mg-

doped GaN treated with low-energy electron beam irradiation (LEEBI)," *Jpn. J. Appl. Phys.*, vol. 28, no. 12, pp. 2112–2114, 1989.

[11] S. Nakamura, Y. Harada, and M. Seno, "Novel metalorganic chemical vapor deposition system for GaN growth," *Appl. Phys. Lett.*, vol. 58, no. 18, p. 2021, 1991.

[12] S. Nakamura, "GaN Growth Using GaN Buffer Layer," *Jpn. J. Appl. Phys.*, vol. 30, pp. L1705–L1707, 1991.

[13] S. Nakamura, N. Iwasa, and M. Senoh, "Hole compensation mechanism of p-type GaN films," *Jpn. J. Appl. Phys.*, vol. 31, no. 5A, pp. 1258–1266, 1992.

[14] S. Nakamura, T. Mukai, and M. Senoh, "Thermal annealing effects of p-type Mg-doped GaN films," *Japanese J. Appl. Phys. Part 2 - Lett.*, vol. 31, no. 2B, pp. L139–L142, 1992.

[15] H. Kroemer, "A proposed class of hetero-junction injection lasers," *Proc. IEEE*, vol. 51, no. 12, pp. 1782–1783, 1963.

[16] S. Nakamura and T. Mukai, "High-quality InGaN films grown on GaN films," *Jpn. J. Appl. Phys.*, vol. 31, no. 10B, pp. L1457–L1459, 1992.

[17] S. Nakamura, T. Mukai, and M. Senoh, "Candela-class high-brightness InGaN/AlGaN double-heterostructure blue-light-emitting diodes," *Appl. Phys. Lett.*, vol. 64, no. 13, pp. 1687–1689, 1994.

[18] S. Nakamura, N. Senoh, N. Iwasa, and S. Nagahama, "High-brightness InGaN blue, green and yellow light-emitting-diodes with quantum-well structures," *Jpn. J. Appl. Phys.*, vol. 34, no. 2, No. 7A, pp. L797–L799, 1995.

[19] S. Nakamura, S. Masayuki, S. Nagahama, N. Iwasa, T. Yamada, T. Matsushita, H. Kiyoku, and Y. Sugimoto, "InGaN-based multi-quantum-well structure laser diodes,"

Jpn. J. Appl. Phys., vol. 35, no. 2, 1B, pp. L74–L76, 1996.

[20] S. Nakamura, M. Senoh, S. Nagahama, N. Iwasa, T. Yamada, T. Matsushita, Y. Sugimoto, and H. Kiyoku, "Room-temperature continuous-wave operation of InGaN multi-quantum-well structure laser diodes," *Appl. Phys. Lett.*, vol. 69, no. 26, pp. 4056–4058, 1996.

[21] C. Weisbuch, M. Piccardo, L. Martinelli, J. Iveland, J. Peretti, and J. S. Speck, "The efficiency challenge of nitride light-emitting diodes for lighting," *Phys. Status Solidi*, vol. 212, no. 5, pp. 899–913, 2015.

[22] "DOE SSL Program, R&D Plan," 2015.

[23] C.-C. Pan, S. Tanaka, F. Wu, Y. Zhao, J. S. Speck, S. Nakamura, S. P. DenBaars, and D. Feezell, "High-Power, Low-Efficiency-Droop Semipolar ($20\bar{2}1$) Single-Quantum-Well Blue Light-Emitting Diodes," *Appl. Phys. Express*, vol. 5, no. 6, p. 062103, 2012.

[24] J. S. Speck, S. F. Chichibu, and G. Editors, "Nonpolar and Semipolar Group III Materials," vol. 34, no. May, 2009.

[25] A. Inoue, R. Kato, A. Yamada, and T. Yokogawa, "Extremely high current density over 1000 A / cm 2 operation in m-plane GaN small size LEDs with low efficiency droop and method for controlling radiation pattern and polarization," *2012 Int. Electron Devices Conf.*, pp. 621–624, 2012.

[26] J. S. Speck and S. J. Rosner, "The role of threading dislocations in the physical properties of GaN and its alloys," *Phys. B Condens. Matter*, vol. 273–274, pp. 24–32, Dec. 1999.

[27] K. Motoki, "Development of Gallium Nitride Substrates," *SEI Tech. Rev.*, no. 70, pp.

28–35, 2010.

[28] I. Kizilyalli, A. Edwards, O. Aktas, T. Prunty, and D. Bour, “Vertical Power p-n Diodes Based on Bulk GaN,” *IEEE Trans. Electron Devices*, vol. 62, no. 2, pp. 414–422, 2015.

[29] W. Utsumi, H. Saitoh, H. Kaneko, T. Watanuki, K. Aoki, and O. Shimomura, “Congruent melting of gallium nitride at 6 GPa and its application to single-crystal growth.,” *Nat. Mater.*, vol. 2, no. 11, pp. 735–8, Nov. 2003.

[30] K. Fujito, S. Kubo, H. Nagaoka, T. Mochizuki, H. Namita, and S. Nagao, “Bulk GaN crystals grown by HVPE,” *J. Cryst. Growth*, vol. 311, no. 10, pp. 3011–3014, May 2009.

[31] R. Madar, G. Jacob, J. Hallais, and R. Fruchart, “High-pressure solution growth of GaN,” *J. Cryst. Growth*, vol. 31, pp. 197–203, 1975.

[32] T. Yoshida, M. Imanishi, T. Kitamura, K. Otaka, M. Imade, M. Shibata, and Y. Mori, “Development of GaN substrate with a large diameter and small orientation deviation,” *Phys. Status Solidi*, vol. 1600671, pp. 1–4, 2017.

[33] P. Von Dollen, S. Pimputkar, M. A. Alreesh, S. Nakamura, and J. S. Speck, “A new system for sodium flux growth of bulk GaN. Part II: In situ investigation of growth processes,” *J. Cryst. Growth*, vol. 456, pp. 67–72, 2016.

[34] G. Dhanaraj, K. Byrappa, V. Prasad, and M. Dudley, *Springer Handbook of Crystal Growth*, vol. 39, no. 5. 2010.

[35] K. F. Schafthaul, *Gelehrt. Anz. Bayer. Akad.*, vol. 20, p. 557, 1845.

[36] H. E. Saint-Claire Deville, *Ann. Chim. Phys.*, vol. 61, pp. 309–314, 1857.

[37] K. Byrappa and Y. Masahiro, *Handbook of Hydrothermal Technology*. 2001.

[38] D. McWhan, *Sand and Silicon: Science That Changed the World*. 2012.

[39] R. Juza and H. Jacobs, *Angew. Chem. Int. Ed. Engl.*, vol. 5, p. 247, 1966.

[40] R. Dwilinski, A. Wysmolesk, M. Baranowski, M. Kaminska, R. Doradzinski, J. Garczynski, L. Sierzputowski, and H. Jacobs, "GaN Synthesis by Ammonothermal Method," *Acta Phys. Pol. A*, vol. 88, p. 833, 1995.

[41] R. A. Laudise, *Prog. Inorg. Chem.*, vol. 3, no. 1, 1962.

[42] H. Jacobs and D. Schmidt, "High-pressure ammonolysis in solid-state chemistry," in *Current Topics in Materials Science, Volume 8*, 1982, pp. 381 – 428.

[43] B. Wang and M. J. Callahan, "Ammonothermal Synthesis of III-Nitride Crystals," *Cryst. Growth Des.*, vol. 6, no. 6, pp. 1227–1246, Jun. 2006.

[44] B. Hertweck, T. Steigerwald, N. Alt, and E. Schluecker, "Corrosive degeneration of autoclaves for the ammonothermal synthesis: experimental approach and first results," *Chem. Eng. Technol.*, vol. 37, pp. 1903–1906, 2014.

[45] B. Hertweck, T. G. Steigerwald, N. S. A. Alt, and E. Schluecker, "Different corrosion behaviour of autoclaves made of nickel base alloy 718 in ammonobasic and ammonoacidic environments," *J. Supercrit. Fluids*, vol. 95, pp. 158–166, 2014.

[46] B. Hertweck, S. Schimmel, T. Steigerwald, N. Alt, P. Wellmann, and E. Schluecker, "Ceramic liner technology for ammonoacidic synthesis," *J. Supercrit. Fluids*, vol. 99, pp. 76–87, 2015.

[47] S. Pimputkar, T. F. Malkowski, S. Griffiths, A. Espenlaub, S. Suihkonen, J. S. Speck, and S. Nakamura, "Stability of Materials in Supercritical Ammonia Solutions," *J. Supercrit. Fluids*, vol. 110, pp. 193–229, 2015.

[48] R. Dwilinski, J. Baranowski, M. Kaminska, R. Doradzinski, J. Garczynski, and L.

Sierzputowski, “On GaN crystallization by ammonothermal method,” *Acta Phys. Pol. A*, vol. 90, no. 4, pp. 763–766, 1996.

[49] R. Dwiliski, R. Doradziski, J. Garczyski, L. Sierzputowski, J. Baranowski, and M. Kamiska, “Exciton photo-luminescence of GaN bulk crystals grown by the AMMONO method,” *Mater. Sci. Eng. B*, vol. 50, no. 1–3, pp. 46–49, 1997.

[50] M. Zając, R. Doradziński, J. Gosk, J. Szczytko, M. Lefeld-Sosnowska, M. Kamińska, A. Twardowski, M. Palczewska, E. Grzanka, and W. Gębicki, “Magnetic and optical properties of GaMnN magnetic semiconductor,” *Appl. Phys. Lett.*, vol. 78, no. 9, p. 1276, 2001.

[51] R. Dwilinski and Y. Doradzinski, R.M., Garczynski, J.S., Sierzputowski, L.P., Kanbara, “United State Patent No. US 6,656,615 B2,” 2003.

[52] I. Application, P. Under, T. H. E. Patent, and C. Treaty, *No Title*, no. 12. 2004.

[53] R. Dwilinski, R. Doradzinski, J. Garczynski, L. Sierzputowski, A. Puchalski, Y. Kanbara, K. Yagi, H. Minakuchi, and H. Hayashi, “Excellent crystallinity of truly bulk ammonothermal GaN,” *J. Cryst. Growth*, vol. 310, no. 17, pp. 3911–3916, Aug. 2008.

[54] R. Dwilinski, “Growth of GaN crystals by the ammonothermal method,” in *The International Workshop on Nitride Semiconductors (Switzerland)*, 2008.

[55] R. Kucharski, M. Rudziński, M. Zając, R. Doradziński, J. Garczyński, L. Sierzputowski, R. Kudrawiec, J. Serafińczuk, W. Strupiński, and R. Dwiliński, “Nonpolar GaN substrates grown by ammonothermal method,” *Appl. Phys. Lett.*, vol. 95, no. 13, p. 131119, 2009.

[56] R. Kudrawiec, R. Kucharski, M. Rudziński, M. Zając, J. Misiewicz, W. Strupiński, R. Doradziński, and R. Dwiliński, “Application of contactless electroreflectance to study

the epi readiness of m-plane GaN substrates obtained by ammonothermal method," *J. Vac. Sci. Technol. A Vacuum, Surfaces, Film.*, vol. 28, no. 6, p. L18, 2010.

[57] T. Hashimoto, K. Fujito, F. Wu, B. A. Haskell, P. T. Fini, and J. S. Speck, "Mater. Res. Soc. Symp. Proc. Vol. 831 © 2005 Materials Research Society E2.8.1," vol. 831, pp. 1–6, 2005.

[58] T. Hashimoto, K. Fujito, M. Saito, J. S. Speck, and S. Nakamura, "Ammonothermal Growth of GaN on an over-1-inch Seed Crystal," *Jpn. J. Appl. Phys.*, vol. 44, no. No. 52, pp. L1570–L1572, Dec. 2005.

[59] T. Hashimoto, K. Fujito, R. Sharma, E. R. Letts, P. T. Fini, J. S. Speck, and S. Nakamura, "Phase selection of microcrystalline GaN synthesized in supercritical ammonia," *J. Cryst. Growth*, vol. 291, no. 1, pp. 100–106, May 2006.

[60] T. Hashimoto, F. Wu, J. S. Speck, and S. Nakamura, "Ammonothermal growth of bulk GaN," *J. Cryst. Growth*, vol. 310, no. 17, pp. 3907–3910, Aug. 2008.

[61] M. Saito, D. S. Kamber, T. J. Baker, K. Fujito, S. P. DenBaars, J. S. Speck, and S. Nakamura, "Plane Dependent Growth of GaN in Supercritical Basic Ammonia," *Appl. Phys. Express*, vol. 1, no. 12, p. 121103, Dec. 2008.

[62] M. Saito, H. Yamada, K. Iso, H. Sato, H. Hirasawa, D. S. Kamber, T. Hashimoto, S. P. DenBaars, J. S. Speck, and S. Nakamura, "Evaluation of GaN substrates grown in supercritical basic ammonia," *Appl. Phys. Lett.*, vol. 94, no. 5, p. 052109, 2009.

[63] S. Pimputkar, S. Kawabata, J. S. Speck, and S. Nakamura, "Surface morphology study of basic ammonothermal GaN grown on non-polar GaN seed crystals of varying surface orientations from m-plane to a-plane," *J. Cryst. Growth*, vol. 368, pp. 67–71, Apr. 2013.

[64] D. R. Ketchum, G. L. Schimek, W. T. Pennington, and J. W. Kolis, “Synthesis of new Group III fluoride – ammonia adducts in supercritical ammonia : structures of AlF 3 (NH 3) 2 and,” vol. 294, pp. 200–206, 1999.

[65] D. R. Ketchum and J. W. Kolis, “Crystal growth of gallium nitride in supercritical ammonia,” *J. Cryst. Growth*, vol. 222, no. 3, pp. 431–434, May 2001.

[66] M. J. Callahan, B. Wang, L. O. Bouthillette, S. Wang, J. W. Kolis, and D. F. Bliss, “Growth of GaN crystals under ammonothermal conditions,” vol. 798, pp. 1–6, 2004.

[67] J. Bai, M. Dudley, B. Raghothamachar, P. Gouma, B. J. Skromme, L. Chen, P. J. Hartlieb, E. Michaels, and J. W. Kolis, “Correlated structural and optical characterization of ammonothermally grown bulk GaN,” *Appl. Phys. Lett.*, vol. 84, no. 17, p. 3289, 2004.

[68] B. Wang, M. J. Callahan, K. D. Rakes, L. O. Bouthillette, S.-Q. Wang, D. F. Bliss, and J. W. Kolis, “Ammonothermal growth of GaN crystals in alkaline solutions,” *J. Cryst. Growth*, vol. 287, no. 2, pp. 376–380, Jan. 2006.

[69] S. Zhang, N. S. a. Alt, E. Schlücker, and R. Niewa, “Novel alkali metal amidogallates as intermediates in ammonothermal GaN crystal growth,” *J. Cryst. Growth*, vol. 403, pp. 22–28, Oct. 2014.

[70] M. Callahan, B. G. Wang, K. Rakes, D. Bliss, L. Bouthillette, M. Suscavage, and S. Q. Wang, “GaN single crystals grown on HVPE seeds in alkaline supercritical ammonia,” *J. Mater. Sci.*, vol. 41, no. 5, pp. 1399–1407, Mar. 2006.

[71] B. T. Adekore, M. J. Callahan, L. Bouthillette, R. Dalmau, and Z. Sitar, “Synthesis of erbium-doped gallium nitride crystals by the ammonothermal route,” *J. Cryst. Growth*, vol. 308, no. 1, pp. 71–79, Oct. 2007.

[72] D. Bliss, B. Wang, M. Suscavage, R. Lancto, S. Swider, W. Eikenberry, and C. Lynch, "Ammonothermal GaN: Morphology and properties," *J. Cryst. Growth*, vol. 312, no. 8, pp. 1069–1073, Apr. 2010.

[73] T. Hashimoto, F. Wu, J. S. Speck, and S. Nakamura, "A GaN bulk crystal with improved structural quality grown by the ammonothermal method.," *Nat. Mater.*, vol. 6, no. 8, pp. 568–571, Aug. 2007.

[74] Y. Mikawa, T. Ishinabe, S. Kawabata, and T. Mochizuki, "Ammonothermal Growth of Polar and Non-polar Bulk GaN Crystal," vol. 9363, pp. 1–6, 2015.

[75] D. Ehrentraut, R. T. Pakalapati, D. S. Kamber, W. Jiang, D. W. Pocius, B. C. Downey, M. Mclaurin, and M. P. D'Evelyn, "High Quality , Low Cost Ammonothermal Bulk GaN Substrates," vol. 52, pp. 1–4, 2013.

[76] Q. Bao, M. Saito, K. Hazu, Y. Kagamitani, K. Kurimoto, D. Tomida, K. Qiao, T. Ishiguro, C. Yokoyama, and S. F. Chichibu, "Ammonothermal growth of GaN on a self-nucleated GaN seed crystal," *J. Cryst. Growth*, vol. 404, pp. 168–171, Oct. 2014.

[77] Y. Kagamitani, D. Ehrentraut, A. Yoshikawa, N. Hoshino, T. Fukuda, S. Kawabata, and K. Inaba, "Ammonothermal Epitaxy of Thick GaN Film Using NH 4 Cl Mineralizer," *Jpn. J. Appl. Phys.*, vol. 45, no. 5A, pp. 4018–4020, May 2006.

[78] K. Yoshida, K. Aoki, and T. Fukuda, "High-temperature acidic ammonothermal method for GaN crystal growth," *J. Cryst. Growth*, vol. 393, pp. 93–97, May 2014.

[79] S. Pimputkar, S. Kawabata, J. S. Speck, and S. Nakamura, "Improved growth rates and purity of basic ammonothermal GaN," *J. Cryst. Growth*, vol. 403, pp. 7–17, Oct. 2014.

[80] K. Fujito, S. Kubo, and I. Fujimura, "Development of Bulk GaN Crystals and Nonpolar/Semipolar Substrates by HVPE," *MRS Bull.*, vol. 34, pp. 313–317, 2009.

[81] S. Schimmel, M. Lindner, T. G. Steigerwald, B. Hertweck, T. M. M. Richter, U. Künecke, N. S. Alt, R. Niewa, E. Schlücker, and P. J. Wellmann, "Determination of GaN solubility in supercritical ammonia with NH4F and NH4Cl mineralizer by in situ x-ray imaging of crystal dissolution," *J. Cryst. Growth*, vol. 418, pp. 64–69, May 2015.

[82] D. Ehrentraut, Y. Kagamitani, C. Yokoyama, and T. Fukuda, "Physico-chemical features of the acid ammonothermal growth of GaN," *J. Cryst. Growth*, vol. 310, no. 5, pp. 891–895, Mar. 2008.

[83] D. Tomida, K. Kuroda, N. Hoshino, K. Suzuki, Y. Kagamitani, T. Ishiguro, T. Fukuda, and C. Yokoyama, "Solubility of GaN in supercritical ammonia with ammonium chloride as a mineralizer," *J. Cryst. Growth*, vol. 312, no. 21, pp. 3161–3164, Oct. 2010.

[84] D. Tomida, T. Kuribayashi, K. Suzuki, Y. Kagamitani, T. Ishiguro, T. Fukuda, and C. Yokoyama, "Effect of halogen species of acidic mineralizer on solubility of GaN in supercritical ammonia," *J. Cryst. Growth*, vol. 325, no. 1, pp. 52–54, Jun. 2011.

[85] T. Hashimoto, M. Saito, K. Fujito, F. Wu, J. S. Speck, and S. Nakamura, "Seeded growth of GaN by the basic ammonothermal method," *J. Cryst. Growth*, vol. 305, no. 2, pp. 311–316, Jul. 2007.

[86] Q. Bao, M. Saito, K. Hazu, K. Furusawa, Y. Kagamitani, R. Kayano, D. Tomida, K. Qiao, T. Ishiguro, C. Yokoyama, and S. F. Chichibu, "Ammonothermal Crystal Growth of GaN Using an NH 4 F Mineralizer," *Crys Grow Des*, vol. 13, p. 4158, 2013.

[87] R. Juza, H. H. Weber, and K. Opp, "Kristallstruktur des Natriumamids," *Zeitschrift für*

Anorg. und Allg. Chemie, vol. 284, no. 1, pp. 73–82, 1956.

[88] M. Nagib, H. Kistrup, and H. Jacobs, "Neutron-diffraction by sodium-deuteroamide, NaND2," *Atomkernenergie*, vol. 26, no. 2, pp. 87–90, 1975.

[89] S. Pimputkar and S. Nakamura, "Decomposition of supercritical ammonia and modeling of supercritical ammonia-nitrogen-hydrogen solutions with applicability toward ammonothermal conditions," *J. Supercrit. Fluids*, vol. 107, pp. 17–30, 2016.

[90] S. Fernandez-Garrido, G. Koblmuller, E. Calleja, and J. S. Speck, "In situ GaN decomposition analysis by quadrupole mass spectrometry and reflection high-energy electron diffraction," *J. Appl. Phys.*, vol. 104, no. 3, pp. 1–6, 2008.

[91] Predel B., "Ga-Ni (Gallium-Nickel) Phase diagram," *Landolt-Bornstein*, vol. IV, no. 5, 1991.

[92] O. Ruff and J. Zedner, *Ber.*, vol. 41, p. 1948, 1908.

[93] O. Ruff and E. Geisel, *Ber.*, vol. 39, p. 838, 1906.

[94] T. Steigerwald, N. Alt, B. Hertweck, and E. Schluecker, "Feasibility of density and viscosity measurements under ammonothermal conditions," *J. Cryst. Growth*, vol. 403, pp. 59–65, 2014.

[95] S. Griffiths, S. Pimputkar, J. S. Speck, and S. Nakamura, "On the solubility of gallium nitride in supercritical ammonia-sodium solutions," *J. Cryst. Growth*, vol. 456, pp. 5–14, 2016.

[96] M.A. Lovette, A. R. Browning, D. W. Griffin, J. P. Sizemore, R. C. Snyder, and M. F. Doherty, "Crystal Shape Engineering," *Ind. Eng. Chem. Res.*, vol. 47, no. 24, pp. 9812–9833, Dec. 2008.

[97] R. Laudise, *The Growth of Single Crystals*. Prentice-Hall, 1970.

[98] R. Laudise, *Hydrothermal crystal growth - some recent results*, Advanced C. Prentice-Hall, 1987.

[99] R. Laudise and R. Sullivan, *Chem. Eng. Prog.*, vol. 55, pp. 55–59, 1959.

[100] L. Leal, *Advaned Transport Phenomena*. Cambridge Univ Press, 2007.

[101] Q. S. Chen, S. Pendurti, and V. Prasad, "Effects of baffle design on fluid flow and heat transfer in ammonothermal growth of nitrides," *J. Cryst. Growth*, vol. 266, no. 1–3, pp. 271–277, May 2004.

[102] Q.-S. Chen, S. Pendurti, and V. Prasad, "Modeling of ammonothermal growth of gallium nitride single crystals," *J. Mater. Sci.*, vol. 41, no. 5, pp. 1409–1414, Mar. 2006.

[103] Y.-N. Jiang, Q.-S. Chen, and V. Prasad, "Numerical simulation of ammonothermal growth processes of GaN crystals," *J. Cryst. Growth*, vol. 318, no. 1, pp. 411–414, Mar. 2011.

[104] A. Chernov, *Modern Crystallography III: Crystal Growth*. Springer, 1984.

[105] L. Mu, H. He, and C. Feng, "Lattice energy estimation for complex inorganic ionic crystal," *Chinese J. Chem.*, vol. 24, no. 7, pp. 855–861, 2006.

[106] M. R. Louthan and R. G. Derrick, "Permeability of nickel to high pressure hydrogen isotopes," *Scr. Metall.*, vol. 10, no. 1, pp. 53–55, 1976.

[107] E. H. Van Deventer and V. A. Maroni, "Hyrdogen permeation characteristics of some austenitic and nickel-base alloys," *J. Nucl. Mater.*, vol. 92, pp. 103–111, 1980.

[108] I. Chou, "Permeability of precious metals to hydrogen at 2kb total pressure and elevated temperatures," *Am. J. Sci.*, vol. 286, pp. 638–658, 1986.

[109] K. T. Jacob and G. Rajitha, "Discussion of enthalpy, entropy and free energy of

formation of GaN," *J. Cryst. Growth*, vol. 311, no. 14, pp. 3806–3810, Jul. 2009.

[110] B. Predel, "Bi-Ga (Bismuth-Gallium) Phase diagram," *Landolt-Bornstein*, vol. IV, no. 5, 1991.

[111] B. Predel, "Ga-Pb (Gallium-Lead) Phase diagram," *Landolt-Bornstein*, vol. IV, no. 5, 1991.

[112] B. Predel, "Ga-Sn (Gallium-Tin) Phase diagram," *Landolt-Bornstein*, vol. IV, no. 5, 1991.

[113] B. Predel, "Ga-Tl (Gallium-Thallium) Phase diagram," *1Landolt-Bornstein*, vol. IV, no. 5, 1991.

[114] B. Predel, "Ag-Ga (Silver-Gallium) Phase diagram Crystal structure," *Landolt-Bornstein*, vol. IV, no. 5, 1991.

[115] B. Predel, "Co-Ga (Cobalt-Gallium) Phase diagram," *Landolt-Bornstein*, vol. IV, no. 5, 1991.

[116] B. Predel, "Ga-Gd (Gallium-Gadolinium) Phase diagram," *Landolt-Bornstein*, vol. IV, no. 5, 1991.

[117] B. Predel, "Ga-Hf (Gallium-Hafnium) Phase diagram," *Landolt-Bornstein*, vol. IV, no. 5, 1991.

[118] B. Predel, "Ga-Sb (Gallium-Antimony) Phase diagram," *Landolt-Bornstein*, vol. IV, no. 5, 1991.

[119] B. Predel, "Ga-Sc (Gallium-Scandium) Phase diagram," *Landolt-Bornstein*, vol. IV, no. 5, 1991.

[120] L. Graph, "Ga-Te (Gallium-Tellurium) Phase diagram," *Landolt-Bornstein*, vol. IV, no. 5, 1991.

[121] B. Predel, “Ga-Yb (Gallium-Ytterbium) Phase diagram,” *Landolt-Bornstein*, vol. IV, no. 5, 1991.

[122] B. Predel, “Al-Ga (Aluminum-Gallium) Phase diagram,” *Landolt-Bornstein*, vol. IV, no. 5, 1991.

[123] M. R. Chellali, L. Zheng, R. Schlesiger, B. Bakhti, A. Hamou, J. Janovec, and G. Schmitz, “Grain boundary segregation in binary nickel-bismuth alloy,” *Acta Mater.*, vol. 103, pp. 754–760, 2016.

Appendix A Stability of Materials in Supercritical Ammonia Solutions

A detailed review of the stability of materials in supercritical-NH_3 solutions (NH_3-Na, pure NH_3, and NH_3-Cl) was conducted in Ref. [47]. The analysis was based on the chemical and mechanical stability of the materials in each of the three solutions, and a summary of notable observations specific to each material was reported. The chemical stability of materials was determined by their relative mass change, thickness change (when accurately obtained with sufficiently small experimental error), and color change. In some cases, EDX was also used to determine chemical stability. Chemical stability is defined here as the absence of any measurable chemical changes that compromised the integrity of the sample. For example, a sample can change color and lose a small amount of mass but still be considered chemically stable if the changes are such that the expected lifetime of the sample would be long compared to the length of a typical ammonothermal run. The mechanical stability of materials was determined by observable changes in mechanical properties (such as embrittlement) and macroscopic defects (such as crack formation, spalling, etc.).

A general "recommendation" was made for each material in each solution based on the aggregate knowledge collected for the material and is presented using a checkmark (✓), a circle (○), or a cross (×) in the following tables. A checkmark indicates that the material has good to excellent chemical and mechanical stability in the indicated supercritical NH_3-solution and should be considered for future in-depth studies for chemically inert components (for example, internal components, liners, etc.). A circle indicates that the material could potentially be used under certain circumstances, though it should not necessarily be considered simultaneously

chemically and mechanically stable. A cross suggests the material is not stable for the given environment as it severely degraded, though it may be suitable as a solute.

A.1 Ceramics

A.1.1 Oxides

Name	Recommendation			Weight Change (%)		
	NH_3-Na	NH_3	NH_3-Cl	NH_3-Na	NH_3	NH_3-Cl
Aluminum Silicate $Al_{13.1}Si_{21.0}Fe_{0.8}K_{0.6}Ti_{0.4}O_{64.1}$	×	○	✓	-1.62	-0.49	+0.11
Fused Silica SiO_2	×	✓	✓	-100.00	-0.02	-0.90
Glass Ceramic $Si_{20.7}Al_{7.9}Li_{3.2}Mg_{1.9}Ca_{1.4}Na_{0.6}$ $Ti_{0.6}Zn_{0.6}Ba_{0.5}K_{0.4}Zr_{0.4}O_{61.8}$	×	✓	○	-21.58	+0.02	-0.07
Glass Mica $Si_{15.4}Mg_{8.5}F_{4.2}Al_{3.2}K_{2.1}B_{2.0}O_{64.5}$	×	○	○	-4.61	+0.05	-0.44
Machinable Alumina Ceramic Al_2O_3	×	✓	○	-92.53	-0.89	+4.60
Magnesium Oxide MgO	×	✓	×	-4.05	N/A	-100.00
Quartz SiO_2	×	✓	✓	-100.00	-0.13	0.00
Sapphire Al_2O_3	×	✓	✓	-51.82 -47.14	0.00 -0.03	-0.01 0.00
Sintered Alumina Al_2O_3	×	✓	✓	-4.07	-0.05	-0.04
Soda lime $Si_{24.4}Al_{0.5}K_{0.6}Mg_{2.3}Na_{10.0}Ca_{2.5}O_{59.7}$	×	○	○	-100.00	N/A	-1.43
Yttria-stabilized Zirconia $Zr_{29}Y_5O_{66}$	○	✓	✓	-0.05	-0.04	-0.30
Zirconia ZrO_2	✓	✓	○	-0.01	0.00	-0.10

A.1.2 Nitrides

Name	Recommendation			Weight Change (%)		
	NH_3-Na	NH_3	NH_3-Cl	NH_3-Na	NH_3	NH_3-Cl
Hot-Pressed Boron Nitride BN	×	○	○	-5.51	-0.54	-0.20
Pyrolytic Boron Nitride BN	×	○	○	-19.77	-1.55	+0.84
Silicon Nitride Si_3N_4	×	✓	✓	-1.56	-0.02	-0.02

A.1.3 Carbides

Name	Recommendation			Weight Change (%)		
	NH_3-Na	NH_3	NH_3-Cl	NH_3-Na	NH_3	NH_3-Cl
Silicon Carbide SiC	○	✓	✓	-0.97	-0.05	0.00
Tungsten Carbide $(WC)_{90\text{-}94}Co_{6\text{-}10}Fe_{0\text{-}4}$	✓	✓	✓	0.00	0.00	-0.16

A.2 Metals

A.2.1 Pure

Name	Recommendation			Weight Change (%)		
	NH_3-Na	NH_3	NH_3-Cl	NH_3-Na	NH_3	NH_3-Cl
Aluminum Al	×		×	-100.00		-100.00
Gold Au	×	✓	✓	-8.76	+0.13	+0.09
Iridium Ir	×			-27.55		
Lanthanum La		×			+77.00	

Magnesium Mg	×		×	-27.28		-100.00
Niobium Nb	○	○	○	+0.88	+0.71 -0.44	+0.89
Palladium Pd	×	✓	✓	-55.17	+0.21	+0.97
Scandium Sc		✓			+3.18	
Silver Ag	✓	✓	×	-0.04	0.00	-5.49
Tantalum Ta	○	○	×	+0.32	-5.40	+1.17
Titanium Ti	×	✓	○	+3.29 N/A	+0.20	+0.50
Vanadium V	○	○	✓	+1.45	+1.29	-0.42
Yttrium Y	×	×	×	-100.00	N/A	-100.00 -100.00
Zirconium Zr	×	✓	×	-0.28	+0.31	N/A

A.2.2 Cobalt and Cobalt Alloys

Name	Recommendation			Weight Change (%)		
	NH_3-Na	NH_3	NH_3-Cl	NH_3-Na	NH_3	NH_3-Cl
Cobalt Co	✓	✓	×	+0.04	-0.01	-40.98 -41.54
Co-W-Al Alloy $Co_{80}W_{10.6}Al_{9.4}$	✓	✓	✓	-0.02	+0.07	-0.05

A.2.3 Copper and Copper Alloys

Name	Recommendation			Weight Change (%)		
	NH_3-Na	NH_3	NH_3-Cl	NH_3-Na	NH_3	NH_3-Cl
Brass 260 $Cu_{71}Zn_{29}$	×	○	×	-53.64	-9.29	-100.00
Constantan (TC J-, TC E-) $Cu_{53}Ni_{47}$	○	✓	×	+2.00	-0.09	-100.00
Copper Cu	×	○	×	-100.00	-6.36	-100.00

A.2.4 Iron and Iron Alloys

Name	Recommendation			Weight Change (%)		
	NH_3-Na	NH_3	NH_3-Cl	NH_3-Na	NH_3	NH_3-Cl
1018 Steel $Fe_{98.3}Mn_{0.8}C_{0.9}$	○	○	×	+2.58	+0.86	-66.95
15-5 PH $Fe_{75.9}Cr_{16.1}Ni_{4.5}Si_{2.0}Mn_{1.0}C_{0.3}Nb_{0.2}P_{0.1}S_{0.1}$	○	○	×	+0.27	+0.88	-1.22
17-4 PH $Fe_{75.6}Cr_{17.1}Ni_{3.7}Si_{1.9}Mn_{1.0}C_{0.3}Nb_{0.2}P_{0.1}S_{0.1}$	○	○	×	+0.25	+0.86	-1.96
316L Stainless Steel $Fe_{64.7}Cr_{18.1}Ni_{11.3}Mn_{2.0}Si_{2.0}Mo_{1.4}C_{0.4}P_{0.1}S_{0.1}$	○	○	×	+0.81 +0.24 +0.27	+0.81 +2.46	-0.08 +0.80

A.2.5 Molybdenum and Molybdenum Alloys

Name	Recommendation			Weight Change (%)		
	NH_3-Na	NH_3	NH_3-Cl	NH_3-Na	NH_3	NH_3-Cl
Molybdenum Mo	✓	✓	✓	+0.01	+0.03	0.00
TZM $Mo_{99.6}Ti_{0.3}Zr_{0.1}$	✓	✓	✓	0.00	0.00	0.00

A.2.6 Nickel and Nickel Alloys

Name	Recommendation			Weight Change (%)		
	NH_3-Na	NH_3	NH_3-Cl	NH_3-Na	NH_3	NH_3-Cl
Chromel C (TC K+) / Alumel (TC K-) Junction $Ni_{89}Cr_{11}$ / $Ni_{92}Mn_2Al_4Si_2$	○	○	×	+0.02	+0.36	-63.62
Hastelloy C-276 $Ni_{58.9}Cr_{18.7}Mo_{10.4}Fe_{6.2}Co_{2.7}W_{1.3}$ $Mn_{1.1}V_{0.4}Si_{0.2}P_{0.1}S_{0.1}C_{0.1}$	✓	✓	○	+0.02	+0.05	-0.01
Nickel Ni	✓	✓	×	+0.01	+0.05	-52.22
Nicrosil (TC N+) / Nisil (TC N-) Junction $Ni_{81.2}Cr_{15.7}Si_{2.8}Mg_{0.2}$ / $Ni_{91.2}Si_{8.8}$	○	○	×	+0.03	+0.28	-59.18

A.2.7 Platinum and Platinum Alloys

Name	Recommendation			Weight Change (%)		
	NH_3-Na	NH_3	NH_3-Cl	NH_3-Na	NH_3	NH_3-Cl
Platinum (TC R-) Pt	×	✓	✓	-100.00	+1.83	+1.63
Platinum-Rhodium (TC R+) $Pt_{78}Rh_{22}$	×	✓	✓	-86.38	+1.70	+1.26
Platinum-Ruthenium $Pt_{91}Ru_9$	✓	✓	✓	+2.27	+2.50	+5.06

A.2.8 Tungsten and Tungsten Alloys

Name	Recommendation			Weight Change (%)		
	NH_3-Na	NH_3	NH_3-Cl	NH_3-Na	NH_3	NH_3-Cl
High-Strength Durable Tungsten $W_{74.7}Ni_{15.6}Cu_{9.6}$	✓	✓	○	-0.10	-0.01	-0.32
Tungsten W	✓	✓	○	-0.94	0.00	0.00 +0.05
Tungsten-Rhenium (TC C-) $W_{74}Re_{26}$	✓	✓	✓	-0.02	-0.04	+0.10
Tungsten-Rhenium (TC C+) $W_{95}Re_5$	✓	✓	✓	-1.29	-0.04	+0.07

A.3 Metalloids

Name	Recommendation			Weight Change (%)		
	NH_3-Na	NH_3	NH_3-Cl	NH_3-Na	NH_3	NH_3-Cl
Germanium Ge	×	○	×	N/A	-6.92	+42.33
Silicon Si	×	✓	×	N/A	-0.07	+1.53